Università degli Studi di Padova

Dipartimento di Fisica e Astronomia

SCUOLA DI DOTTORATO DI RICERCA IN FISICA

CICLO XXV°

The lifetime of the 6.79 MeV state in ^{15}O as a challenge for nuclear astrophysics and γ-ray spectroscopy: a new DSAM measurement with the AGATA Demonstrator array

Direttore della Scuola : Ch.mo Prof. Andrea Vitturi

Supervisori : Ch.mo Prof. Santo Lunardi,

Dott. Calin Alexandru Ur

Dottoranda : Caterina Michelagnoli

Abstract

The determination of the *thermonuclear reaction rates* is a challenging task of nuclear astrophysics. In order to investigate this and other nuclear processes in the stellar medium, new techniques and new advanced setups for nuclear physics experiments are of vital importance.

In this Thesis an advanced γ–ray spectroscopy system has been used in an experiment of astrophysical interest, that is a new Doppler shift attenuation measurement of the lifetime of the 6.79 MeV state in ^{15}O. An accurate measurement of this quantity is of paramount importance in the determination of the astrophysical S–factor and the derived cross section for the ^{14}N(p,γ)^{15}O reaction, the slowest one in the CNO cycle. The results of a new direct measurement of this nuclear level lifetime are discussed. The first excited states in ^{15}O (and ^{15}N) were populated via fusion–evaporation and nucleon–transfer reactions of ^{14}N on ^{2}H (implanted at the surface of a $\approx$4 mg/cm^2 Au layer) at 32 MeV beam energy, provided by the XTU Tandem at the Legnaro National Laboratories. Gamma rays were detected with 4 triple clusters of the AGATA Demonstrator array, placed at backward angles, allowing to measure the angular distribution of the emitted gamma rays in a continuous way. The energy resolution and position sensitivity of this state–of–the–art gamma spectrometer have been exploited to investigate lifetimes of nuclear levels in the $\approx$fs range via the Doppler Shift Attenuation Method. The deconvolution of the lifetime effects on the line–shapes of the gamma–peaks from the ones due to the kinematics of the emitting nuclei has been performed by means of detailed Monte Carlo simulations of the gamma emission and detection. Coupled–channel calculations for the nucleon transfer process have been used for this purpose.

Being one of the first experiments using this state–of–the art γ–ray spectroscopy tool, particular emphasis will be put in the description of the not trivial data replay

and analysis, as well as the development of an *ad hoc* simulation tool.

The comparison of experimental and simulated spectra of high–energy gamma–rays, de–exciting levels with lifetimes in the few fs range, will be shown for the 6.79 MeV transition in ^{15}O and for known cases in ^{15}N, together with details of the chi–square analysis. Lifetime estimates for excited levels in ^{15}N will be given and compared with previous results. The data analysis allows to give a new limit to the lifetime of the 6.79 MeV state in ^{15}O.

Riassunto

La determinazione della sezione d'urto delle reazioni termonucleari nelle stelle è una delle sfide più impegnative per l'astrofisica nucleare. Per comprendere questo ed altri processi nucleari che avvengono nel mezzo stellare sono fondamentali gli esperimenti di fisica nucleare con tecniche e strumentazioni sempre più avanzate. In questo lavoro di tesi, è stato utilizzato per la prima volta un apparato d'avanguardia per la spettroscopia gamma per un esperimento di interesse astrofisico e, cioè, una nuova misura della vita media dello stato a 6.79 MeV nel nucleo ^{15}O, utilizzando il metodo del Doppler shift attenuato. Una determinazione accurata di questa quantità è, infatti, di estrema importanza per ricavare il fattore astrofisico S e la corrispondente sezione d'urto della rezione ^{14}N(p,γ)^{15}O, la più lenta del ciclo CNO. Verranno quindi presentati e discussi i risultati di una nuova misura diretta della vita media dello stato in questione. I primi stati eccitati del nucleo ^{15}O (e ^{15}N) sono stati popolati attraverso i meccanismi di fusione-evaporazione e di trasferimento di nucleoni nella reazione ^{14}N + ^{2}H (impiantato sulla superficie di 4mg/cm^2 di uno strato di oro) ad una energia di 32 MeV, con il fascio di ^{14}N accelerato dal Tandem XTU dei Laboratori Nazionali di Legnaro. I raggi gamma prodotti nella reazione sono stati rivelati mediante quattro rivelatori compositi (clusters tripli) del dimostratore di AGATA, posti all'indietro rispetto alla linea di fascio, consentendo una misura, in modo continuo, della distribuzione angolare dei raggi gamma. La risoluzione in energia e la sensibilità alla posizione di interazione di questo modernissimo spettrometro gamma sono stati utilizzati per misurare vite medie nel range dei fs mediante il"Doppler Shift Attenuation Method". Il contributo degli effetti dovuti alla vita media sulle forme di riga dei picchi gamma, rispetto a quelli legati alla cinematica dei nuclei emessi è stato estratto mediante dettagliate simulazioni Monte Carlo della emissione e rivelazione della radiazione gamma. A questo scopo sono stati effettuati calcoli in canali accoppiati del processo di trasferimento di nucleoni.

Trattandosi di uno dei primi esperimenti in cui tale spettrometro d'avanguardia è coinvolto, verranno discussi in dettaglio i vari passaggi dell'analisi dei dati e dello sviluppo di una parte di codice Monte Carlo.

Il confronto tra gli spettri sperimentali e simulati per raggi gamma di energia molto alta, che diseccitano stati nucleari di pochi fs, verrà mostrato per la transizione di 6.79 MeV nel nucleo ^{15}O e per alcuni livelli del nucleo ^{15}N. Vengono presentati anche i dettagli dell'analisi del chi-quadro, essenziale per ottenere i risultati. I valori di vita media ottenuti per gli stati eccitati del nucleo ^{15}N vengono confrontati con i risultati noti in letteratura. L'analisi dei dati conclusiva ha permesso di dare un nuovo limite alla vita media del livello a 6.79 MeV del nucleo ^{15}O.

Contents

List of Figures **iii**

List of Tables **vii**

1 Introduction **1**

1.1 Stellar burning rates 1

1.2 The Carbon–Nitrogen–Oxygen (CNO) cycle and the ^{14}N(p,γ)^{15}O reaction 6

1.3 ^{14}N(p,γ)^{15}O reaction cross–section measurements 9

1.3.1 The width of the sub–threshold resonance at -506 keV, i.e. the lifetime of the 6.79 MeV state in ^{15}O 11

1.4 Existing literature for the lifetime of the 6.79 MeV state in ^{15}O : why is a new evaluation needed 12

1.5 Thesis outline 15

2 Experimental method and setup **17**

2.1 The Doppler Shift Attenuation method for the measurement of nuclear level lifetimes 17

2.1.1 Doppler Shift techniques 19

2.1.1.1 Doppler Shift Attenuation (DSA) method: lineshape analysis 22

2.1.1.2 Pushing the DSA technique to the *femtosecond* limit . . 28

2.2 Gamma–ray spectroscopy with segmented HPGe detectors: modern gamma–ray tracking arrays 30

2.2.1 Principles of gamma–ray tracking 34

2.2.2 Pulse shape analysis 40

2.2.2.1 Radiation damage from fast neutrons 44

2.2.3 The AGATA project 45
2.2.3.1 The AGATA Demonstrator at the Legnaro National Laboratories 52
2.3 The experiment for the measurement of the lifetime of the 6.79 MeV state in ^{15}O 55
2.3.1 The deuterium target 58

3 Replay of the data from the AGATA Demonstrator array 61
3.1 Data replay (processing) 61
3.1.1 Local Level Processing (LLP) 63
3.1.2 Global Level Processing (GLP) 79
3.2 Data sorting 84

4 Monte Carlo simulations for lifetime measurements with Doppler shift techniques 89
4.1 Simulations with the `Geant4` package 90
4.2 The AGATA simulation code 91
4.3 Extension of the code to include complex level scheme and nuclear level lifetimes 92
4.3.1 Preliminary test of the code with some experimental data 94

5 The lifetime of the 6.79 MeV state in ^{15}O 99
5.1 Data analysis 99
5.1.1 The simulated spectra 103
5.1.1.1 Calculations of the kinematics for the ^{14}N(d,n) and ^{14}N(d,p) reactions 106
5.2 Lineshape analysis 111
5.2.1 The lifetime of the 8.31 MeV state in ^{15}N 111
5.2.2 The lifetime of the 10.06 MeV state in ^{15}N 116
5.2.3 The lifetime of the 6.79 MeV state in ^{15}O 119

6 Conclusions 125

Bibliography 127

List of Figures

1.1 Example of Hertzsprung–Russell diagram 2
1.2 Hydrogen burning 3
1.3 The Gamow peak 4
1.4 Data extrapolation to the Gamow energies in the presence of a sub–threshold resonance 5
1.5 Predicted solar neutrinos fluxes 7
1.6 The structure of the Sun 8
1.7 Level structure of ^{15}O 9
1.8 S–factor vs Energy for the ^{14}N(p,γ)^{15}O reaction 10
1.9 Extrapolation of the ^{14}N(p,γ)^{15}O reaction cross–section to Gamow energies 11

2.1 Main lifetime measurement techniques 18
2.2 Effect of different recoil velocities on the observed γ peak 20
2.3 Recoil distance method (plunger) 21
2.4 Examples of slowing–down times 22
2.5 Doppler Shift Attenuation Method 23
2.6 Stopping matrix and lineshape analysis 25
2.7 Intrinsic and measured lineshape 26
2.8 Sensitivity to fs lifetimes 29
2.9 Spectroscopic history of the ^{156}Dy nucleus 30
2.10 Sensitivity of γ arrays across the years 32
2.11 Cross sections for gamma interaction in germanium 35
2.12 Compton scattering 36
2.13 Clustering techniques 37

2.14 Peak efficiency versus position resolution 38
2.15 The gamma–ray tracking concept 39
2.16 Radial dependence of the shape of the signal in a coaxial germanium detector 40
2.17 Net charge and transient signals 41
2.18 n–damage effects in a HPGe operated in position sensitive mode 45
2.19 AGATA 4π configuration 46
2.20 Geometry of one AGATA detector 47
2.21 GTS tree 48
2.22 AGATA front–end electronics and read–out system 49
2.23 The AGATA Demonstrator array at the LNL 53
2.24 AGATA Demonstrator campaign at the LNL 54
2.25 Experimental setup 55
2.26 Level schemes of ^{15}O and ^{15}N 56
2.27 AGATA setup for the experiment 57
2.28 Deuterium target implantation profile 59

3.1 Comparison of γ spectra before and after the offline data replay 62
3.2 Detector numbering 64
3.3 Local Level Processing 65
3.4 Raw waveforms 66
3.5 Producer amplitudes 67
3.6 Timestamp differences 68
3.7 AmBe(Ni) gamma source spectrum 71
3.8 Central contact spectrum vs sum of segment energies 72
3.9 Segments cross–talk correction 72
3.10 Alignment of the time of the waveforms 73
3.11 Correction for a broken segment 74
3.12 PSA traces 75
3.13 Interaction point distributions 76
3.14 AmBe(Fe) source spectrum 77
3.15 Scaling factors for the central–contacts 78
3.16 Correction for n–damage 78

3.17 Global Level Processing . . . 79
3.18 Timestamp differences . . . 80
3.19 Comparison between tracked and sum–event spectra . . . 81
3.20 Number of detected γ rays per tracked event . . . 82
3.21 Angle of the first interaction point . . . 83
3.22 Spectra reconstructed as Compton and pair–production . . . 83
3.23 Coincidences with a composite gamma line . . . 84
3.24 γ–ray energy vs θ of the first interaction point . . . 86
3.25 Energy spectrum for different "angle θ" slices . . . 87
3.26 Lineshape of the 8.31 MeV line in ^{15}N observed at different angles . . . 87

4.1 `Geant4` philosophy . . . 90
4.2 Conceptual organization in classes of the simulation code . . . 93
4.3 Simulation macro file . . . 95
4.4 Simulated spectra of complex level schemes following fusion–evaporation reactions . . . 96
4.5 Simulated lineshapes of gamma peaks produced in fusion–evaporation reactions . . . 97
4.6 Simulated spectra for a differential plunger measurement . . . 97

5.1 Source subtracted spectra . . . 101
5.2 Normalization coefficients used for the source subtraction . . . 102
5.3 Background subtraction . . . 103
5.4 Escape subtraction . . . 104
5.5 Normalization for the subtraction of the escape peaks . . . 104
5.6 Evolution of the lineshape with increasing complexity of the kinematics 106
5.7 χ^2 on stooped lines . . . 107
5.8 Nucleon–transfer and fusion–evaporation components in the γ lineshape 107
5.9 Test of the CDCC-CRC calculations . . . 109
5.10 CDCC-CRC calculations for the nucleon–transfer process . . . 110
5.11 Reduced χ^2 vs τ for the 8.31 MeV level in ^{15}N . . . 112
5.12 Reduced χ^2 vs p_{fe} for the 8.31 MeV level in ^{15}N . . . 113
5.13 Lineshape of the 8312 keV level in ^{15}N for different p_{fe} . . . 113
5.14 Lineshape of the 8312 keV level in ^{15}N for different τ . . . 114

5.15 Reduced χ^2 vs τ for different θ angles 115
5.16 Lifetime of the 8.3 MeV level in ^{15}N 116
5.17 Reduced χ^2 vs τ for the 10.06 MeV level in ^{15}N 117
5.18 Lineshape analysis for the 10.06 MeV level in ^{15}N 117
5.19 Reduced χ^2 vs τ for the 6792 keV state in ^{15}O 118
5.20 Reduced χ^2 vs p_{fe} for the 6792 keV state in ^{15}O 118
5.21 Sensitivity of the simulated lineshapes to chnges of the lifetime in the fs region 120
5.22 The lifetime of the 6.79 MeV state in ^{15}O 121
5.23 6.79 MeV in ^{15}O lineshapes. 122

List of Tables

1.1 Summary of the results on the lifetime of the 6.79 MeV state in ^{15}O present in the literature 12

2.1 Examples of lifetime measurements in ^{15}O and ^{15}N 19

3.1 Polar and azimuthal angles of the R,G and B detectors 64

3.2 Tracked vs sum–energy spectrum for the 7.63 and 7.64 MeV lines 81

LIST OF TABLES

1

Introduction

Theoretical predictions and experimental results on Nuclear Physics observables are fundamental pieces of the puzzle constituted by many astrophysical problems. The Nuclear Physics information needed in the context of Astrophysics is often quite demanding, due to the extreme conditions characterizing the stellar plasma. The branch of Nuclear Astrophysics of interest in the contest of this Thesis deals with the determination of *thermonuclear reaction rates*, i.e. the interaction probabilities and rates of energy production in stars and stellar explosions, responsible for the ongoing synthesis of the elements (1).

In the following sections, the tools for the study of stellar burning rates will be briefly described and the relevant aspects that make fundamental a new estimation of the lifetime of the 6.79 MeV level in ^{15}O will be outlined. The content of this Thesis will be, then, summarized.

1.1 Stellar burning rates

Observation of stars reveals a variety of stellar conditions, that can be classified using the *luminosity* vs *surface temperature* (or *magnitude* vs *color*) correlation, namely the so–called *Hertzsprung–Russel* diagram (1, 2). An example of such a diagram for stars belonging to a globular cluster is reported in Fig. 1.1. Almost 80% of the stars reside in the *main sequence*, diagonal of this correlation. These stars support themselves via *hydrogen–burning*, through the *pp chain* and the *CNO bi–cycle*, outlined in Fig. 1.2. The reaction cross–sections involved in these processes are fundamental ingredients

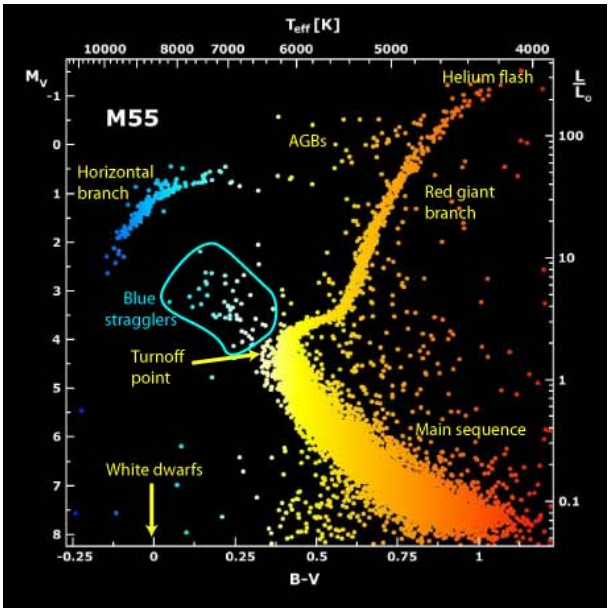

Figure 1.1: Example of Hertzsprung–Russell diagram - Hertzsprung–Russell diagram for the M55 globular cluster (3). The turn–off point –where the stars deviate from the main sequence (see text)– is indicated.

in the understanding of stellar evolution and nucleosynthesis (1). The average energy available for the reaction is the one of the thermal motion in the stellar plasma, kT, with T temperature of the stellar interior. For a hydrogen–burning core, T $\approx$8–55$\times10^6$K, for our Sun T$\approx$ 15.5×10^6 K. This energy is usually not sufficient to overcome the Coulomb barrier. For instance, the Coulomb barrier for the lightest possible binary reaction, namely p+p (or H+H), is $\approx$400 keV, while, for instance, $kT_{Sun} \approx 1$ keV. The reaction proceeds through quantum mechanical tunneling of such barrier. The probability for this effect decreases exponentially with the decreasing interaction energy (in the center of mass of the binary system). On the other side, the particles inside the stellar plasma are distributed according to the Maxwell–Boltzmann distribution. The interplay of these two trends is reported in Fig. 1.3, and defines a maximum in the interaction probability at the *Gamow peak*. The reaction cross–sections in the Gamow energy range are of the order of femtobarn–picobarn, as the longevity of the stars suggests. The actual reproduction of these reactions in the laboratory is affected by signal–to–noise ratio and signal to environmental background ratio far smaller than one. Big steps in the direction of the direct measurement of thermonuclear reaction rates have been

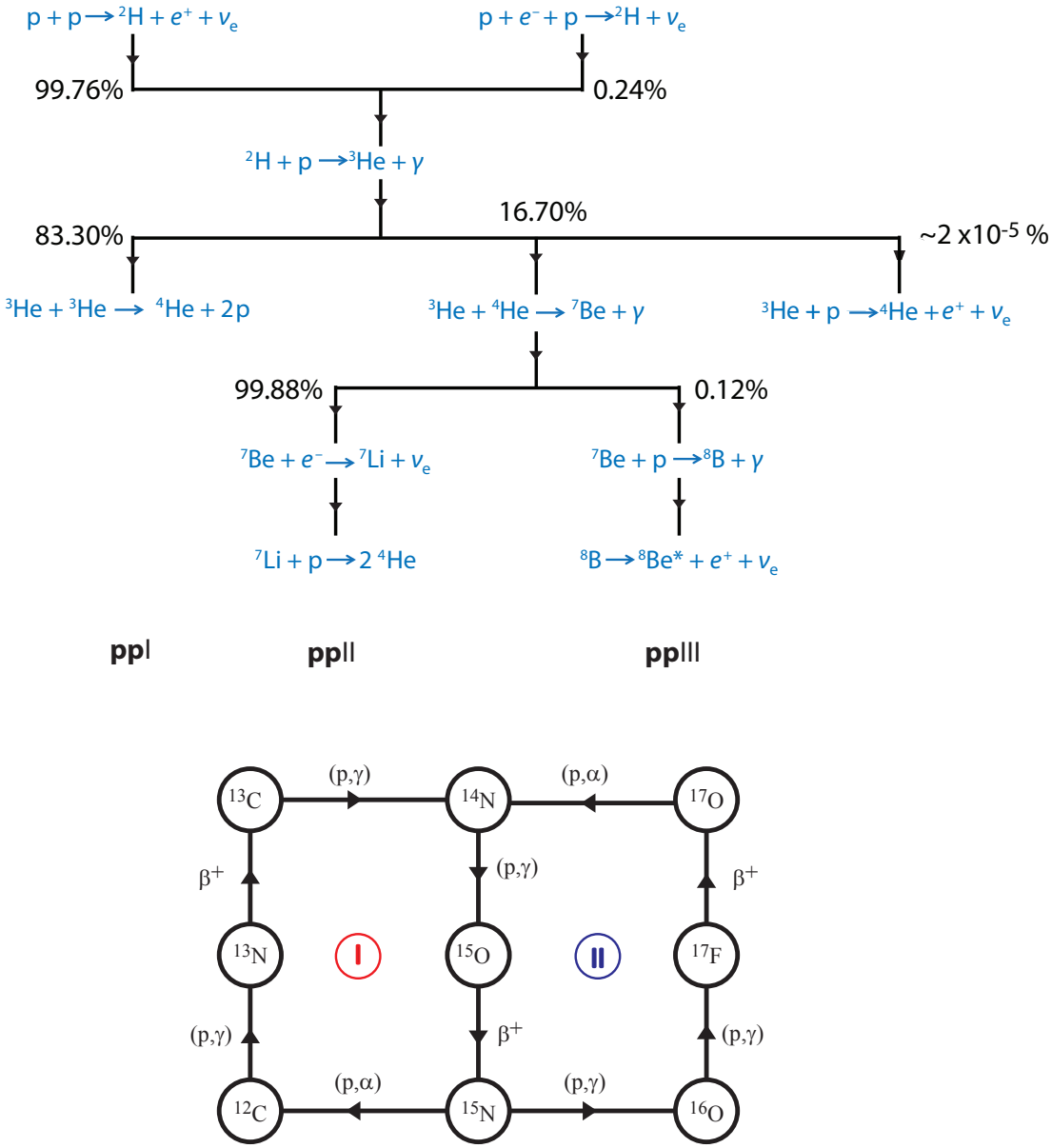

Figure 1.2: Hydrogen burning - The *pp chain* (up) and the CNO bi–cycle (down) for the hydrogen burning in the main sequence stars (4). The initial and final states are $4\,\mathrm{p} \rightarrow {}^4\mathrm{He} + 2\,e^+ + 2\,\nu_e$.

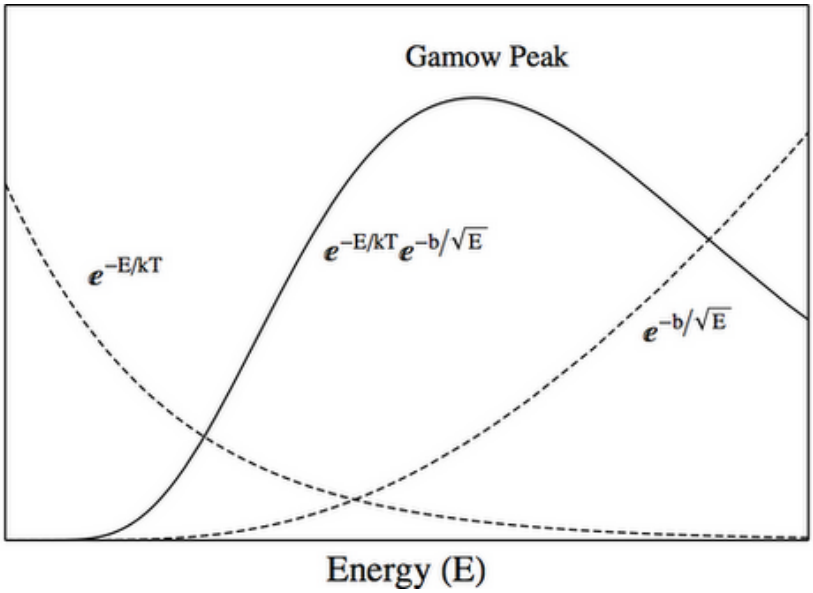

Figure 1.3: The Gamow peak - The product of the Maxwell–Boltzmann probability distribution –$\propto e^{-kT}$– and the tunneling probability of the Coulomb barrier –$\propto e^{-b/\sqrt{E}}$ entails a maximum, corresponding to the *Gamow peak*.

done using underground facilities, as, for instance, the experimental campaign carried–out by the LUNA (Laboratory for Underground Nuclear Astrophysics) collaboration (5). Although the development of the experimental setups and analysis techniques has allowed for the extension of the excitation functions down to center–of–mass energies of the order of several keV, the Gamow energies interval is not reached in most cases and an extrapolation is needed to obtain the reaction cross–section (S–factor) at stellar energies, as it is for instance the case of the ^{14}N(p,γ)^{15}O reaction, that will be discussed later in Sec. 1.2. In order to isolate the strong energy dependence due to Coulomb effects in the reaction cross–section $\sigma(E)$, the nuclear part is summarized in the *astrophysical S–factor* $S(E)$ (2):

$$\sigma(E) = \frac{S(E)}{E} \exp[-2\pi\eta(E)] \tag{1.1}$$

where η is the Sommerfeld parameter, $2\pi\eta$ =31.29Z1 Z_1 Z_2 $(\mu/\mathrm{E})^{1/2}$, with Z_1 and Z_2 electric charges of the two nuclei, μ the reduced mass expressed in mass units and E the energy in the center of mass system (keV). Because the S–factor is slowly varying, one can extrapolate $S(E)$ more reliably than the corresponding $\sigma(E)$, from the range of energies where experimental data are available to the lower energies characterizing

the Gamow peak. When considering relation 1.1 in the expression of the interaction probability, an effective S–factor can be factorized from the Taylor expansion of the exponential functions involved (Eqn. 6 in (4) and formulation from (6)):

$$S_{eff} = S(0)(1 + \frac{5kT}{36E_0}) + S^{'}(0)E_0(1 + \frac{35kT}{36E_0}) + \frac{1}{2}S^{''}(0)E_0^2(1 + \frac{89kT}{36E_0}) \qquad (1.2)$$

where E_0 is the Gamow peak energy, corresponding to the maximum interaction probability, and kT is the available energy due to thermal motion. Rates in an astrophysical plasma can be calculated given S(E), slowly varying as a function of the energy. In the case of non-resonant reactions, it can be approximated by its zero-energy value S(0) and possible corrections determined by its first and second derivatives, $S^{'}(0)$ and $S^{''}(0)$ (Eqn. 1.2).

For most of the reactions contributing to the pp chain and CNO bi–cycle, data have been obtained only for energies in regions above the Gamow peak, e.g., typically $E \gtrsim 70$ keV, so that extrapolations to lower energies depend on the quality of the fit to higher energy data. Attention should be payed, anyway, to the possible occurrence of resonances, in particular sub–threshold ones, as schematically reported in Fig. 1.4. As one can see from this text–book picture, such a phenomenon may compromise

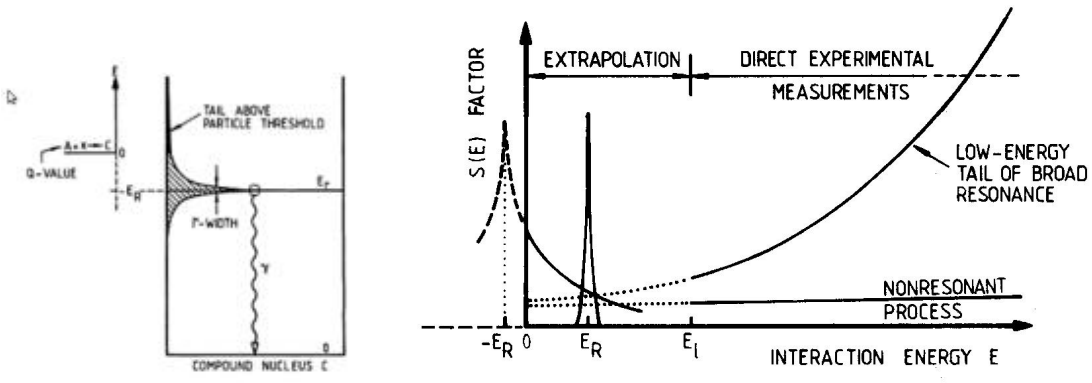

Figure 1.4: Data extrapolation to the Gamow energies in the presence of a sub–threshold resonance - Example of excitation function in terms of S–factor (right) (7). Three types of possible resonances that can occur in case of a charge–particle induced reaction are schematically represented. The reaction cross–section at low energies can be dominated by a resonance just slightly above the threshold or by the tail of a sub–threshold resonance, schematically represented in the level scheme on the left (7).

the extrapolation of the reaction cross–section at stellar energies in case of a wrong parametrization.

An overview of such extrapolation techniques is reported in (4) (and references therein). A widely adopted fitting procedure is the one based on the R–matrix theory (8), in the parametrization developed by (9). In this way, known nuclear properties can be included in the fitting procedure and experimental resonance properties can be used in order to decrease the number of free parameters in the fitting procedure.

A prime example of the influence of an accurate determination of the resonance parameters in the determination of the S–factor at stellar energies is given by the ^{14}N(p,γ)^{15}O reaction in the CN cycle.

1.2 The Carbon–Nitrogen–Oxygen (CNO) cycle and the ^{14}N(p,γ)^{15}O reaction

The CNO cycle was proposed by Bethe and von Weizsäcker to account for the evolutionary path of massive stars. The CNO bi–cycle (Fig. 1.2), differently from the pp–chain, requires pre–existing metals[1] to process H into ^{4}He. This cycle is the most efficient energy source in massive stars. The knowledge of the overall rate of this cycle is thus important for the study of their evolution. In particular, this cycle rules the energy production of stars at the *turn–off* of the main sequence –Fig. 1.1: when the hydrogen fuel in a star's core runs out, the shrinking due to gravity takes place and the hydrogen starts burning in shell at higher temperature through the CNO cycle. In this way, the star "moves away" from the main sequence, towards the red giant branch (1). The rate of the cycle influences the luminosity at the main–sequence turn–off, thus affecting the determination of the age of globular clusters ((10) and references therein).

In our Sun, the CNO cycle accounts for only less than 1% of the energy production. The knowledge of the rate of the cycle can anyway shed light on some fundamental astrophysical questions. The CN–cycle, denoted by I in Fig. 1.2, is indeed a neutrino source, that can be used to test some assumptions of the *Solar Standard Model* (SSM). The ^{13}N and ^{15}O neutrinos have an energy spectrum –reported in red in Fig. 1.5– with end–point energies of 1.2 and 1.7 MeV, respectively. While the *solar neutrino problem* has been successfully solved (6, 12), the *solar composition problem* is nowadays one of

[1] With "metal" we refer to elements heavier than H and ^{4}He.

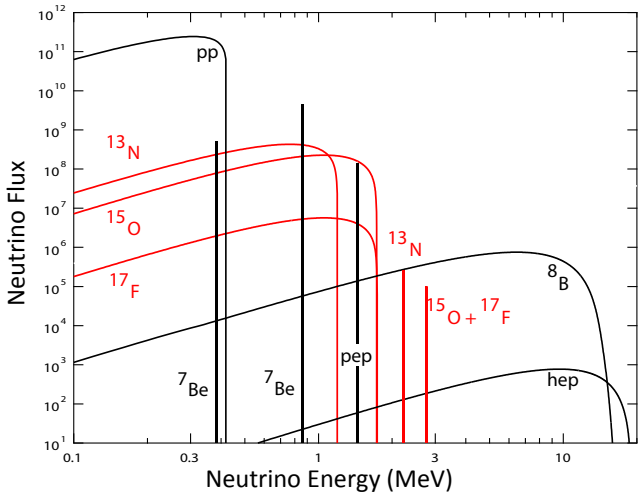

Figure 1.5: Predicted solar neutrinos fluxes - Solar neutrino fluxes calculated in (11) (figure taken from (4)). Line fluxes are in $cm^{-2}\,s^{-1}$ and spectral fluxes are in $cm^{-2}\,s^{-1}\,MeV^{-1}$. The ^{13}N and ^{15}O neutrino fluxes depend almost linearly from the cross–section of the ^{14}N(p,γ)^{15}O reaction, "bottle–neck" of the CNO cycle. The CNO neutrino flux is $\approx$1/10 of the ^{7}Be one.

the headlines concerning the pertinence of the SSM in the description of the structure and evolution of our Sun (4, 13, 14), optimal testing ground for the main sequence stellar evolution. It addresses the homogeneity of the metal content across the solar volume. Assuming the Sun *metallicity* $Z = [metal]/[H]$ (ratio between the metal and hydrogen concentrations) as constant over the solar bulk, the interior metal abundances, one of the inputs for the SSM, can be equated to the convective zone abundances –Fig. 1.6– experimentally deduced from the analysis of the photospheric absorption lines.

A quantity that can be predicted by the SSM and depends on the Sun's metal content is the *sound speed profile*. Being a function of the Sun's interior pressure and density profiles, it reflects the thermal transport properties, that depend on the Sun's metal content, through the *opacity* (1, 4). Such an output from the SSM can be verified with the experimental results from helioseismology (15). A recent and more accurate analysis of the photospheric absorption lines leads to reduced metallicity estimates from Z$\approx$0.0169 to 0.0122 (16), destroying the once excellent agreement between helioseismology and the SSM. It has been suggested that this difficulty may reflect, contrary to the SSM assumption, differences in solar core and convective-zone metallicity that could have arisen from the late-stage evolution of the solar disk (17).

It has been suggested (17) to use the neutrino fluxes from the β^+ decay of ^{13}N and ^{15}O in the CNO cycle of hydrogen burning (Fig. 1.2) to address this problem. These quantities depend linearly on the solar core metallicity, in particular the C and N abundances. New–generation neutrino experiments (such as Borexino (18) and SNO+ (19)) are indeed expected to be sensitive to these neutrino fluxes, Fig. 1.5. The accurate measurement of these quantities can be used to determine the C and N content of the solar core, provided the nuclear cross sections of the key–processes involved in the cycle are accurately known.

The ^{14}N(p,γ)^{15}O reaction is the slowest reaction in the CN cycle at low temperatures and thus the rate–controlling step, that rules the energy production rate of the cycle. In particular, it is the key reaction to determine the ^{13}N and ^{15}O solar neutrino flux, which depends almost linearly on its cross section. By using CNO neutrinos as a probe

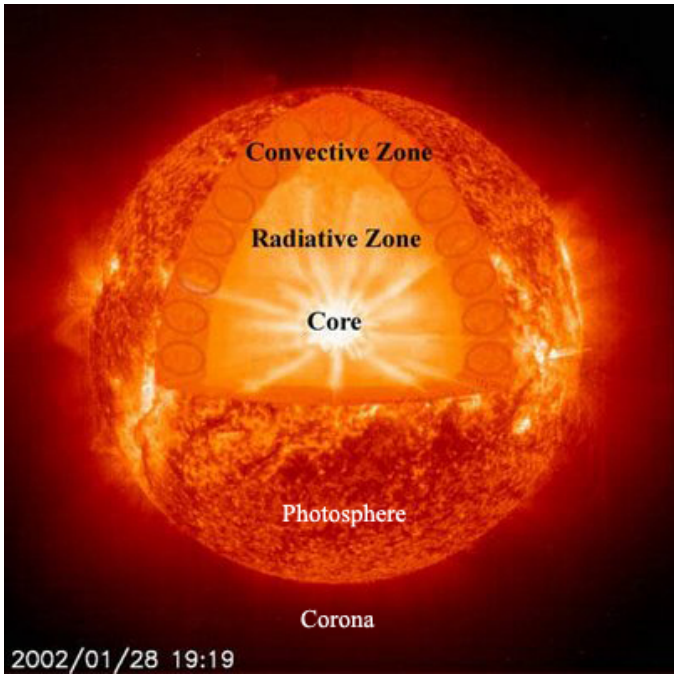

Figure 1.6: The structure of the Sun - The different "layers" along the Sun's volume are labelled in the figure taken from (20). The *core* (20–25% of the radius) is the center of the thermonuclear fusion reactions (T$\approx 15\times10^6$K, $\rho \approx 150\,$g/cm^3). Such energy is first radiated and then carried toward the surface by heat convection currents. The Sun's energy escapes from a $\approx 200\,$km thick region, the *photosphere*, as visible light. The metallicity at the Sun's surface can be determined by the analysis of photospherical absorption lines.

of the deep interior of the Sun it will be possible to determine the inner metallicity and compare it with the one in the photosphere. In this way we will test one of the key assumptions of the standard Solar Model, i.e. the chemical homogeneity of the early Sun.

1.3 ^{14}N(p,γ)^{15}O reaction cross–section measurements

The ^{14}N(p,γ)^{15}O reaction (Q–value=7.297 MeV) has been deeply investigated in the recent years, especially by the LUNA collaboration. Fig. 1.7 (taken from (4)) shows the level structure of ^{15}O and, for each level, the corresponding energy relative to the threshold energy for the reaction. This reaction has been studied in detail in the laboratory (21, 22, 23, 24, 25, 26, 27, 28) and the contributions of the different γ–ray transitions in the capture process (Fig. 1 in (29)) have been disentangled (through the use of high–resolution Ge detectors). These experiments cover a proton energy range between 70 and 480 keV in the center of mass, hence far from the solar Gamow window centered at 27 keV. Five different radiative capture transitions contribute

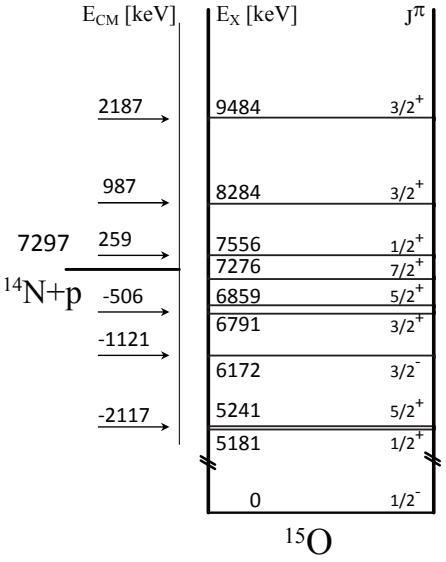

Figure 1.7: Level structure of ^{15}O - Lowest known levels of the ^{15}O nucleus. For each of them, excitation energy (E_x) and angular momentum (J^π) are indicated. The energy of the levels with respect to the threshold energy for the ^{14}N(p,γ)^{15}O reaction is indicated on the left side.

to the cross section at low energy: to the ground state and to the 6.79, 6.17, 5.24 and 5.18 MeV excited levels. When evaluating the total S–factor, the sum of the S–factors corresponding to each of these transitions has to be considered. A summary of the available experimental data (below 200 keV center of mass energy) in terms of S–factor is reported in Fig. 1.8. LUNA was able to measure the cross section down to 70 keV (23, 24, 25) (red points in the picture). Despite this valuable extension of the experimental data to lower energies, the available data are still far from the Gamow energy, peaked at E_0 =27 keV and with a FWHM of about 7 keV (approximating the distribution in Fig. 1.3 as a gaussian). The R–matrix fit to this extended data set

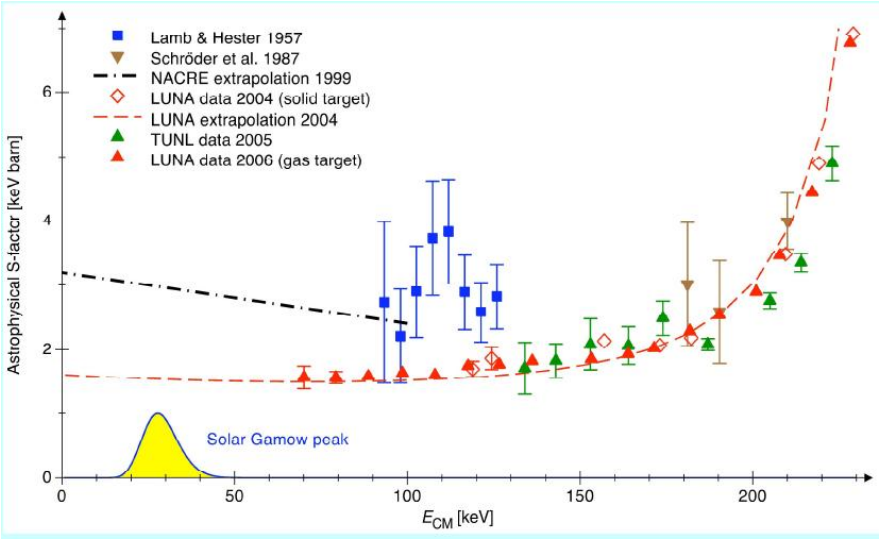

Figure 1.8: S–factor vs Energy for the ^{14}N(p,γ)^{15}O reaction - Astrophysical S–factor as a function of the center–of–mass energy for the ^{14}N(p,γ)^{15}O reaction. The points refer to the available experimental data (see legend). The solar Gamow energy peak for the reaction is reported in yellow (in arbitrary units). The extrapolation performed on the data set extended to 70 keV (27) (dashed red line) is a factor of two smaller then the NACRE evaluation (dashed black line).

provided an extrapolated astrophysical S-factor $S_{tot}(0) = 1.57 \pm 0.13$ keV barn (27), corresponding to $\sigma \approx 1.03 \times 10^{-19}$ (from Eqn. 1.1, $S(E) = \sigma E \exp(212.4/\sqrt{E})$). This cross–section is about a factor 2 smaller than the previous extrapolation in the NACRE compilation (30). The astrophysical consequences of such a reduction are significant. In particular, the CNO neutrino yield in the Sun is decreased by about a factor two (31, 32) and the estimate of the age of the oldest Globular Clusters is increased by

0.7-1 Gyr (to about 14 Gyr, (33)).

For the ^{14}N(p,γ)^{15}O reaction, it has been shown that the uncertainty on the total S–factor at zero energy is strongly dominated by the width Γ of the sub–threshold resonance at E=-506 keV, corresponding to the 6.79 MeV state in ^{15}O ((5, 34) and references therein). Several experiments have been therefore performed to determine as accurately as possible the width Γ of this nuclear level, that is, its lifetime $\tau = \hbar/\Gamma$.

1.3.1 The width of the sub–threshold resonance at -506 keV, i.e. the lifetime of the 6.79 MeV state in ^{15}O

An error below 5% on the determination of the ^{14}N(p,γ)^{15}O reaction cross–section is required in order to determine the metallicity of the central region of the Sun (where fusion reactions take place) by comparing the detected CNO neutrino flux with the predicted one (13). The cross–section for the capture to the ground state ($S_{GS}(0)$) is coming from the interference between the sub–threshold resonance at -506 keV and the direct capture reaction. The adopted value for the width of this resonance is $\Gamma = (0.9 \pm 0.2)$ eV, corresponding to $S_{GS}(0) = 0.20 \pm 0.05$ keV barn (27), used for the determination of the new extrapolated S–factor discussed above. The importance

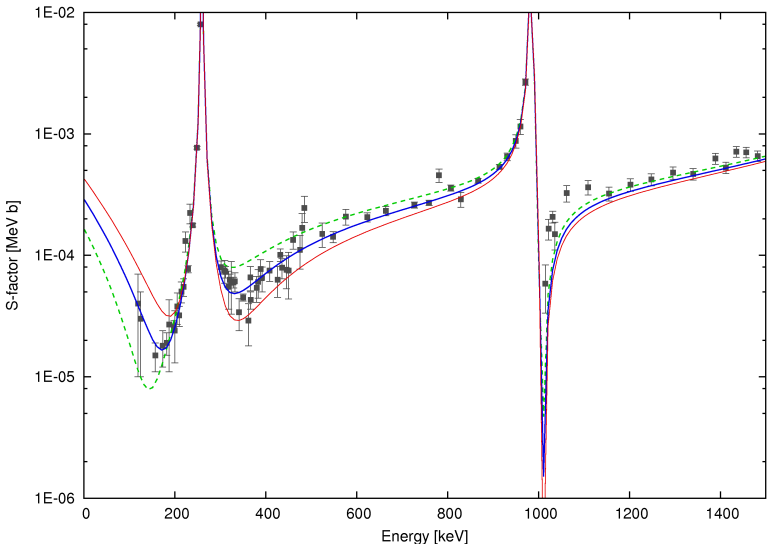

Figure 1.9: Extrapolation of the ^{14}N(p,γ)^{15}O reaction cross–section to Gamow energies - Influence of the width of the -506 keV sub–threshold resonance of the extrapolation of the S–factor at Gamow energies for the ^{14}N(p,γ)^{15}O reaction (34).

of an accurate determination of the width of this resonance is illustrated in Fig. 1.9 (34, 35). By changing the width by 20% (corresponding to the indetermination in the current adopted value) a variation in the extrapolated S–factor at zero energy of about 30% is obtained. To decrease the error on the R–matrix fit it is necessary to better determine the width of the sub–threshold resonance corresponding to the 6.791 MeV state of ^{15}O (4).

1.4 Existing literature for the lifetime of the 6.79 MeV state in ^{15}O : why is a new evaluation needed

The results available in the literature to date for the lifetime of the 6.79 MeV state in ^{15}O and the corresponding width and S factor at zero energy are reported in Tab. 1.1.

group/year (method)	τ [fs]	Γ [eV]	$\Gamma/\Delta\Gamma$ [%]	$S_{GS}(0)$ [keV barn]
Oxford 1968 (36) (DSAM d(^{14}N,^{15}O)n)	< 28	> 0.02	–	–
TUNL 2001 (37) (DSAM ^{14}N(p,γ)^{15}O)	1.6±0.7	0.41±0.17	44	0.12-0.45
RIKEN 2004 (38) (CE ^{208}Pb(^{15}O,^{15}O*))	< 1.8 fs	> 0.36	–	–
LUNA 2004 (23) (R–matrix fit)	1.1±0.5	0.6±0.3	45	0.25±0.06
TUNL 2005 (26) (R–matrix fit)	0.3±0.1	2.2±0.7	33	0.49±0.08
Bochum 2008 (39) (DSAM ^{14}N(p,γ)^{15}O)	<0.77	> 0.85	–	–
LUNA 2008 (27) (R–matrix fit)	0.75±0.20	0.9±0.2	26	0.20±0.05

Table 1.1: Summary of the results on the lifetime of the 6.79 MeV state in ^{15}O present in the literature The different results obtained by the various collaborations are reported. Where it is possible, the corresponding relative error and obtained $S_{GS}(0)$ are indicated. The direct methods for the lifetime measurement are shown in red. The presently adopted width and $S_{GS}(0)$ are underlined.

We can see that, on the basis of what has been discussed before, the uncertainty is still too high. Some of the results listed in the table are obtained from an "indirect" determination of the width, extracted as a parameter from the R–matrix fit to the reaction data (23, 26, 27). In order to increase the accuracy in such extrapolation, it is of paramount importance to determine this quantity "directly" and use it for the R–matrix fit as a fixed, precisely known, value.

In the experiment performed at RIKEN (40), the radiative width was measured in an intermediate–energy Coulomb excitation experiment (38). The γ rays emitted

from the de–excitation of the scattered ^{15}O nuclei –produced by fragmentation– were detected with an array of scintillator detectors (NaI(Tl)). The result was obtained by comparing the γ energy spectrum with the results of Monte Carlo simulations, which was needed in particular in order to disentangle the 6792 keV peak of interest from the 6859 keV one (second $5/2^+$ to g.s. transition, Fig. 1.7). These peaks were indeed difficult to separate in the γ spectrum due to the poor energy resolution of the detector system. The obtained upper limit can serve, anyway, as a validation of independent evaluations resulting from different techniques.

The direct methods for the lifetime measurement are given in red in Tab. 1.1. For the determination of the lifetime of the level of interest the Doppler Shift Attenuation (DSA) technique (see Sec. 2.1.1.1) is used. The lifetime is thus obtained by looking at the Doppler shift effects in the γ spectrum recorded at different angles with respect to the direction of motion of the emitting nuclei, while they are slowing down in a given material. The lifetime has thus to be comparable with the characteristic slowing–down time of the stopping material. As we will extensively discuss in the body of this Thesis, in the fs region we are at the limit of sensitivity of this technique so that well defined experimental conditions are needed in order to minimize the systematic errors.

The experiments reported in the literature for the direct measurement of the lifetime of the 6.79 MeV state in ^{15}O are of two kinds, differing by the reaction used to populate the level of interest:

^{14}N(p,γ)^{15}O (direct kinematics reaction): in the experiments described in (37, 39) the 6.79 MeV state in ^{15}O is populated from the 259 keV resonance following the ^{14}N(p,γ)^{15}O reaction and the lifetime has been evaluated from the shift of the baricenter of the γ peak observed at different angles. In (36), the γ rays were detected with three 60%–efficiency HPGe detectors placed at 11 cm from the target and positioned at $0, 90, 144^o$ with respect to the beam direction. The emitting nuclei were recoiling with $\beta \approx 0.16\%$, resulting in a maximum Doppler shift (at 0^o, Eqn. 2.3) of ≈ 110 keV (over 6.79 MeV).

In (39) the combination of angles was increased by placing a single HPGe detector on a rotating frame (from 40 to 116^o), allowing for a check of eventual asymmetries. The proton beam was delivered at 318 keV, resulting in a velocity of the emitting nuclei $\beta \approx 0.06\%$.

d(^{14}N,^{15}O)n (inverse kinematics reaction): the reaction in inverse kinematics, the one adopted in the present Thesis work, was used in an experiment performed 50 years ago (36). A 22 MeV beam energy was used, i.e. $\beta \approx 6\%$, resulting in a Doppler shift of the gamma of interest at 0 degrees of about 420 keV. The gamma rays were measured in a Ge(Li) detector and different stopping materials were used in order to have independent evaluations, thus reducing the uncertainties due to the indetermination on the nuclear stopping powers. The upper limit on the lifetime of the 6.79 MeV state in ^{15}O reported in Tab. 1.1 is obtained from the lineshape analysis of the γ peaks. The corresponding spectra are, however, not shown in the article (only the lineshape fit for the single escape peak of the 7.30 MeV line in ^{15}N , also populated in the same reaction process).

As we will extensively argument throughout the Thesis, from the point of view of the DSA experimental requirements the choice of the reaction and analysis technique reported in (36) seem optimal for pushing the lifetime measurement method at the limit of its applicability. On the other side, the value and limit proposed in (37) and (39), respectively better agree with the indirect results achieved with the R–matrix fits. Moreover, a hint of the order of magnitude for the lifetime of the considered level can be obtained from nuclear structure considerations: the analogous level (second $3/2^+$) in the isospin symmetric ^{15}N nucleus is the level at 7.3 MeV and its lifetime is (0.61±0.06) fs (41). On the basis of the isospin symmetry, the lifetime of the analogous state in ^{15}O should lie in the same energy range.

Is the limited "success" of the Oxford group experiment related to the poor γ–ray detection performance or are there intrinsic limitations of the used technique when pushed at the limits of its applicability?

On the other side, the solution of fundamental astrophysical problems, such as the *solar composition problem*, demands for a more accurate determination of the width of the sub–threshold resonance corresponding to the 6.791 MeV state of ^{15}O, i.e. of its lifetime, as stressed in the last review about the solar fusion cross sections, by Adelberger et al. (4).

1.5 Thesis outline

In this Thesis the data analysis and results of a new dedicated experiment to perform a direct measurement of the lifetime of the 6.79 MeV level in ^{15}O will be presented[1]. Preliminary results from this work have been presented at International Conferences and Workshops, see for instance (44).

After the presentation of the astrophysical interest of such a measurement, given in the present Chapter, the experimental techniques used in this work will be outlined in Chapter 2. We will give a quick overview of the methods to measure short nuclear lifetimes in unstable nuclei, in particular to the techniques based on the Doppler shift effects. Emphasis will be given to the Doppler Shift Attenuation Method and to all the optimizations we had to adopt to push such a method to the femtosecond limit. The state-of-the-art detection device that has been used, namely the AGATA Demonstrator array, will be described, after a quick overview of the innovative Pulse Shape Analysis and γ-ray tracking techniques which have been developed in the last years.

The complex sequence of operations needed in order to extract the relevant information from the raw data produced by AGATA will be described in Chapter 3. As a matter of fact, the behaviour of modern highly–segmented HPGe detectors is quite unlike the "conventional" detectors, meaning that several corrections are required before extracting information with full quality from the raw data. It should not be forgotten that in modern devices such as AGATA most of the "traditional" signal processing is replaced by software filtering.

Chapter 4 will deal with the Monte Carlo code that was developed and used. In order to combine the existing `Geant4` code for AGATA with the possibility of treating the effects of nuclear deexcitation with finite lifetime, the `Geant4` libraries had to be extensively modified. The resulting simulation code was tested by successfully reproducing known experimental cases.

The actual lineshape analysis will be described in Chapter 5. The validity and soundness of our analysis method was first tested on "known" cases, namely on levels

[1] Another experiment for the measurement of the lifetime of the 6.79 MeV state in ^{15}O has been performed at the TRIUMF facility (42), using the ^{3}He+^{16}O$\rightarrow \alpha$+^{15}O reaction at 35 MeV beam energy, selected by detecting the α particles. In (43), the spectrum for the 6.79 MeV gamma line observed at 0 deg is shown, as coming from a preliminary analysis. No estimation of the lifetime, nor lineshape analyses are given.

in ^{15}N populated in the same reaction as the 6.79 MeV level of interest in ^{15}O. The results will be presented.

Finally, the results will be briefly discussed in the Conclusions.

2

Experimental method and setup

Is it possible to improve the measurement of the lifetime of the 6.79 MeV state in ^{15}O and to reduce its uncertainty? In this Chapter, the framework of a new dedicated experiment will be outlined. The first application of state–of–the–art spectroscopic tools to the detection of high–energy gamma–rays of astrophysical interest will thus be introduced. Implementing innovative techniques for the γ–ray detection and data analysis, a far much larger inspecting power is expected with respect to the previously performed experiments (see Tab. 1.1, Chap. 1).

2.1 The Doppler Shift Attenuation method for the measurement of nuclear level lifetimes

In the study of the gamma rays emitted by excited nuclei during their de–excitation path to the ground state, the transition probability between two levels is one of the most important probes of the structure of the states involved. The strong force is the dominant interaction between nucleons and governs the behaviour of the nucleus. The electromagnetic interaction operators have a well-known structure (45) and only weakly perturb the strong nuclear interaction. Hence, it is possible to compare experimentally determined γ-ray reduced transition probabilities between nuclear states with the theoretical predictions of nuclear models. This is one of the most sensitive tools available to investigate the structure of the wave–functions characterizing the nuclear excited states (46). The lifetime of a nuclear state is the observable that is measured in gamma–ray spectroscopy experiments in order to derive the reduced transition proba-

bilities. Measurement methods have thus been developed in order to determine either the lifetime τ of a given nuclear level or the width Γ of the metastable state. These two quantities are intimately bound by the relation:

$$\Gamma = \hbar/\tau \tag{2.1}$$

The determination of the lifetime of an excited nuclear level is therefore an indirect measurement of the width of the same level.

The total width Γ of a state is obtained by summing up the partial widths associated to the various decay processes it experiences, each of them correlated to the transition matrix element between the initial and final state (46). If the excited level of interest belongs to a stable nucleus, its width can be measured via the absorption of a photon (*resonance fluorescence*) or Coulomb excitation on the ground state. If the populated level decays back to the ground state via different γ patterns, only the partial width is measured. In the case of excited levels populated via nuclear reactions, there are several ways to directly measure the lifetime τ of a given level. In the simplest case of a particular nuclear level populated at $t = 0$, the corresponding *decay function* is:

$$n(t) = n_0 \exp \frac{-t}{\tau} \tag{2.2}$$

where $n_0 = n(0)$ is the number of nuclei excited at $t = 0$.

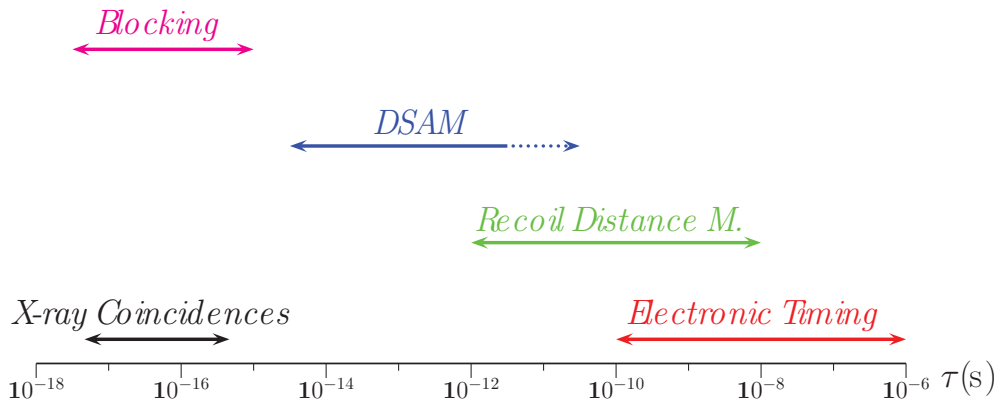

Figure 2.1: Main lifetime measurement techniques - Approximate range of application of the main techniques for the measurement of the lifetime of excited nuclear levels (53). The DSAM (Doppler Shift Attenuation Method) and RDM (Recoil Distance Method) are marked in blue and green respectively.

nucleus	E^* [MeV] (spin [$\hbar$])	τ	method (Ref.)
^{15}N	7.30 ($3/2^+$)	0.61±0.05 fs	resonance fluorescence (47)
		0.25±0.05 fs	inelast. electron scattering (48)
^{15}N	8.30 ($1/2^+$)	1.7±1.1 fs	resonance fluorescence (47)
		$<$ 16 fs	DSAM (48)
^{15}N	9.05 ($1/2^+$)	0.50±0.08 fs	resonance fluorescence (47)
		$<$ 2 fs	DSAM (48)
^{15}N	10.06 ($3/2^+$)	0.104±0.007 fs	resonance fluorescence (47)
^{15}O	6.86 ($5/2^+$)	16.0±2.5 fs	DSAM (49)
^{15}O	7.27 ($7/2^+$)	1.2±0.3 ps	DSAM (50)

Table 2.1: Examples of lifetime measurements in ^{15}O, and ^{15}N - Techniques used to measure the lifetime of some of the excited levels in ^{15}O, ^{15}N. E^* is the excitation energy. Adopted energies and their uncertainties reported in (41). The adopted values for the spectroscopic observables in the A= $13-15$ mass region are compiled in (51). The table is similar to the one reported in (52).

The lifetimes of nuclear states decaying via emission of gamma radiation typically lie in the 10^{-16} to 10^{-3} s interval, depending on the strength and on the energy of the transition. Different methods and analysis techniques have been developed in the last decades (see, for example, (54) for more details). The lifetime ranges covered by some of the main methods are reported in Fig. 2.1. Among these, the Doppler shift techniques are powerful tools for lifetimes in the $10^{-14} - 10^{-8}$ s interval. The basic elements of the Doppler Shift Attenuation method, the one used in this Thesis, will be recalled in the next section.

Examples of the different techniques used to measure the lifetime of excited states in nuclei belonging to the A$\approx$ 15 mass region –of interest in the present work– are reported in Tab. 2.1.

2.1.1 Doppler Shift techniques

When the nuclear level of interest is populated in a heavy–ion[1] reaction, the finite time it takes the reaction product to travel a given distance can be considered as a "unit of measure" of the decay lifetime of the populated level(s). When the radiation with energy E_γ (center of mass energy) is emitted by a nucleus moving with a velocity

[1]With "heavy ion" one refers to the nucleus of an element with Z>4.

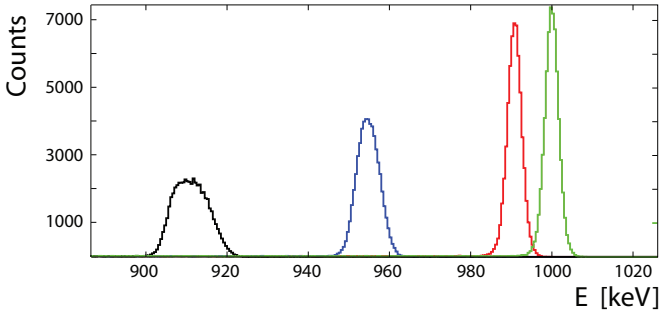

Figure 2.2: Effect of different recoil velocities on the observed γ peak - Simulated spectra for a 1 MeV energy γ line, emitted by a nucleus travelling in a fixed direction (0 degrees) with different $\beta = v/c$: 0 in green, 0.01 in red, 0.05 in blue, 0.1 in black. The gamma rays are observed at backward angles (158 degrees).

$\vec{\beta} = \vec{v}/c$, the gamma–ray energy observed at an angle θ between the recoil and the γ–ray emission directions follows the Doppler relation:

$$E'_{\gamma} = E_{\gamma}\frac{\sqrt{1-\beta^2}}{1-\beta cos\theta} \tag{2.3}$$

where $\beta = \|\vec{\beta}\|$. The effect of different recoil velocities on the γ–ray peak observed by a finite–size detector is shown in the simplified case of Fig. 2.2. Here the emitting nuclei travel along the beam direction (a good approximation in the case of fusion–evaporation reactions) with different recoil velocities, ranging from β =0 (emission at rest) to β =0.1. The gamma rays are detected at backward angles with respect to the beam axis and, as the recoil velocity increases, the peak centroid shifts to lower energy, according to Eq. 2.3, and broadens.

Depending on the order of magnitude of the lifetime and on the kind of nuclear reaction involved, different variants of the technique have been developed. For instance, in the case of the neutron–rich nuclei produced in nucleon–transfer reactions (key point of the recent experimental nuclear structure campaign at the Legnaro National Laboratories, as explained later) the *Differential plunger* method (55) is used. In this particular case of *Recoil Distance Method* (RDM), a "thin" layer of material (degrader) is placed after the production target in order to slow down the emitting nuclei and observe two components in the γ spectrum, corresponding to two different velocities of the emitting nuclei. The lifetime is obtained from the intensity ratio between these two components as a function of the distance between the target and the degrader. While nucleon

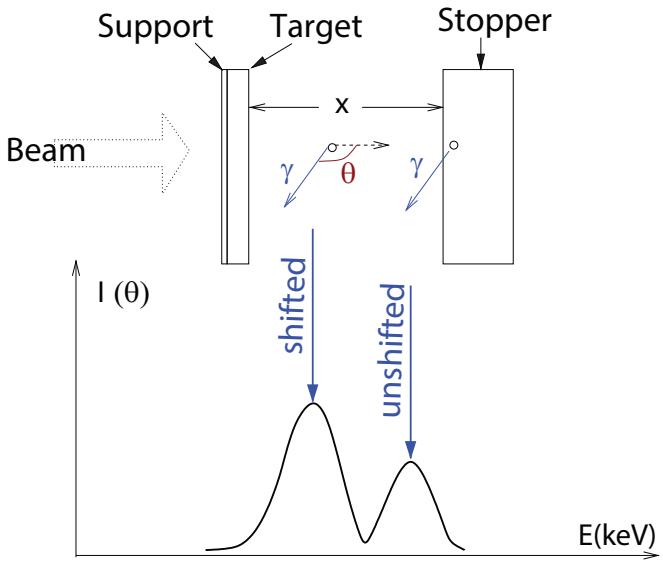

Figure 2.3: Recoil distance method (plunger) - Schematic representation of the setup for a Recoil Distance experiment. When the γ rays are emitted in flight (and observed at $\theta > 90^{o}$) the peak is lowered in energy, according to Eqn. 2.3.

transfer reaction mostly populate low lying states, the lifetime of low and high–spin states can be determined when possible using fusion–evaporation reactions where the recoils are stopped in the second "thick" layer (*plunger* (55, 56, 57)). The produced nuclei are assumed to travel along the beam direction (good approximation for this kind of reactions) and the intensities of the shifted and unshifted components in the gamma spectrum are evaluated, see Fig. 2.3. The range of applicability of the RDM (*Recoil Distance Method*, i.e. the plunger measurements) is in the ps–hundreds of ps time interval (Fig. 2.1).

The methods discussed above take great advantage of the the use of HPGe detectors, whose excellent energy resolution allows for the observation of fine details in the γ energy spectrum. In particular, a big improvement in the accuracy of the determination of the lifetimes by means of these techniques was achieved with the use of arrays of HPGe detectors, placed symmetrically all around the target position. The possibility of a simultaneous measurement at many angles is important for discovering the presence of contaminations as well as for increasing the accuracy since the lifetime is obtained in a number of independent evaluations.

In addition, it is worth noting that analysis techniques based on gamma coincidences

allow to reduce systematic errors related to the *side feeding* (55), i.e. the population of the state of interest via intermediate (unobserved) levels of poorly or completely unknown lifetime. The occurrence of unobserved feeders results in additional parameters in the solution of the Bateman equations and frequently compromises the accuracy on the measured lifetime.

2.1.1.1 Doppler Shift Attenuation (DSA) method: lineshape analysis

When the lifetime of the level of interest is comparable to the slowing down time of the emitting nucleus in a given material, the Doppler Shift Attenuation Method (DSAM) (54) is used. This technique is widely adopted for the measurement of sub–ps lifetimes (Fig. 2.1), corresponding to the typical slowing down times of heavy ions in solid mediums, which are $\approx 10^{-13} \rightarrow 10^{-12}$ s for kinetic energies below or about 10 MeV per nucleon. In Fig. 2.4 the slowing–down times of ^{15}N ions in different materials for two different initial energies as a function of the energy are reported. The accuracy attainable in the determination of the lifetime with this method is limited by mainly two phenomena:

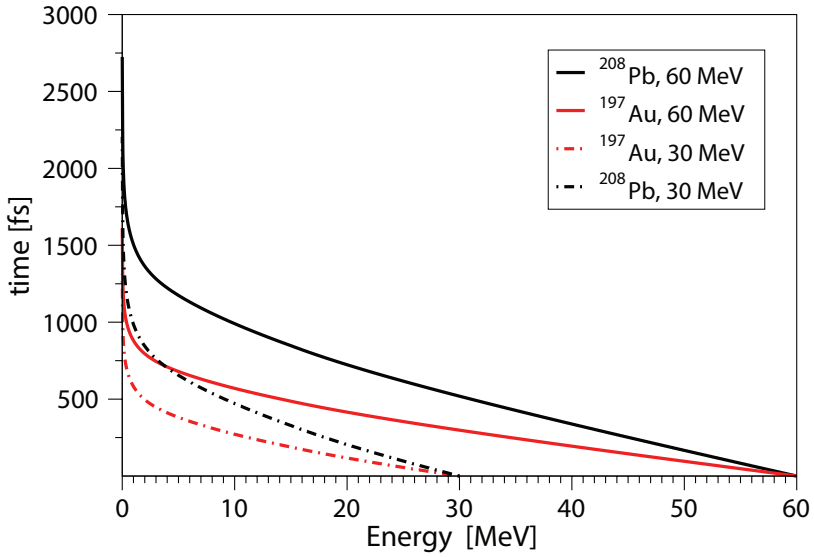

Figure 2.4: Examples of slowing–down times - Stopping times for ^{15}N ions in lead and gold for two different initial energies as a function of the energy. The stopping power in gold is larger with respect to lead.

- the indetermination on the stopping powers, in particular at low velocities (systematic errors up to 10–15%);

- the total or partial lack of knowledge of the population pattern of the level of interest (*side feeding*), when the measurement does not involve proper multiple gamma coincidences (58, 59).

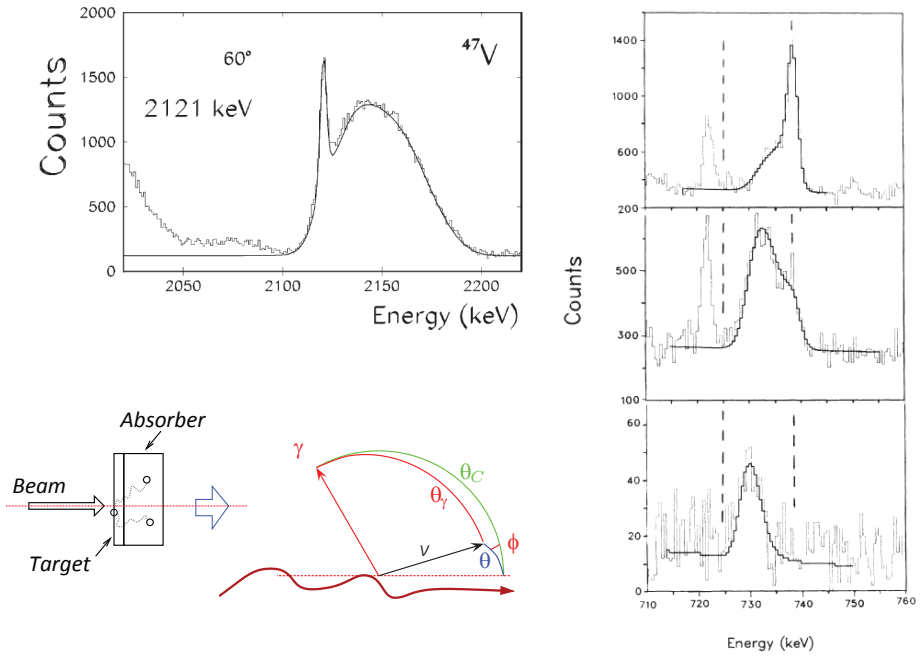

Figure 2.5: Doppler Shift Attenuation Method - Schematic representation of the working principle of a typical DSAM experiment (lower left) and examples of measured γ–ray lineshapes taken from the literature. The nuclei produced by fusion–evaporation in the target layer slow down in the absorber. The γ rays are emitted at different velocities $\vec{v}$. θ_γ is the angle between the recoil and emission directions, θ and ϕ are the polar angles of the recoil (referred to the beam direction). Upper left panel: $31/2^- \rightarrow 27/2^-$ 2121 keV γ transition in ^{47}V measured at 60º (detectors of the GASP array). The nuclei were excited in the ^{28}Si+^{28}Si reaction at 115 MeV beam energy –$\beta_{^{47}\mathrm{V}} \approx 4.5\%$– and the target consisted of 0.8 mg/cm^2 Si on 15 mg/cm^2 Au backing. The lifetime of the $31/2^-$ level is 0.37(3) ps (60). Right: $24^+ \rightarrow 22^+$ γ transition (738.5 keV) in ^{166}Dy, measured at ≈150º. The ^{40}Ar+^{130}Te reaction at 180 MeV was used –$\beta_{^{166}\mathrm{Dy}} \approx 4.8\%$– with three different absorbers, Au, Pb and Mg, from top to bottom. The dashed vertical lines indicate fully shifted and stopped peak positions (61).

In a typical DSAM experiment (schematic representation in Fig. 2.5), the excited nuclei are produced in the target and an additional layer (stopper) is used to enhance the slowing–down effects. The de–excitation of the nuclear states populated in the reaction process takes place at different velocities, as a function of the distance travelled at the time of the γ emission, due to the slowing–down caused by the interaction with the atoms in the target/absorber layer. Thus, according to Eq. 2.3, the γ rays emitted by nuclei moving with different velocities are detected with different energies. Being the slowing down process continuous and the gamma–ray emission statistical, the detected gamma energy spectrum corresponding to a particular transition is a continuous distribution ranging between the nominal rest energy and the maximum Doppler shift (Doppler broadened peak). Clearly, the shape of the distribution (*lineshape*) depends on the lifetime of the level, on the kinematics of the emitting nucleus and on the slowing–down properties of the absorbing medium. In Fig. 2.5, examples of lineshape analyses taken from the literature are reported, together with the schematic representation of the principle at the basis of the method. The spectrum on the upper left part is taken from (60) and corresponds to the lineshape analysis of the $31/2^- \rightarrow 27/2^-$ γ transition in ^{47}V. The γ rays are observed at forward angles and the emitting nuclei are travelling at $\beta \approx 4.5\%$ (see figure caption for more details). The effects of the lifetime (0.37(3) ps) and of the slowing down in the Au absorber result in a stopped peak at the rest energy of 2.12 MeV, followed by a "bump" corresponding to nuclei emitting while slowing down, up to the maximum Doppler shift. To the right, the γ–ray lineshapes of a transition of 738 keV energy observed at backward angles and in correspondence to different absorber materials are reported, taken from (61). Such ^{166}Yb gamma line is emitted by nuclei recoiling with $\beta \approx 4.8\%$. The spectra are presented in order of decreasing stopping power from top to bottom.

The shift of the centroid of the gamma peak in the energy spectrum as a function of the observation angle can be also used for the evaluation of the lifetime (62). In this way, only the first moment of the projection of the velocity distribution along a given direction is considered. A more accurate determination of the lifetime can be obtained by using the information of the whole distribution and performing a *lineshape analysis* of the DSA data.

All the modern lineshape analysis programs follow the pioneering work by M.C. Currie and co–workers (63). The lifetime of a nuclear level is determined by a comparison

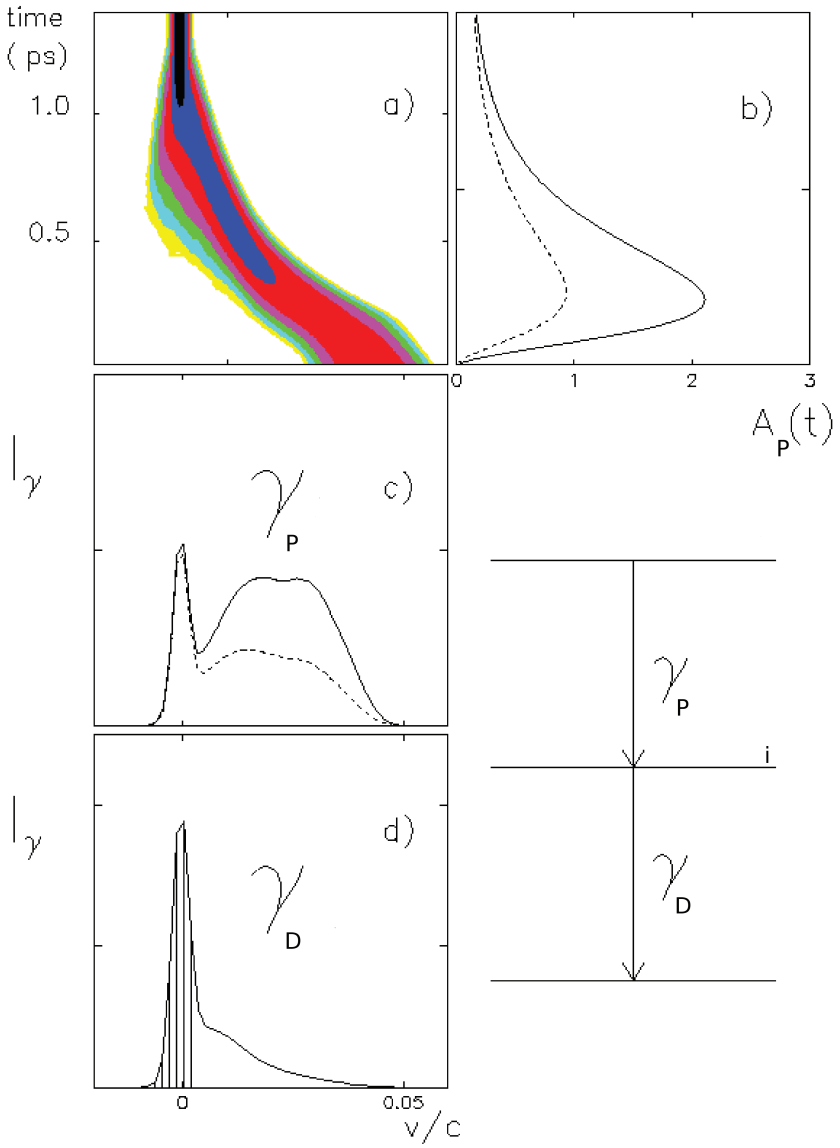

Figure 2.6: Stopping matrix and lineshape analysis - (Taken from (59).) a) Simulated time–velocity distribution, i.e. $D(t, v_\theta)$ (see text), for the γ_F transition. The figure was used in the original paper to illustrate a particular analysis method. In our context this is taken as an example of stopping matrix. In b) the projection on the time axis, i.e. the decay function for the F level, is reported (solid line) while in c) the one on the β axis, connected to the γ energy by the Doppler relation.

(via a χ^2 analysis) between the experimental lineshape and the one generated with a Monte Carlo simulation of the slowing–down process[1]. Following the setup represented in Fig. 2.5 and the simplified case of a two–level gamma cascade, as represented in Fig. 2.6, the gamma ray de–exciting the level i, observed at an angle θ between the recoil and γ emission directions, will be observed with an energy distribution resulting in a lineshape $\mathcal{P}(v_\theta)$ (blue spectrum in Fig. 2.7), that is intrinsic (recorded by an "ideal" detector). The correlation between the distribution of the projections of the velocities along the observation direction and the level decay function is accounted for in the *stopping matrix*:

$$\mathcal{P}(\theta) = \int_0^\infty P(t, v_\theta)\frac{n_i(t)}{\tau_i}dt \equiv \int_0^\infty \mathcal{D}(t, v_\theta)dt \tag{2.4}$$

An example of $\mathcal{D}(t, v_\theta)$ correlation is given in Fig. 2.6 (a). The observed gamma lineshape with a "real" detector is given by the convolution of the intrinsic lineshape and the detector response function, $\Phi^\theta(E_\gamma, E_\gamma^{'})$, which includes the experimental detection constraints (black spectrum in Fig. 2.7). It indicates the probability to detect a gamma ray of energy $E_\gamma^{'}$ when E_γ is firing. Ideally, this should be a Dirac delta function: in practice it is represented by a gaussian:

$$\Phi^\theta(E_\gamma, E_\gamma^{'}) = \frac{1}{\sigma\sqrt{2\pi}}e^{-\frac{(E_\gamma - E_\gamma^{'})^2}{2\sigma^2}} \tag{2.5}$$

with $\sigma = FWHM/2.35$, experimentally determined from the width of the gamma

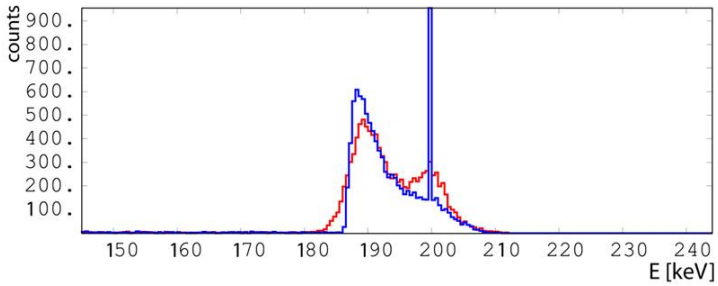

Figure 2.7: Intrinsic and measured lineshape - Example of convolution of the intrinsic lineshape of a peak in the gamma spectrum (blue) and detector response function. The resulting spectrum (red) is the one that is measured in DSAM experiments.

[1] As discussed in Sec. 4.3, for the analysis of our data we developed a Monte Carlo code that takes also the γ emission and detection into account. The detector response function is also determined from a MC simulation of the actual detector set–up.

peaks under ideal conditions (not Doppler shifted/broadened –i.e. emitted at rest– and properly calibrated.

The lineshape techniques rely upon the Monte Carlo simulations of the slowing–down and scattering processes of each ion, travelling in the solid medium, as described in the following.
The starting position is randomly chosen in the target layer and the slowing–down process in the medium is thus followed recording at each step j the velocity vector ($v_x(t_j)$, $v_y(t_j)$,$v_z(t_j)$), evaluated at definite time intervals (*stepping time*). The number of velocity histories and the stepping time have to be chosen in a way to adequately sample the lineshape (and according to the available computing resources). The starting velocity is computed taking into account the reaction kinematics and considering the slowing down of the projectile up to the starting point. The gamma–ray emission moment is attributed randomly inside the decay distribution, while the entering angle of the emitted γ ray into the detector is considered uniformly distributed over the covered solid angle. The recorded energy is obtained by weighting the value resulting from Eq. 2.3 with the detector response function. The energy–loss in the path travelled by the emitting nucleus is taken into account on the basis of available data/parametrization for the stopping powers (64). For $\beta_{recoil} \gtrsim 2\,\%$, the stopping power is mostly ruled by the interaction with the atomic electrons of the medium (*electronic part* of the stopping–power) and its determination is based on the semiempirical table edited by Northcliffe and Schilling (65) for heavy ions, and later revised, on the basis of experimental measurements, by Ziegler and Chu (1974) (66) and Ward et al. (1976) (67). For lower energies one has to rely on theoretical models, among them the commonly used Lindhard, Scharff and Schiott (LSS) theory (68). Due to the lack of experimental data at these energies, the corresponding stopping powers are not well determined and this is one of the main sources of uncertainty in the lineshape analyses.

Summarizing, the key ingredients and the main sources of uncertainties for a lineshape analysis are:

- proper stopping material and modeling of the stopping power
- knowledge/definition of the kinematics
- proper modeling of the side–feeding

- "good" and well known detector response function

2.1.1.2 Pushing the DSA technique to the *femtosecond* limit

As represented in the diagram of Fig. 2.1 and on the basis of what has been recalled in the previous section, it is clear that the DSAM measurement of lifetimes in the fs region, as required by the physics case treated in this Thesis, is quite demanding. On the other side, this is the only technique nowadays available for the measurement of such a lifetime. ^{15}O is not a stable nucleus, so that techniques like the *resonance fluorescence* (mentioned earlier), more suitable in this lifetime range, cannot be used. The Coulomb–excitation of the 6.79 MeV level suffers from a quite low probability on one side and on limitations due to the interpretation of the results on the other side, as one can see from the Riken group attempt (see Sec. 1.4 and (38)).

In order to push the previously described method to the fs region, i.e. to the limit of its applicability, all the aspects listed at the end of the previous section should be fulfilled in the best way. In case of "short" lifetimes, the shape of the peak in the gamma spectrum is mainly determined by the kinematics, since most of the nuclei decay as soon as they are produced. For different lifetimes one can see a "small" deviation from the fully Doppler shifted energy range, as it is shown in the left side of Fig. 2.8. In this figure, 6.79 MeV γ rays emitted by ^{15}O nuclei produced in the direct mechanism reported in the figure are simulated corresponding to different fs lifetimes. The detector considered in this simulation covers an angle of two degrees around 160^{o} with respect to the beam direction (mimicking the situation we will have from the analysis of our data, Sec. 5). The same data simulated in case of a traditional HPGe detector ($\approx 6^{o}$ angular coverage), as one on the most forward ring of the GASP array, give the spectra presented on the right side of Fig. 2.8. While in the former case the peaks differing by a few fs can be distinguished, in the latter no difference is evident between the two peaks at 1 fs and 5 fs.

The experimental requirements to be fulfilled can thus be summarized as follows:

1. maximization of Doppler shift effects: recording on more channels of the gamma spectrum the expected lineshape allows for a better sensitivity to lifetime differences;

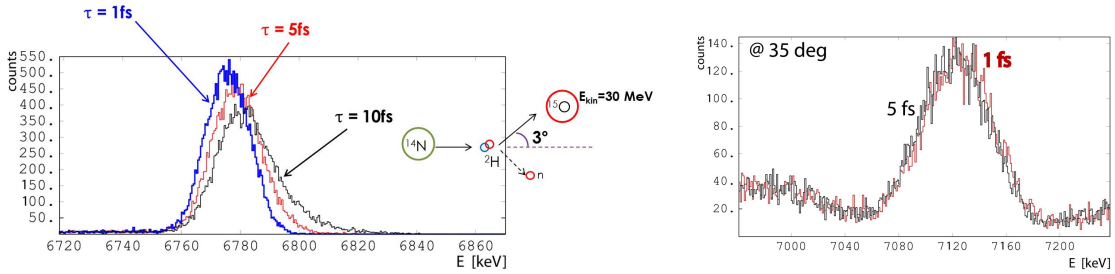

Figure 2.8: Sensitivity to fs lifetimes - 6.79 MeV γ rays emitted by ^{15}O nuclei produced in the simplify direct process reported in the figure. The sensitivity to $\approx$ fs lifetimes obtained in the spectra on the left (see text) is lost when using a traditional HPGe detector, as one from the GASP array.

2. large stopping power of the absorbing material: the "sooner" the emitting nuclei start being slowed down, the larger is the deviation of the observed shape from the fully Doppler shifted one, when changing the lifetime;

3. monitor of gain instabilities: as it results from Fig. 2.8, one expects small shifts that may be hidden by electronic shift effects;

4. high efficiency and resolution of the detectors system, i.e. good response function: the closer the response function is to a "δ", the less are lifetime effects smeared out.

While the first three points are related to the choice of the reaction and experimental conditions, the last point concerns the gamma–ray detection and will be discussed and introduced in the next section. It should be clear from the examples shown above that the determination of fs lifetimes with the DSAM technique is hardly feasible using "conventional" detection devices. Therefore, in the present work it was decided to rely upon a state–of–the–art device, namely the *AGATA Demonstrator*.

Before describing the details of the experiment, the basic concepts of such a device, the characteristics and purposes of the AGATA project are outlined.

2.2 Gamma–ray spectroscopy with segmented HPGe detectors: modern gamma–ray tracking arrays

Since germanium detectors became available in the 1960s, they constituted the most used and important tool for γ–ray spectroscopy. In particular, the modern High–Purity Germanium crystals (HPGe) provide a good ($\approx$keV) energy resolution in the energy range between 10 keV and 10 MeV, typical for nuclear spectroscopic studies. The continuous development of high–resolution γ–ray detector systems has been of vital importance to nuclear structure physics. It has steadily expanded the limits of what can be observed, allowing for the discovery of new phenomena and leading to

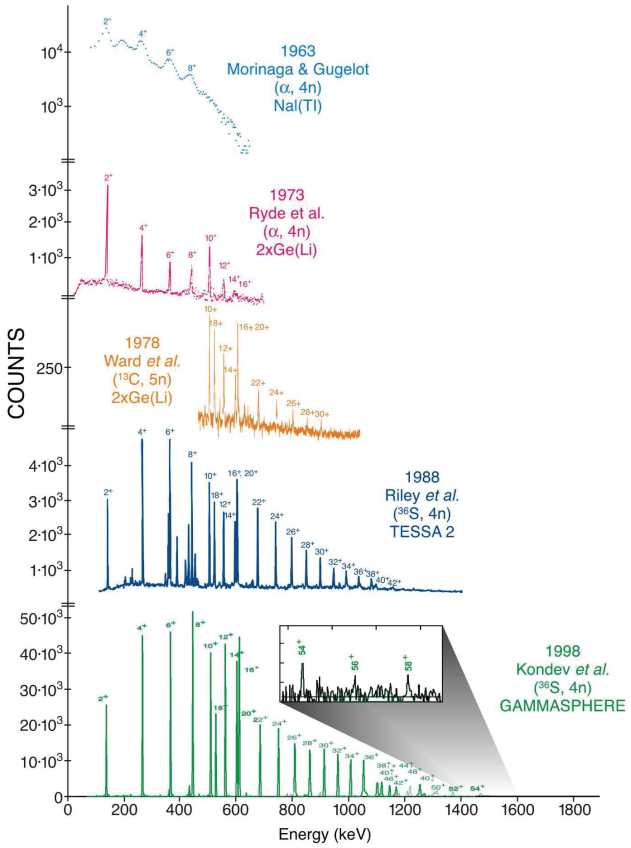

Figure 2.9: Spectroscopic history of the ^{156}Dy nucleus - Example (taken from (69)) of improvement in the spectrum quality with the evolution of γ–ray detection and acceleration techniques (see text). The spectra are taken from (top to the bottom) (67, 70, 71, 72, 73).

deeper insights into the nature of the nucleus. An example of this is provided by the "spectroscopic history" of ^{156}Dy, represented schematically in Fig. 2.9 (taken from (69)). The possibility to analyze weak gamma lines closely spaced in energy lead to the identification of new structures, in the study of nuclei at the limit of the angular momentum. The first significant advance that lead to the establishment of the yrast structure of this nucleus was the replacement of the scintillation–based detectors with semiconductors (first two spectra starting from above (70, 71)). The advent of heavy–ion accelerators in the 1970s made it possible to populate nuclei at high–spin states (third spectrum, from (67)). Higher–spin states and non–yrast bands were afterwards investigated with the use of the first array of HPGe detectors (around the 1980s, (72)). Discrete γ lines up to $58\,\hbar$ angular momentum were observed (73) thanks to the high detection efficiency and energy resolution of the array of HPGe Compton–suppressed detectors GAMMASPHERE.

Indeed, arrays of HPGe detectors became in the 1990s the state–of–the–art instruments for γ–ray spectroscopy, having not only a large photopeak efficiency, but also a high selectivity of the reaction channels of interest, through the analysis of multiple gamma coincidences. The key concept behind these arrays is to obtain the required selectivity (and efficiency) through the combination of several detectors, each of them with good response function (in other words, with energy resolution and P/T ratio both as good as possible). It should be strongly remarked that, since the photons are emitted by recoiling nuclei, the FWHM of the peak is dominated in most cases by the Doppler broadening due to the finite size of the detector, rather than the intrinsic detector resolution. This means that each element of the array should cover an as small as possible solid angle to keep this broadening within "reasonable" limits. Concerning peak–to–total ratio, the background generated by partially absorbed photons can be the dominant part of the spectrum for the available size of the HPGe crystals. Such background can be efficiently reduced by surrounding the Ge detectors with the so–called *Compton suppression shields*, namely veto detectors that can only detect photons escaping from the germanium crystal.

In Fig. 2.10 the sensitivity of the γ arrays –the reciprocal of the minimal fraction of the total cross–section that can be identified– is shown as a function of the years. The introduction of the Compton suppression and of large volume germanium crystals lead

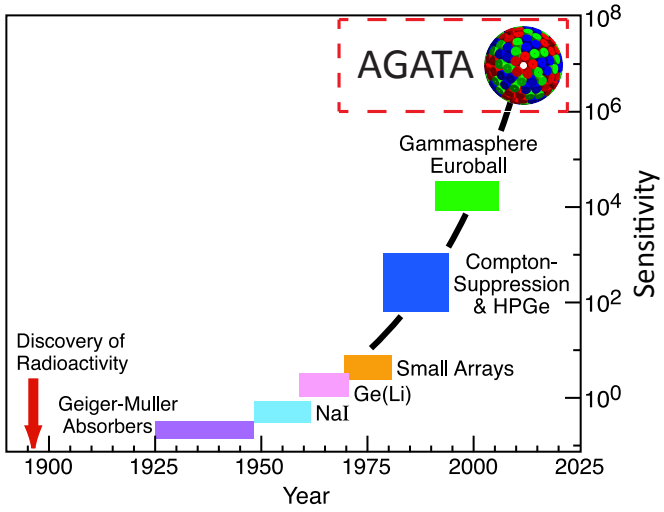

Figure 2.10: Sensitivity of γ arrays across the years - Sensitivity (inverse of the fraction of the weakest channel reaction cross–section that can be appreciated with respect to the total reaction cross–section) of the main HPGe arrays built by different collaborations across the years (figure taken from (69)). The predicted sensitivity of the full AGATA array is also shown.

to sensitivities larger than 10^4, with a gain of over four orders of magnitude with respect to the first Ge(Li) detectors. A major breakthrough in the field of γ–spectroscopy was achieved in the 1980's with the construction of arrays of Compton–shielded large–volume HPGe detectors –GASP (74, 75), EUROGAM (76), EUROBALL (77, 78) and GAMMASPHERE (79, 80).

How can one compare different HPGe arrays for γ–ray spectroscopy? The concept of *resolving power* has been introduced (see, for instance, (81, 82)) as a figure–of–merit that "quantifies" how much do the γ–ray peaks stand out from the background by using multiple coincidences. This quantity can be written as:

$$R = \frac{SE_\gamma}{\Delta E_\gamma}\frac{P}{T} \tag{2.6}$$

thus proportional to the peak–to–total ($\frac{P}{T}$) ratio, to the average separation between two different gamma lines (SE_γ) and inversely proportional to the effective energy resolution (ΔE_γ) which takes both the intrinsic energy resolution and the Doppler broadening due to the finite opening angle of the detector into account. It can be shown that the peak–to–background ratio N_P/N_B depends on the resolving power as

well as on the fold F of the coincidences (81, 82), namely on the number of detectors observed in coincidence:

$$\frac{N_P}{N_B} \propto R^F \tag{2.7}$$

The resolving power was used to compare the performance of different HPGe arrays when used for the detection of closely spaced lines, as it is the case of *superdeformed* bands (83), where the different γ lines are separated by $\approx$ 100 keV. The resolving power ultimately describes how the array can resolve many weakly populated sequences embedded in large and complex backgrounds. Further improvements in the resolving power can be obtained with additional information, for instance the selection of the reaction channel of interest by means of *ancillary* devices, used in coincidence with the HPGe detectors. Examples of such devices used during the Legnaro campaign of the AGATA Demonstrator are the PRISMA (84) magnetic spectrometer or the DANTE (85) and TRACE (86, 87) charged particle detectors.

In principle, an array of germanium detectors should have as large as possible photopeak efficiency, in order to keep the time needed to acquire the required statistics to a minimum. Large photopeak efficiency is best obtained by combining several detectors, each of them subtending a small solid angle. In this way, not only the Doppler broadening effects are kept under control, but also the probability of multiple hits, i.e. two or more photons entering the same crystal at the same time, is minimized. Multiple–hit phenomena can of course be significant when several photons are emitted simultaneously.

The characteristics to be considered to assess the quality of an array of HPGe detectors for high–resolution and high–efficiency in–beam gamma–ray spectroscopy can thus be summarized as follows:

- effective energy resolution;
- full–energy (photopeak) efficiency (ϵ_{ph});
- peak–to–total ratio;
- granularity;
- amount of dead materials;
- time resolution;

- counting–rate capabilities.

With the "conventional" Compton suppression techniques, it was not feasible to reach simultaneously total photopeak efficiencies around $\epsilon_{ph} = 50\%$ and P/T ratios around 50%. These two parameters are considered essential features to pursue the physics program at the future radioactive ion beam facilities (88). An alternative approach, followed since the 1990s (89), involves the construction of a Ge ball around the target position, with the development of techniques (*pulse shape analysis* and *γ–ray tracking*) to "look inside" the germanium crystals and to follow the individual photon scattering.

As in this work the first prototype of an Advanced–Gamma Tracking array has been used, the principles of such an instrument will be now extensively introduced and outlined.

2.2.1 Principles of gamma–ray tracking

It is known that charged particles release their energy in a medium through a continuous process of scattering with the electrons (and atoms) of the material. In this way, a continuous ionization path is generated, which can be directly followed (tracked). On the other hand, in the case of neutral particles (neutrons and gammas) the energy is released in a discrete number of interactions, that can be located at "large" distances one from the other. The aim of the *γ–ray tracking* technique is the reconstruction of the individual γ–ray energies and directions based on the deposited energy and position of all the interaction points of an event seen by the detector(s). For each event, the number of photons, their energies, the incident and scattering directions should be measured, and the events corresponding to incomplete energy release should be discarded. In principle, this could be performed by knowing both the interaction positions with sufficient precision and the details of the interaction mechanisms, as summarized in Fig. 2.11 for the energies of interest for gamma spectroscopy.
Below 100 keV, the photons are mainly detected by photoelectric effect. In this process, the photon is absorbed and the energy is used to ionize an atom in the detector, resulting in a single, isolated interaction in the germanium medium.
In the energy range between 100 keV and 10 MeV the dominant interaction mechanism is Compton scattering, i.e. the elastic collision of a photon with an electron of the

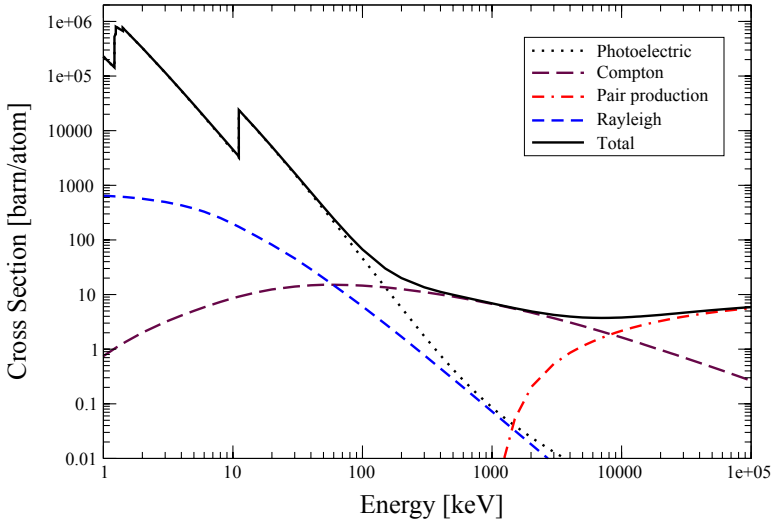

Figure 2.11: Cross sections for gamma interaction in germanium - Cross–section per atom as a function of the γ–ray energy for photons interacting with germanium for the main interaction mechanisms. The Compton scattering is the dominant interaction process in the 100 keV–10 MeV energy range.

absorbing material. In the limit of a free electron at rest, the process can be described analytically –see Eqn. 2.8.

Above 1.022 MeV the γ energy is sufficient for creating an e^-–e^+ pair, with the positron later annihilating and emitting two 511 keV photons in opposite directions.

To clarify the ideas behind the concept of γ–ray tracking, let's consider a photon that is absorbed after two consecutive scatterings, as schematically represented in Fig. 2.12. As said, the energy of the scattered photon in a collision with an electron (assumed to be unbound and at rest) is related to the scattering angle via the Compton formula, Eqn. 2.8 in Fig. 2.12. If the source position is known, a Compton scattering event can be tracked by evaluating the Compton formula for each permutation of the interaction points and by building a χ^2 function (or *figure of merit*) similar to the one shown in Eqn. 2.10.

The relevant equations are summarized on the left–hand side of Fig. 2.12. Basically, our figure of merit function is constructed by comparing two independent evaluations of the scattered photon energies (or, equivalently, of the scattering angles). Recalling that the initial photon energy E_γ is the sum of the individual deposited energies, and assuming a given sequence for the photon scattering, the photon energy after the i^{th}

$$E_{\gamma i} = \frac{E_{\gamma i-1}}{1 + \frac{E_{\gamma i-1}}{m_e c^2}(1 - cos\theta_i)} \quad (2.8)$$

$$e_i = E_{\gamma i-1} - E_{\gamma i}$$

$$cos\theta_{Pos} = \frac{\vec{01}\vec{12}}{|\vec{01}||\vec{12}|} \Rightarrow E_{\gamma'}^{Pos} \quad (2.9)$$

$$\chi^2 \approx \sum_{n=1}^{N-1} w_n \left(\frac{E_{\gamma'} - E_{\gamma'}^{Pos}}{E_\gamma} \right)_n^2 \quad (2.10)$$

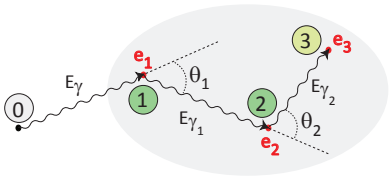

Figure 2.12: Compton scattering - Example of a gamma ray undergoing two Compton scatterings before being photo-absorbed. E_γ is the initial energy of the gamma ray, $E_{\gamma i}$, e_i and θ_i are the energy of the scattered gamma and electron and scattering angle, respectively.

scattering is easily computed as:

$$E_{\gamma_i} = E_\gamma - \sum_{n=1}^{i} e_n \quad (2.11)$$

Since the scattering angles can be computed from the actual point positions (Eqn. 2.9), E_{γ_i} can also be evaluated starting from E_γ and applying the Compton formula (Eqn. 2.8) in a "recursive" way. The approach of determining the scattering angles from the Compton formula (using the partial energy deposition) and comparing these values with the "direct" (geometrical) determination is obviously equivalent.

In practice, one should construct the figure of merit function for all the possible permutations of the interaction points. The "optimal" permutation does not only correspond to the lowest χ^2 , but normally a more stringent condition is required, namely the event is accepted only if the merit of the best permutation is compatible (lower than) with an empirically defined limit. This is not always the case, thus events where no permutation produces an "acceptable" χ^2 are discarded, producing the software equivalent of a Compton suppression.

In (real) cases with more than one gamma ray per event, the straightforward method would consist in the analysis the permutations of all partitions of the measured points,

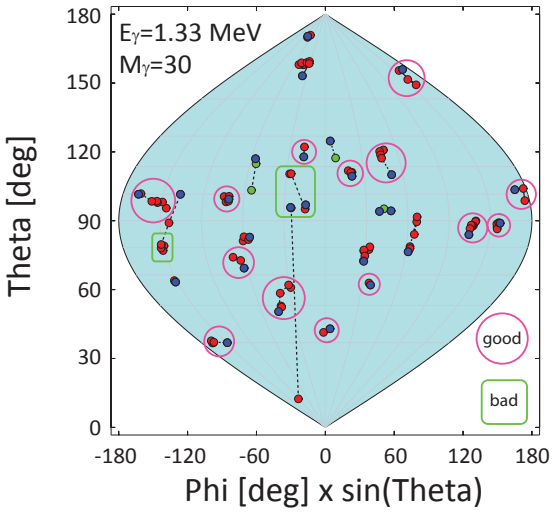

Figure 2.13: Clustering techniques - Theta vs phi×sin(theta) plot for simulated interaction points in an ideal 4π Ge shell (figure taken from (90)).

but this is normally not feasible, due to the huge number of cases to compute[1]. *Clustering* techniques (91) have thus to be adopted to identify smaller sets of points, each of them corresponding to the interaction of a single photon. In fact, since there is a finite absorption length for the photons ($\approx$55 μm for a 10 keV, $\approx$3.5 cm for 1 MeV in germanium) and the Compton scattering reaction cross–section is forward peaked (Klein–Nishina formula), the points generated by a single γ are expected to be localized in a small portion of the total detection volume. The interactions belonging to the same track can be clustered on the basis of both the angular separation (seen from the source) and their mutual linear distance.

As an example, the theta vs phi×sin(theta) plot of simulated interaction points in an ideal 4π Ge shell is presented in Fig. 2.13. Any two points separated by a theta smaller than a reference value are grouped in the same cluster. Once the clusters are identified, the validity of the Compton scattering formula is checked for each of them.

The *forward tracking* method[2] is implemented in the *mgt* tracking code (89, 93), used

[1]The number of ways to partition a set of n objects into k non empty subset is called *Stirling number of the second kind*. For 30 points the total number of partitions is 10^{23}.

[2]Another class of tracking algorithms is based on the *backtracking* method (92): the interaction points within a given deposited energy interval (corresponding to the peaking of the photoelectric absorption probability) are considered as the last interactions of a fully absorbed gamma. The photon scattering is then tracked backwards, up to the known position of the source. As the performance of this method are inferior to the forward tracking algorithms, it was not used in the present work.

in our analysis. The starting point is the identification of a set of clusters, the energy of each of them corresponding to the sum of the energy depositions in the cluster. Then, the three mechanisms of gamma interaction with germanium are tested (considering the appropriate interaction probabilities) and the "good clusters" are selected via a χ^2 test.

There are some fundamental effects limiting the performance of the tracking algorithms:

- the interaction position of the photon is different from the position of the energy deposition (performed by electrons moving in the medium);
- electrons can lose energy via bremsstrahlung, which can result in loss of energy or detection of "spurious" interactions points;
- low–energy gammas towards the end of the track can undergo Rayleigh scattering, resulting in a change of direction, without change of energy;
- electrons in media are not free nor at rest, thus Eqn. 2.8 is approximate and should be corrected to take the momentum profile of the electron into account.

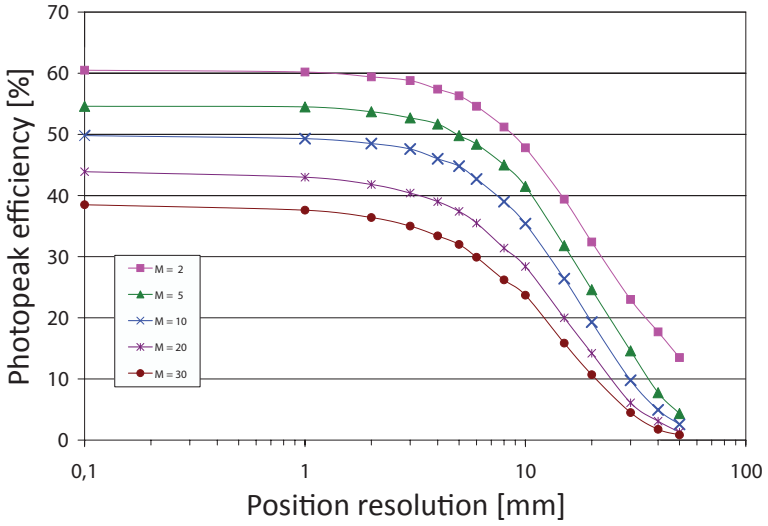

Figure 2.14: Peak efficiency versus position resolution - Photopeak efficiency of an ideal germanium shell for 1.332 MeV (^{60}Co calibration source) photons as a function of the position resolution. Tracking is performed. The different colours and symbols correspond to the performance for different photon multiplicity. (94)

These effects are mostly masked by the limited knowledge of the interaction points achieved at present with actual Ge detectors. Practically, the performance is limited by the uncertainty in the determination of the interaction point, position resolution, energy threshold, energy resolution and the eventual presence of dead materials. The efficiency of a standard Ge shell vs position resolution and gamma multiplicity is plotted in Fig. 2.14, taken from (94), where it is assumed that γ–ray tracking is performed. It is worth noting that, as represented in Fig. 2.14, the tracking algorithms provide "good results" only for a position resolution below ≈ 5 mm. This means that techniques to reach such a position resolution should be developed in order for the γ–ray tracking principle to be applied.

The gamma-ray tracking paradigm is illustrated in the block diagram of Fig. 2.15. The shapes of the electrical signals induced by the interaction of the gamma radiation with the detectors (waveforms or "traces") are digitized (and stored). The interaction points and energy depositions in the detector are reconstructed by means of *pulse shape analysis* techniques (as discussed in the next section). The set of interaction points

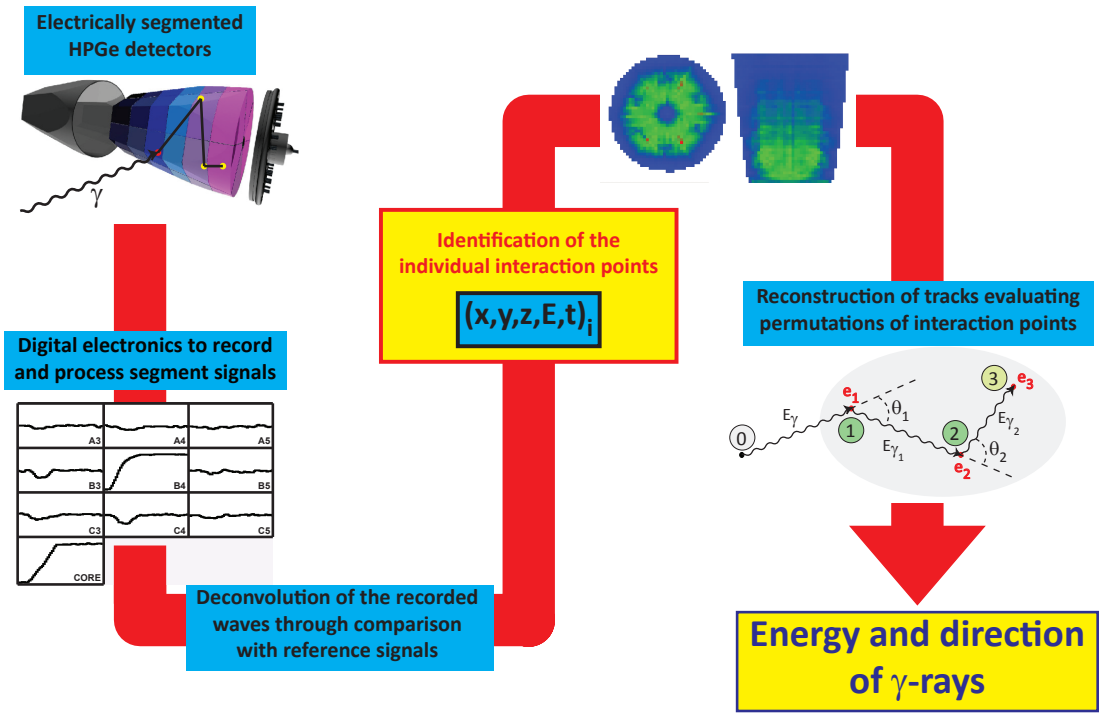

Figure 2.15: The gamma–ray tracking concept - Summary of the fundamental steps in the tracking of gamma rays detected by segmented HPGe detectors.

thus obtained is treated by tracking algorithms and the gamma event is reconstructed.

Already from this brief introduction, we can clearly see that the data analysis and acquisition techniques required by such a system are far more complicated than the ones employed for the "standard" germanium arrays. However complicated it might seem be, the detailed information on the detection process provided by this methodology is the basis for challenging experiments like the subject of this Thesis.

The next sections will describe the technical aspects of the AGATA project.

2.2.2 Pulse shape analysis

The coaxial geometry has always been the choice for HPGe detectors used in the largest part of nuclear spectroscopy studies. A coaxial HPGe detector can be schematically viewed as a charged cylindrical capacitor (with a dielectric medium). The interaction of the gamma radiation in the detector generates electron-hole pairs, that drift to the electrodes (anode and cathode) under the influence of an electric field. What is measured is the current induced at the electrodes by the moving charge carriers. It is well known that the shape of a signal in a true coaxial detector depends on the radius of the interaction (95), as illustrated in Fig. 2.16. Given the cylindrical symmetry of the system, no other information on the position can be extracted. In order to

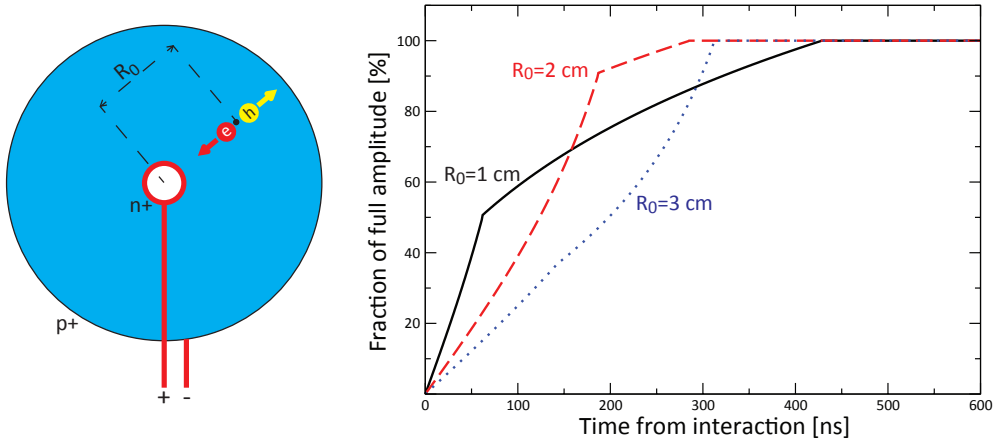

Figure 2.16: Radial dependence of the shape of the signal in a coaxial germanium detector - In a true–coaxial detector the shape of the signals measured at the electrodes depends on the radius at which the interaction takes place. The plotted signal shapes are calculated according to the simplified model reported in (95), assuming constant and homogeneous drift velocity of the charge carriers.

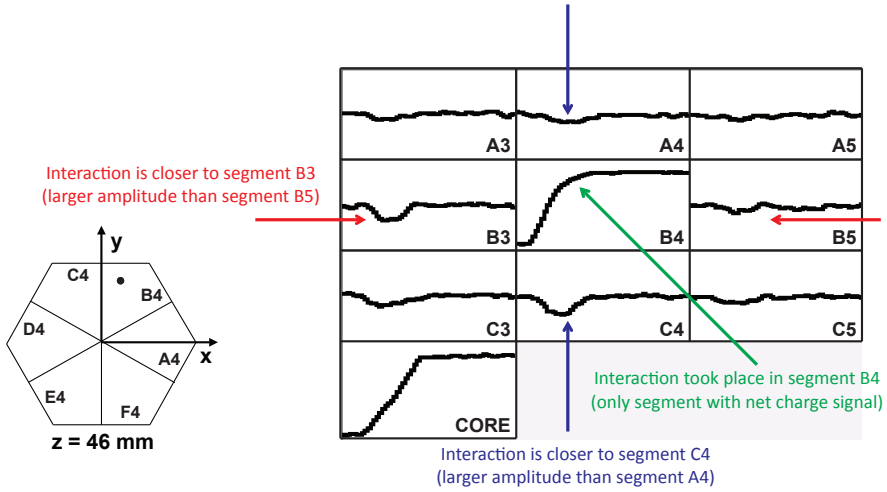

Figure 2.17: Net charge and transient signals - Segment signal shapes following a γ interaction in one segment at 46 mm depth in an AGATA segmented HPGe. The net charge signal identifies the segment where the interaction took place, while the amplitude of the transient signals suggest its position inside the segment.

extract more information, this symmetry has to be broken, for instance by electrically segmenting one of the electrodes. When one of the electrodes is electrically segmented, the motion of the charges within one segment induces signals also in the neighbouring electrodes (Fig. 2.17). Contrary to the segment where the interaction takes place (i.e. where there is a *net* charge release), the total collected charge in the neighbouring electrodes is zero. For this reason, the signals induced in the neighbouring electrodes are known as *transient* signals. The shapes and amplitudes of *net* and *transient* shapes depend also on the angular position of the interaction point, as simplified in Fig. 2.17. The amplitude of the induced transient signals provides a convenient way to locate the interaction with sub–segment precision, but this is not enough to achieve the required position resolution, on the basis of what is expected from Fig. 2.14.

In order to reach a better precision, the full shapes of the observed signals should be compared to a set of reference signals, each of them corresponding to interactions taking place in well–defined locations in the crystal. In principle, the basis of reference signals for a given segmented detector (such as the AGATA detector represented in Fig. 2.20) should be constructed experimentally. This can be done using the so–called *scanning tables* (96, 97). Obtaining scanned bases for all the detectors of an array is far too time–consuming and in practice not feasible, so that techniques to calculate these

reference signals have been developed (98), with parameters adjusted by comparison with measured pulse shapes in "key–locations" in the crystal.

In principle, the signal shape calculations would require the knowledge of the electric field (or of the potential) in the full segmented detector, which is typically a quite complicated problem. In practice, the *Shockley–Ramo theorem* (98, 99) allows for a great simplification. For each sensing electrode, the *weighting field* can be calculated, by solving numerically the Laplace equation with the sensing electrode at fixed potential (V=1 V) and by grounding all the others. Through the Ramo theorem, it can be proved that the charge Q induced on the sensing electrode by a charge q released in a position $\vec{x}$ within the crystal is given by:

$$Q = -qV_w(\vec{x}) \tag{2.12}$$

where V_w is the weighting potential. Once the induced charge is known, the corresponding current can be calculated as a function of position and time. For an AGATA detector, which has a 6×6 outer segmentation, one has 1 Poisson and 37 Laplace (1 anode and 36 cathodes) equations. The calculated basis is usually considered on a space grid of 1 mm and a time grid of 1 ns.

Once the reference signal basis is available, the interaction points of the detected gamma radiation into the germanium detector are obtained by comparison with the recorded waveforms, and this is called *Pulse Shape Analysis (PSA)*. The quality of this procedure strongly determines the performance of the tracking algorithm and depends mainly on two factors, additional to the quality of the signal basis:

1. proper handling of the signals to correct for second order effects due to electronic couplings among the channels

2. performance of the algorithm used to make the comparison

Examples of sources of second order effects due to electronic couplings among the channels. Assuming a "perfectly performing" PSA algorithm, still the experimental waveforms are not at all "ideal", and signal distortions could result in a displacement of the reconstructed interaction point from the actual one. Apart from the electronic noise, that has to be minimized by means of proper groundings of the electronics, some other effects can be observed and taken into account/corrected in the

data preparation to the PSA, as it will be exemplified in the discussion of the analysis part, in Chap. 3.

In any electrically segmented detector the *cross–talk* phenomenon is present. It produces a shift in the reconstructed energies, that is proportional to the *segment* fold of the event, namely to the number of segments firing simultaneously. The origin and calculations for the correction of this effect are extensively described in (98, 100, 101, 102). The cross–talk affects the detector energy resolution since the gain varies depending on the pattern of firing segments. The amplitude of a signal from one segment has therefore to be corrected according to a linear combination of the signal amplitudes of the other segments. Experimentally, two kinds of cross–talk have been observed: a crosstalk which is proportional to the net–charge signal and one which is proportional to its time derivative. Measurements of both kinds of crosstalk are reported in (98).

PSA algorithms. The PSA algorithm compares the measured signals with a reference basis of simulated single interaction signals. This algorithm has to effectively identify the interaction points in the crystal and efficiently process the experimental data in order to obtain these positions and energy depositions from the experimental waveforms in a short time interval. The quality of the PSA algorithm can be tested by comparing the basis signals with experimental data taken in well–defined positions, or, in a less direct but practically faster way, by running in–beam experiments with fast moving nuclei and by checking the Doppler correction capabilities, as shown in (89, 103, 104).

The algorithm used in this work is the *Adaptive Grid–Search* (105). Basically this algorithm compares the measured signals (net and transient signals of the segments) and calculated ones over a fine grid of points in the crystal. It is suited for searching one or two interaction points per segment. Searching one interaction point in a segment is equivalent to consider the energetic barycentre if multiple hits occur. The signal comparison is done evaluating the residue R defined as the sum of the squared difference between measured and calculated signals. The algorithm evaluates R over all the points belonging to the real segment, i.e. working as a full grid search. The smallest R identifies the three dimensional coordinates of the interaction point searched. When two points are searched, the signal in the comparison is a linear combination of signals

for two possible points in the real segment while their amplitudes represent the energy division between the two deposits. This part of data analysis is the bottle–neck of the data processing, taking typically up to 95% of the computing resources. To improve the processing time, the PSA programs used in AGATA implement the so–called Adaptive Grid Search (AGS). This is a simple two–step analysis (105) which starts with an evaluation of the residue R on a coarse grid of points and then proceeds with a search on the fine grid in the surroundings of the coarse–grid minimum to refine the position of the interaction point. With a spacing of 2mm the full fine grid search implies the evaluation of ≈1000 points in a typical AGATA detector segment, resulting in an analysis rate of ≈100 events/s in a standard modern CPU. With a coarse grid spacing of 6 mm, the AGS improves the analysis speed by about one order of magnitude, without significant loss of precision. Due to its relative simplicity and its speed of execution, this algorithm is adopted in the standard PSA procedures of the AGATA collaboration (Sec. 2.2.3) and has been used in (103) to obtain a position resolution of 4 mm for 1.4 MeV energy gammas.

2.2.2.1 Radiation damage from fast neutrons

One of the "by-products" of the PSA consists on the correction of the effects produced by the damage of the crystal structure caused by the interaction of fast neutrons in the germanium medium (106, 107).

It is well known that germanium detectors are sensitive to radiation damage induced by fast neutrons (with energy $E > 1\,\mathrm{MeV}$), which generate charged lattice defects that act as trapping sites for the charge carriers (95). This problem leads to a worsening of the energy resolution, especially in the form of a tail on the left side of the gamma peak in the energy spectrum, as a result of a reduction of the charge collection efficiency (see Fig. 1 in (107) as an example). The main reason for choosing n–type crystals for the detectors used for in-beam γ-ray spectroscopy is that they appear to be less sensitive to neutron damage than p–type ones. This is due to the fact that the defects produced by fast neutrons in the germanium lattice are negatively charged, and therefore do not trap the e^- carriers which, due to the coaxial configuration of the detectors, dominate the signal formation in the positively–biased central electrode, from which the signal is read out. In the case of γ-ray tracking arrays, also the signals induced in the segments of the outer electrode (cathode) are used. They are dominated by the collection of holes

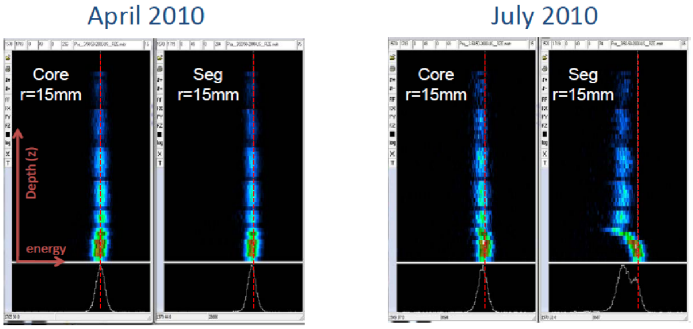

Figure 2.18: n–damage effects in a HPGe operated in position sensitive mode - Depth–energy correlation of the reconstructed interaction points for one of the segmented detectors used in the Legnaro AGATA Demonstrator campaign (see Sec. 2.2.3.1). The figure is taken from (108).

and thus affected by charge trapping effects. Starting with undamaged detectors, for which the energy resolution is better in the segments than in the core, a few weeks of beam time at medium-high counting rate are sufficient to degrade the energy resolution of the segments to values that would normally require annealing of the crystals.

Fortunately, the operation in position–sensitive mode of the germanium crystals offers an interesting way to contrast the trapping effects (106, 107). In fact, for a given level of neutron damage, the fraction of charge carriers lost in the collection process depends mainly on their travel path, the details of which can be easily obtained from the position of the interaction given by the PSA. The principle is represented in Fig. 2.18 taken from (108).

Ideally, the shape of the pulses is also affected by charge trapping but for the practical levels of damage this is not influencing appreciably the pulse shape analysis. The effects of the neutron damage correction based on these principles will be given in Fig. 3.16, of the next Chapter. An improvement of up to 10% in the energy resolution of the segments is obtained.

2.2.3 The AGATA project

Two projects are presently aiming at the construction of arrays of segmented HPGe detectors based on the novel techniques of PSA and γ–ray tracking: AGATA (110, 111) in Europe and GRETA (69) in the US. The innovative performance of such devices will be entirely exploited in gamma spectroscopic studies following reactions induced by

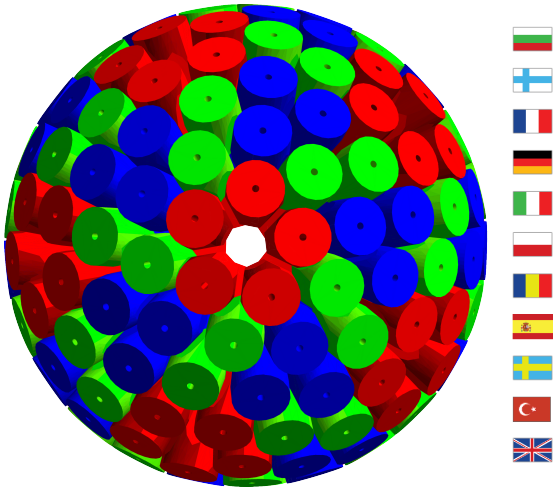

Figure 2.19: AGATA 4π configuration - Geometry of the full AGATA array (109, 110). The flags on the right–hand side represent the different countries presently collaborating to the project.

stable beams as well as radioactive beams. The first phases of these ambitious projects, consisting of a subset of the whole array, have been built and tested in real experiments in order to prove the feasibility of the tracking concept. This Thesis is in fact part of the first experimental campaign with the so–called AGATA Demonstrator (see next Section and (112)).

AGATA (Advanced GAmma–ray Tracking Array) is a collaborative effort of several European countries (represented by the flags in Fig. 2.19) to build a 4π array of segmented HPGe detectors, operated in position–sensitive mode. The full array will consist of 180 n–type 36–fold segmented HPGe detectors, with three slightly different shapes, arranged in 60 AGATA triple clusters (ATC, (113)), i.e. three crystals sharing the same cryostat. The geometry of the array –illustrated in Fig. 2.19– was optimized on the basis of detailed Monte Carlo simulations of the full array (109). The expected performance of the full AGATA array is $\epsilon_{ph} = 43\,\%$, $P/T = 60\%$ for single 1 MeV photons, reducing to $\epsilon_{ph} = 28\,\%$, $P/T = 52\%$ for a cascade of 30 photons of 1 MeV energy. The 6×6 segmentation of the germanium crystals, shown in Fig. 2.20, and in particular the varying thickness of the slices along the detector depth, is the result of detailed electric field calculations aimed at balancing the effective size of the segments.

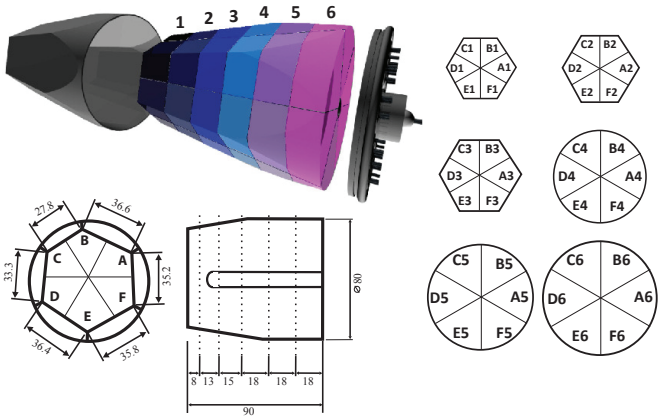

Figure 2.20: Geometry of one AGATA detector - Segmentation of an AGATA HPGe detector. The 36 different segments are identified by the "sector" (column) label and "slice" (ring) number, given in this schematic representation as seen from the front of the detector (adapted from (110)). The size of the front face (bottom left) is shown, as an example, for one of the three different shapes of the AGATA crystals.

As summarized in the diagram of Fig. 2.15, the operation of the detectors in "position sensitive mode" is performed by digitizing the signals from the detector preamplifier and by using PSA algorithms to extract energy and position information. Such an innovative and complex system requires analysis and data acquisition techniques far more sophisticated then those used for "standard" arrays. The architecture of the system and data acquisition (and analysis) is structured in a way that all germanium detectors are followed and treated independently one from another up to the reconstruction of the interaction points inside the individual detector. As for other modern data acquisition systems, the synchronization among different elements is obtained via the distribution of a central clock (GTS, Global Trigger System, Fig. 2.21) and of a time stamp which allow to assemble the data of the detectors fired in a particular event into a global event, containing the information needed to reconstruct (track) the actual γ rays.

It should be observed that the full data processing up to and following the PSA is performed on a dedicated farm of computers. The actual front–end electronics (FEE) for AGATA comprises specially designed charge preamplifiers with differential output, the digitizer modules and the *digital processing electronics*, as schematically represented in Fig. 2.22. The various elements of the front–end electronics are connected via optical

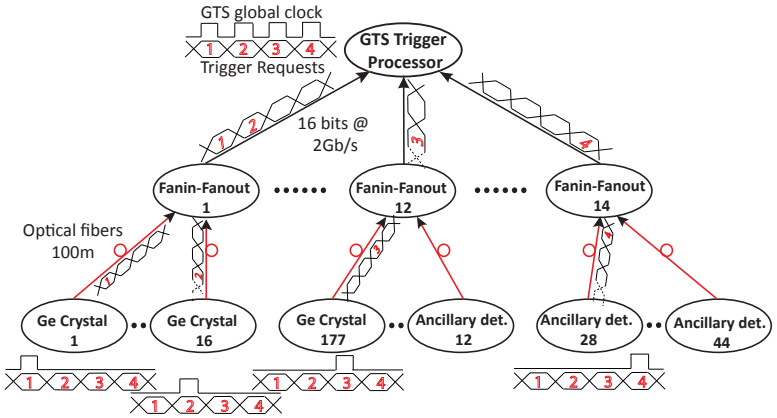

Figure 2.21: GTS tree - Clock distribution via a system of Global Trigger and Synchronization (GTS). The *GTS Trigger Processor* collects the trigger requests and distributes back the validations and rejections to the different GTS *leaves*.

fibers to assure proper data transmission rates and electrical insulation.

The digitizers of AGATA (one for each crystal) perform the signal digital sampling with 100 MHz, 14–bit fADCs and, as mentioned above, they work synchronously by receiving a 100 MHz clock and *timestamp* from the GTS system.

The role of the digital processing electronics is to filter and reduce the amount of data to be sent to the computing farm, by applying digital signal processing algorithms, implemented in FPGAs (Field Programmable Gate Arrays, e.g. (114)). In particular, the energy and time information for each waveform are extracted. The energy is obtained by applying a digital trapezoidal filter (Moving Window Deconvolution, MWD (115)) with rise–time and shaping time based on the characteristics of the detector preamplifiers. The time information is obtained instead with a *leading edge* algorithm. Finally, only the rising part of the pulses is preserved and sent to the computing farm, since it is the part of the signal containing the position information. The digital–processing electronics is realized in the Advanced Telecommunication Computing Architecture (ATCA, e.g. (116)) standard. For each crystal, two carrier boards are used, each of them hosting up to four "daughter" mezzanines. The actual signal processing is performed by the mezzanines, while the carrier cards take care of collecting the results and of making them available to the computing network, with PCI (117) express read–out.

Since the core signal is the sum of the charge released in all the interaction points, this is taken as the trigger for the whole crystal. When this trigger fires, the digital

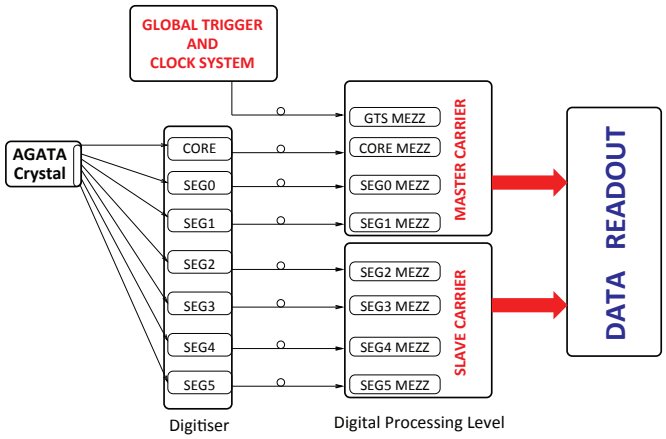

Figure 2.22: AGATA front–end electronics and read–out system - Block diagram for the different components of the FEE for AGATA (adapted from (110)). The digitizers and the digital signal processing boards are based on specific modules (mezzanines), each one able to process up to 6 signals. See text for more details.

signal processing electronics starts the acquisition of the energy and of 100 samples (corresponding to 1 μs of data centered around the risetime of the signal) for all the segments and the two core channels. This data is stored in a local cache memory that can contain up to 20 complete events. In parallel, the time stamp value of the local trigger is sent to a second level trigger board as a request to participate in the generation of a global trigger, that can be used to select a subset of "interesting" events (e.g. with a minimum number of individual Ge crystals or/and other ancillary detectors). If the global trigger condition is satisfied, an event number and a validation signal are sent back to the participating detector(s) to initiate the transmission of the local data (energy and signal samples for the 38 channels plus event number and timestamp, summing up to 9296 bytes for each participating detector) to the DAQ computers where the next data processing stages take place. Trigger requests that do not satisfy the global trigger conditions are sent back to the requesting modules as rejection signals to discard the locally stored data, thus freeing the corresponding memory slots for the next events. For low counting rate experiments, the global trigger can be set in a way that all the local triggers are validated (trigger–less mode, which was the case of the experiment discussed in this thesis).

At $\approx$10 kB/event/detector, a global trigger rate of 1 kHz with an average detector multiplicity of 3 generates 30 MB/s of data entering the computer farm. This data has

to be processed in real time and (at least for the Demonstrator phase) should be stored to disk for off line (re)processing. Clearly, this can only be achieved by a dedicated computing infrastructure with parallel and distributed processing of the specific analysis tasks. The data flow and task management of the AGATA Data Acquisition (DAQ) computers is handled by the NARVAL system (118, 119) as described in the following section.

Organization in chain of *actors*: the NARVAL philosophy

Narval (Nouvelle Acquisition temps-Réel Version 1.2 Avec Linux) (118, 119) is a modular distributed data acquisition system that manages the data flow and the synchronization of the many processes into which the readout, processing and storage of the AGATA data is split. Narval is written in ADA, a strongly–typed object–oriented computing language in which task distribution and process synchronization is provided directly by the compiler. ¿From the user point of view, the AGATA DAQ is seen as a single program with multiple tasks running in parallel on the same or different machines in a transparent mode. Like done in the preprocessing electronics, the individual detectors are processed in parallel and independently from each other up to the point where the data is built into a global event. The analysis of the individual detectors is organized into a pipeline of processes (called *Actors*) which receive the data from the previous stage, make some action on it and pass it to the next stage. While the underlying Narval infrastructure written in ADA manages the flow of data from one stage of the pipeline to the next, the specific data processing is performed by programs written in C++ loaded into the system at startup as shared object libraries. To the C++ programmer, the data processing programs appear as *daughter classes* which inherit from a *mother class* that provides methods to read the data and write it back after having performed the foreseen actions. There are 3 different types of actors:

1. *Producers*, which do not get data from a previous block and therefore lack the read methods;

2. *Filters*, which read data from the Narval flow, process it and write it to the output;

3. *Consumers*, which get data from the Narval flow, process it (typically by writing it to disk files), but do not pass it back to the Narval flow.

In this framework, the local level analysis pipeline of each germanium detector consists of the following actors:

1. Producer (named *CrystalProducer*) that reads the data from the front-end electronics;
2. Filter (named *PreprocessingFilter*) to perform proper calibrations on the energies and on the traces;
3. Filter (called *PSAFilter*) to extract the position of the interaction points from the calibrated data;
4. Filter (named *PostPSAFilter*) to make some final local level processing on the interaction points (e.g. neutron damage corrections);
5. Consumer (named *GenericAFC*) to save the results to disk files.

The global level analysis of the data consists of:

1. a special multi-input Filter (named *EventBuilder*) that gets the data after the local level processing and builds it builds it into a global event;
2. Filter (named *TrackingFilter*) that performs γ-ray tracking and
3. a final Consumer (based on the GenericAFP class) that saves gammas produced by the tracking for the final Physical Analysis.

When the global level analysis is performed in real time (i.e. during the experiment), the EventBuilder receives the data directly from the last filter of the local level processing pipeline. If instead the data is replayed off-line, the Event builder receives the data from a Producer actor which reads it from the data files where it has been saved.

In the end, the power of Narval is the flexibility with which the user can define (via setup files) the *Topology* of the system (i.e. the structure of the individual chains, their number and the computers on which the various actors have to run). It should also be mentioned that this analysis model is available also in a pure C++ environment (although with less flexibility on the distribution of the actors to different computers) via a so-called "Narval emulator" (120), which, indeed, has been very much used to debug the programs and in the off-line replay and analysis of the present experiment.

2.2.3.1 The AGATA Demonstrator at the Legnaro National Laboratories

The γ-ray tracking concept has been implemented for the first time at the Legnaro National Laboratories (121), during the AGATA Demonstrator campaign (86, 112). A critical assumption in the development of the AGATA array is that pulse shape analysis and γ-ray tracking should be performed in real time in order to reduce the data stream to amounts manageable with the present technology. For this reason, it was considered mandatory, while defining the project, to provide a "proof of principle" that this was indeed possible. Therefore, it was decided to build, in the initial phase of the project, a subset of the whole array, known as the AGATA Demonstrator (AD) array, with the goal to provide such a proof of principle. In Fig. 2.23, a picture of the AD array is reported, taken from the reaction chamber point of view. The AGATA Demonstrator Array is an arrangement of five triple clusters of the same kind of the 60 modules which will be used to form the final AGATA array. As reported in details in (109), the performance of the AGATA Demonstrator depends critically on its placement relative to the target position. The full peak efficiency for 1 MeV photons (after tracking) is $\approx$ 3% when the detectors are placed at the "nominal" distance, i.e. the 23.5 cm, radius of the full array. The efficiency reaches $\approx$ 7% when rigidly translating the Demonstrator 10 cm closer to the source position (112). In the same reference, it is shown how the reduction of the distance does not affect significantly neither the P/T ratio ($\approx$ 60%) nor the Doppler correction capabilities.

The AGATA Demonstrator has been installed at the LNL starting in 2009 with the basic infrastructure (one triple cluster and the associated electronics) and reaching the full configuration at the beginning of 2011 (5 ATCs). During this period, after a first part of technical commissioning, where the tracking and PSA capabilities were tested and investigated with standard gamma–ray calibration sources (110) and also in a series of "easy" commissioning experiments (122, 123, 124), experiments with an actual physics goal were performed.

The initial goal of the campaign at LNL was to prove that indeed PSA and γ–ray tracking could be successfully performed in real time. The validation of the γ–ray tracking at LNL occurred on the most demanding conditions achievable at a low-energy stable-beam facility, i.e. velocities of the gamma–emitting products up to $\beta \approx 10\%$ and relatively high intensity beams. Once this was achieved, the AGATA Demonstrator

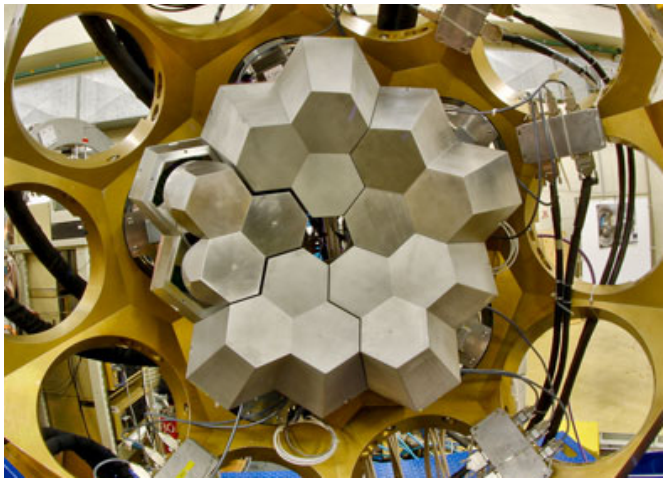

Figure 2.23: The AGATA Demonstrator array at the LNL - Four triple clusters plus one dummy one are seen from the reaction point of view. The picture was taken in April the 9th (inauguration) and, as in our experiment, the Demonstrator was not yet complete.

was mostly used in coupled operation with the large acceptance magnetic spectrometer PRISMA to perform spectroscopic studies of moderately neutron-rich nuclei populated by grazing reactions as multi–nucleon transfer or deep inelastic collisions with the stable beams delivered by the Tandem–ALPI and the PIAVE–ALPI accelerator complex. AGATA was also successfully coupled with a number of other complementary detectors in order to exploit experimental possibilities beyond the aforementioned reactions, namely with direct, Coulomb excitation as well as with fusion-evaporation reactions.

The overview of preliminary results from the first experimental campaign at the LNL is reported in (112), in various conference proceedings (44, 125, 126), LNL Annual reports (127, 128, 129, 130, 131) and journal articles (132, 133, 134). Between 2010 and 2011 roughly 150 days of beam time were devoted to AGATA, performing 19 measurements and 3 in–beam tests. In Fig. 2.24 the summary of the experiments performed in the AD Legnaro campaign is reported, identifying the mass region object of the different studies and the respective physics themes. The stable beam–target combinations available at the LNL allowed for the investigation of the nuclear structure in the n–rich side of the nuclide chart, by coupling the AD array with the PRISMA magnetic spectrometer and the DANTE charged particle detector. Several experiments were dealing with lifetime measurements, mostly with the differential plunger technique. In

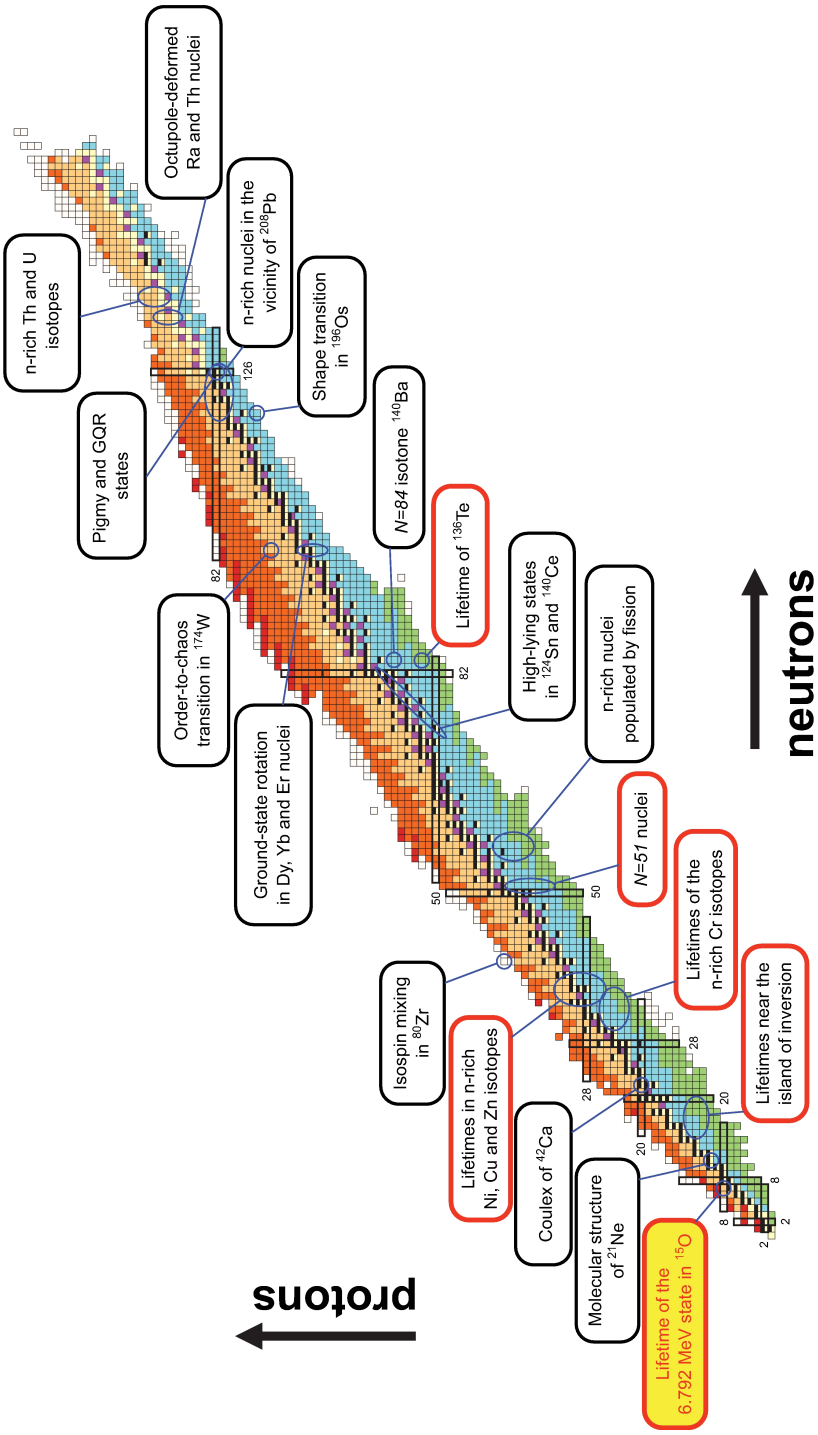

Figure 2.24: AGATA Demonstrator campaign at the LNL - Schematic representation of the N vs Z nuclide chart with the experiments performed in the Legnaro campaign at LNL, using the stable beams provided by the Tandem/PIAVE-ALPI accelerator complex (121).

fact, for these experiments the gain in efficiency and sensitivity with respect to the CLARA–PRISMA campaign was expected to be significant (86).

For the experiment discussed in this Thesis (yellow box in the figure), the Demonstrator consisted of 4 clusters that were placed at the most backward angles with respect to the beam direction, in order to maximise the Doppler shift effects (since, as discussed in the following section, the reaction products were focused along the beam direction).

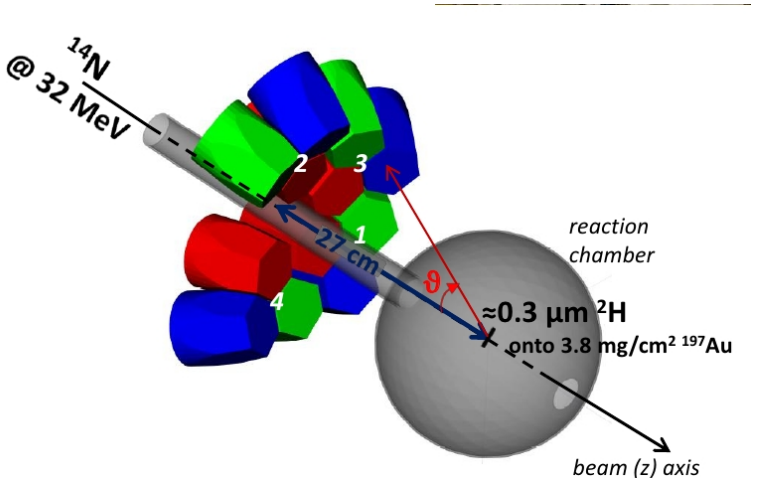

Figure 2.25: Experimental setup - Schematic representation of the reaction and detection setup, see text for the details.

2.3 The experiment for the measurement of the lifetime of the 6.79 MeV state in ^{15}O

¿From now on we will focus on the description of the set–up and data analysis of the experiment for the lifetime measurement of the 6.79 MeV state in ^{15}O (see Fig. 1.7 and yellow box in Fig. 2.24). Several experimental tools were used in order to maximise the Doppler shift and the slowing down effects in the lineshape of the γ–ray peaks (Sec. 2.1.1.2). The reaction and detection setup is sketched in Fig. 2.25. A reaction in inverse kinematics, of the kind used in (36) and discussed in the previous Chapter, was used: excited levels in ^{15}O were populated via the $^{14}\mathrm{N} + {}^{2}\mathrm{H}$ reaction, with the ^{14}N beam delivered by the LNL Tandem XTU (121). The target consisted of a thin deuterium layer (0.4 μm) implanted onto a 4 mg/cm^2 gold substrate, used to slow down

the nuclei produced in the reaction. In such a deuterium layer, the ^{14}N projectile nuclei lose approximately 1.5 MeV in the interactions with the gold atoms. The straggling in the initial reaction position is thus negligible. Moreover, at this energy the electronic stopping power is dominant and the systematic uncertainties due to this process are minimal (64) and this is an important condition for our lineshape analysis.

The main reaction products are the mirror nuclei ^{15}O and ^{15}N, populated in the low–lying excited levels reported in Fig. 2.26 (with reaction Q–values Q(d,n)=5.072 MeV and Q(d,p)=8.608 MeV respectively). These nuclear states decay directly via energetic[1] γ rays ($E_\gamma > 4$ MeV) to the nuclear ground state, resulting in a low (essentially 1)

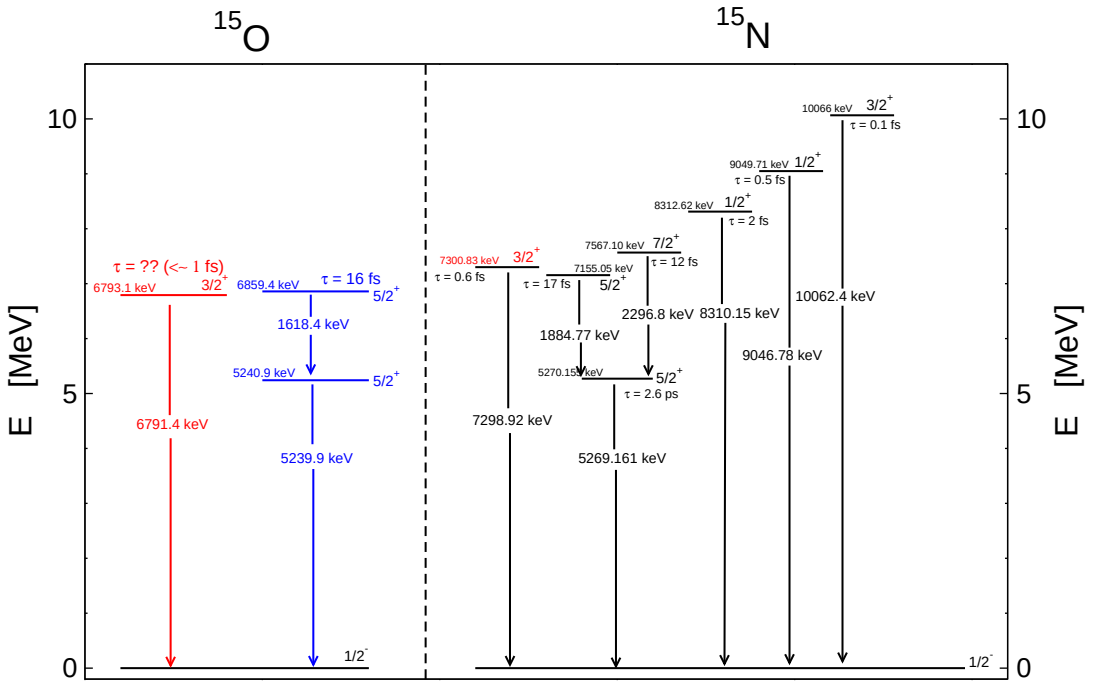

Figure 2.26: Level schemes of ^{15}O and ^{15}N - Level energies and γ–ray transitions for the ^{15}O and ^{15}N nuclei, produced in the reaction process. The level lifetime, where available, is also reported. These are the levels we could reconstruct from the ones listed in (41), and populated in our experiment.

[1]When dealing with heavier nuclei in the region of collectivity, object of most of the recent spectroscopic studies, usually E_γ is $\lesssim$3 MeV.

gamma–ray multiplicity.

The forward focusing of the reaction products was assured by the inverse kinematics. However, at these bombarding energies both fusion–evaporation and nucleon transfer channels are opened, so that (as we will see in the analysis section) the details of the reaction product angular distributions have to be known. Calculations have been used to this purpose (see Sec. 5.1.1.1). The coupling of the detection array to charged–particle or neutron ancillary devices was unfeasible due to the tight forward focusing on one side and the detection efficiency on the other.

The AGATA Demonstrator array was composed of 12 detectors arranged in four ATCs (Fig. 2.25). The detectors were placed at the most backward angles, close to the beam–line (Fig. 2.27), in order to maximise the Doppler effects. The angles covered by the detectors with respect to the beam axis range from $\approx$ 150 to 170^{o}, (see Tab. 3.1). A 2 mm thick lead shield was placed in front of the detectors to reduce the counting rates due to X–rays, see Fig. 2.27. In order to monitor possible gain instabilities, a gamma–ray radioactive source was kept close to the germanium detectors during the whole experiment (see Sec. 3.1.1), providing γ-ray energies close to the energy region of interest. Since γ–ray energies of about 6–8 MeV were expected from the de–excitation of the nuclei produced in the $^{14}\mathrm{N} + ^{2}\mathrm{H}$ reaction, to avoid saturation in case of detection of these high–energy γ-rays, the digitizers of the segments were operated in the 20 MeV full scale range instead of the more common 4 MeV range. This was not a problem for the core signals because the electronics provides by default a 4 and a 20 MeV range. A drawback of using the 20 MeV range is that, due to intrinsic limits of the flash ADCs used by the digitizer, the low–energy parts of the spectra have some degree of non

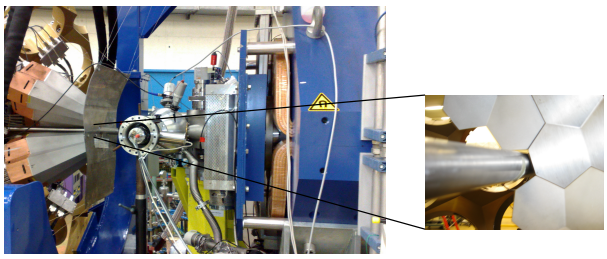

Figure 2.27: AGATA setup for the experiment - Side view of the detection setup used in our experiment. The 4 ATCs were placed at the most backward angles, close to the beam line. A 2 mm thick lead layer was placed in front of the detectors in order to reduce the counting rate due to X–rays.

linearity which must be taken care of by the calibration procedure (see Sec. 3.1.1).

The global trigger for the data acquisition was in *singles* (no multiple gamma coincidences were conditioning the data acquisition so that all trigger requests were validated) with a data storage of 450 Hz, 400 Hz of which due to the radioactive source. During the experiment an amount of approximately 7 TB of data was stored to disk, consisting of a set of waveforms and time–stamps recorded event by event.

While this experiment did not take advantage of the high counting rate capabilities of the AD, it was of interest not only for its physical motivations, but also for the following technical aspects, important to validate the detection technique and analysis under specific conditions:

- high energy gammas (6.792 MeV, 20 MeV dynamical range for the digitizers)
- AGATA Demonstrator (with 4 ATCs) positioned at backward angles (close to the beam line)
- tracking of γ rays with low multiplicity
- test of the capability of AGATA to exploit the Doppler shift effects in a continuous angular distribution
- application of this technique to fs lifetimes
- lifetime analysis in case of two different reaction mechanisms populating the level of interest

2.3.1 The deuterium target

The target has been produced[1] using consecutive deuterium implantations at different energies, between 30 and 100 keV. The range in the gold substrate was 0.45 μm, which corresponds to a deuterium density of 1.04×10^{18} atoms/cm^2. With the assumption of deuterium atoms occupying interstitial rather than substitutional sites within the Au lattice, the density of the target should not differ from that of pure Au. The target profile (Fig. 2.28) has been measured after the experiment at the CN Van der Graaf accelerator at the LNL (136) and the required distribution has been confirmed. The

[1]The target backing preparation has been done at the target laboratory of the Legnaro National Lab. The targets were implanted at the FZ Dresden–Rossendorf facility.

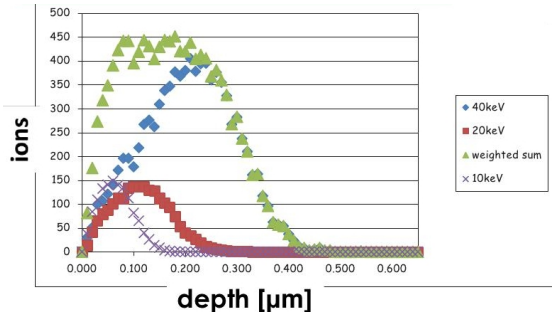

Figure 2.28: Deuterium target implantation profile - Implanted ions concentration as a function of the depth in the implantation layer for different implantation energies. With an implantation energy of 30 keV is possible to reach the saturation with a stoichiometry Au:^{2}H $\approx$ 2.6:1 (135) and a uniform distribution, within 10%, from the surface down to a depth consistent with the 0.15 μm range of the implanted deuterons. Similar target properties are also expected at higher implantation energies.

knowledge of such profile is important and will be used in the Monte Carlo simulation of the lineshapes (see Sec. 5).

3

Replay of the data from the AGATA Demonstrator array

This and the following Chapters will treat in details the construction of the two main components of the line-shape analysis procedure, namely the experimental and the simulated spectra. Both the Monte Carlo simulation structure and the data replay and analysis are important to be discussed, given the complexity and innovation of the system.

The present Chapter will deal with the preliminary data treatment, that will be described in its *replay* and *sorting* stages. The Monte Carlo simulations used for the lineshape analysis will be described in Chap. 4, while the actual lineshape analysis will be the subject of Chap. 5.

3.1 Data replay (processing)

With *data replay* and *processing* we refer to the series of actions performed on the raw waveforms (or *traces*) that lead to the reconstruction of the γ interaction points inside the detector medium and, from them, to the tracked events. During the experiments with the AGATA Demonstrator in Legnaro, this procedure was routinely performed online. While for the operation of the full AGATA array the recording of the full set of raw traces is likely to be technically unfeasible, in the Demonstrator phase also the raw traces have been written to disk, to allow for an offline test of the algorithms. An offline replay has been thus performed in most cases and it turned out that this was

somehow "mandatory" for two main reasons:

- in case of high counting–rate experiments, especially when the merging with an ancillary detector was required (e.g. (130)), a "bottle–neck" at the level of the reconstruction of the global events was observed (due to DAQ–related problems), resulting in a data loss up to ≈30%. This was not, however, our case;
- a careful look to the data allows for a better treatment of signal distortions and energy calibrations. In Fig. 3.1 the improvement in the energy resolution in the offline (red) with respect to the online (black) replay is evident. In the figure, two gamma lines close in energy, produced by the AmBe(Fe) source used during ourthe experiment, are reported. The comparison shows a large improvement in the energy resolution, crucial for the analysis, especially in this particular energy range (around 6–8 MeV).

As described in Sec. 2.2.3, for each detector the event is recorded as a set of 36+2 sampled waveforms, plus the corresponding amplitudes and timestamps. For the 4 triple clusters of the AGATA Demonstrator available during the experiment, an amount of (36(segments)+2(central contacts))×12(detectors)=456 electronic channels had thus to be handled. In order to make the data replay and analysis feasible, automatic procedures have been developed, both for energy calibration purposes and for the preparation of the configuration files for the *actors* used.

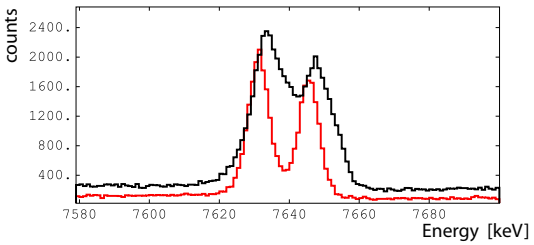

Figure 3.1: Comparison of γ spectra before and after the offline data replay - The 7.631 and 7.645 MeV γ lines from the AmBe(Fe) source in the online (black) and offline (red) spectrum. The improvement in the energy resolution due to the careful offline treatment of the data is evident.

The offline data replay and processing proceeds through a series of actions, listed in a *Topology* of `Narval` *actors*, similarly to the online data processing discussed in Sec. 2.2.3. For the offline data replay we used the `femul` Narval emulator (120). This program implements the same *actor* classes and user–libraries employed in the online system in a "simplified" way (from the point of view of C/C++ programmers –or, at least, "users", that are not familiar with ADA programming language), giving up the possibility to distribute the tasks over different computers, typical of the `Narval` architecture. We could, anyway, parallelize the processing of the individual detectors (see Sec. 3.1.1) by launching several instances of the program over 7 different computers located at the INFN Padova computing centre.

The data are first processed independently for the 12 crystals in order to reconstruct, using PSA techniques, the interaction points (*Local Level Processing*, LLP). Afterwards, this information is merged together (*Global Level Processing*, GLP) and the γ–ray tracking is performed.

The various steps used for the replay of the data from the experiment on the lifetime of the 6.79 MeV state in ^{15}O will be described in the following. We will exemplify the problems and techniques employed in the replay of the data rather than giving a more general overview. For this purpose, we will consider the main tasks of each of the *actors* used at the local (Sec. 3.1.1) and global (Sec. 3.1.2) levels, step by step, referring to the diagrams reported in Fig. 3.3 and 3.17. In these figures, the examples of the corresponding *Topology* files are also reported. After these files are read at program start–up (*initialization*), the *configuration file* for each of the declared *actor* is read (*configuration*) and the data are processed according to the "instructions" (expressed as *key–words* in the configuration file) given to each *actor*. A standard directory structure is assumed for the configuration file storage and input–output of the different stages. This folder organization, together with the content of the configuration files, are built via a `pyton` script (137), for the user to easily change *keywords* and other parameters.

3.1.1 Local Level Processing (LLP)

The different crystals of the AGATA demonstrator used in our experiment are depicted in Fig. 3.2. In the figure, the detectors of ATC 1, 2, 3, 4 are represented schematically (output of the `Geant4` simulation –see Sec 4.2– from the target point of view).

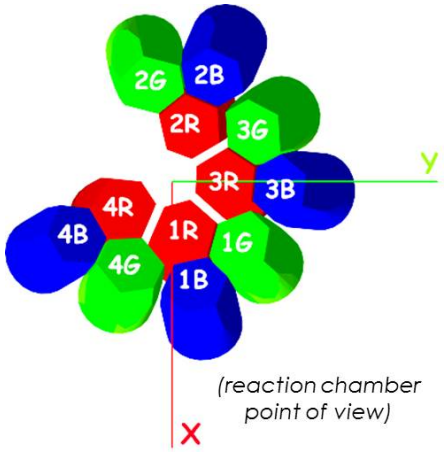

Figure 3.2: Detector numbering - Simulated AGATA Demonstrator detectors, labelled with a number indicating the cluster (1, 2, 3 and 4) and a letter to identify each of them inside the particular cluster (R (red), G (green) and B (blue) – according to the `Geant4` standard colors (138)). The angles of the center of the detectors with respect to the z axis are reported in Tab. 3.1.

crystal name	θ **[degrees]**	$\cos\theta$	ϕ **[degrees]**
1R	168.5	-0.980	32.8
1G	160.0	-0.940	65.3
1B	156.6	-0.918	31.1

Table 3.1: Polar and azimuthal angles of the R,G and B detectors - Polar and azimuthal angles with respect to the beam axis (Fig. 2.25 and z axis in Fig. 3.2) of the 3 of AD detectors (Fig. 3.2) for the experiment. The R, G and B detectors can be grouped in three "rings", according to the different θ angle.

The labelling of the detectors (used during the experiment and in the replay and analysis) is reported in the figure. The "R", "G" and "B" crystals are positioned at θ ≈168°, 160° and 156°, respectively, with respect to the z axis, i.e. to the beam axis. In Tab. 3.1 the polar angles corresponding to the center of the ATC1 detectors are reported, together with the cosine of the polar angle, that enters the Doppler shift relation (Eqn. 2.3).

The *Topology* (chain of `Narval` actors) used for the Local Level Processing (LLP) consists of the sequence (in order) of the following actors: **Crystal Producer**, **Preprocessing Filter**, **PSA Filter** and **Post-PSA Filter**. In the *Topology* file each of these *actors* is listed (*called*) with the syntax reported in the text box in Fig. 3.3. Each

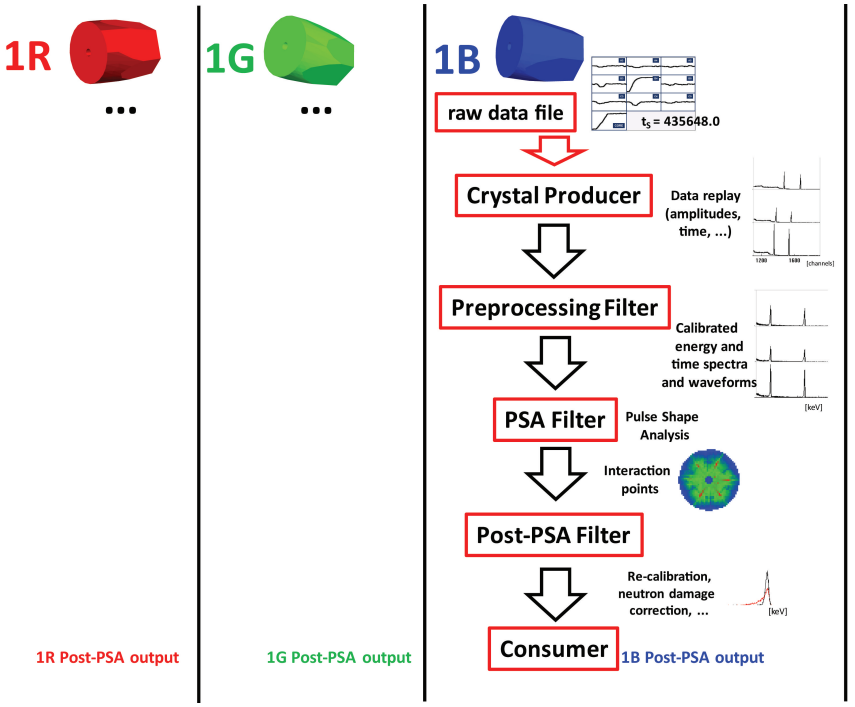


```
Chain 4 1B/
Producer CrystalProducerATCA
Filter PreprocessingFilterPSA
Filter PSAFilterGridSearch
Consumer BasicAFC
```

Figure 3.3: Local Level Processing - Schematic representation of the operations performed at the first level of the data replay, i.e. when the detectors are treated independently, up to the reconstruction of the PSA hits in the detector reference frame. The `Narval` *actors* involved are indicated (for the 1B detector), in the red boxes and the summary of their main tasks is shown to their right (see text for more details). After the *PSA Filter actor* further adjustments on the energies of segments and central contact are performed, and the *chain* is closed with a *Post-PSA Filter actor*. At the bottom right side, an example of the *Topology* file content for the 1B detector is shown. The "Chain" keyword indicates the beginning of a *chain of actors*, "4" in this case, and the directory name "1B" will enter the I/O path at the various stages. Each *actor* is called with the name of the daughter (*actual*) class (see text for details).

actor is indicated with the name of the *mother* class (actor type discussed in 2.2.3) and *daughter* (*actual*) class, that is the derived class, inheriting from the mother its members (variables and methods (139)). Exploiting this feature, which is specific of the object–oriented programming, the daughter classes can be implemented via user–defined libraries (while maintaining the NARVAL structure). For both mother and daughter classes a configuration file should be provided consisting of a sequence of *keywords*, in order to call definite methods of the corresponding class.

In order to understand the various steps of the replay, the different *actors* will be described in their most important parts, showing the most representative spectra[1].

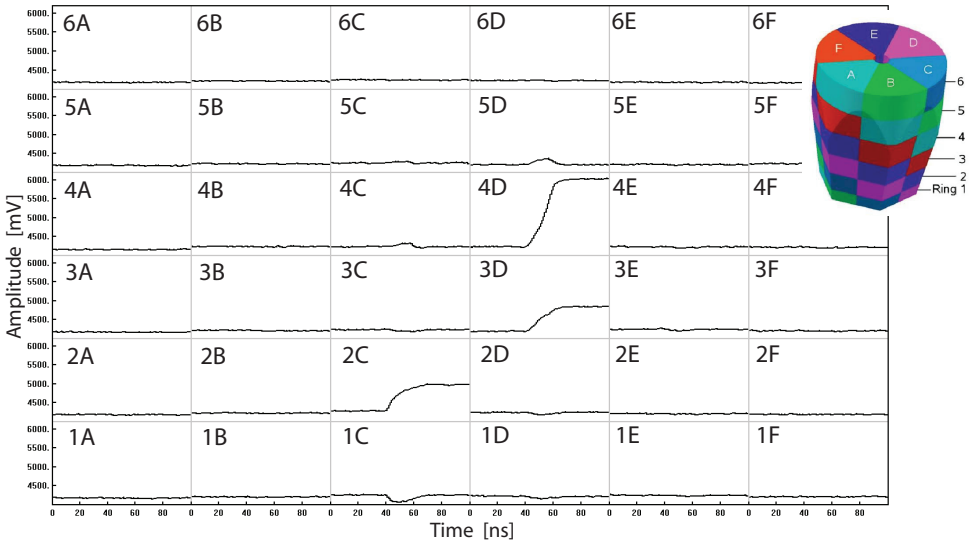

Figure 3.4: Raw waveforms - Raw traces from the segments of one of the used detectors, as decoded by the *CrystalProducer actor*. The mapping of the electronics channels to the physical ones (reported in the figure with reference to the schematic representation of the segmented HPGe in the top right part) is given in the CrystalProducerATCA configuration file. The waveforms reported in this figure refer to the interaction of a ≈1 MeV γ with the net charge released in the 2C, 3D and 4D segments, and transient signals in the neighbouring ones.

[1]While the data are flowing through the different analysis steps, some files are written out, containing spectrum libraries/matrices where the histograms and correlations of the various parameters

Crystal Producer

The first action that has to be performed on the raw data is the decoding of the input channels, i.e. the mapping of the mezzanine read–out channels (see Sec. 2.2.3) with the physical segments/cores. The data format at this level, as well as the elements of the front–end electronics, could vary on the basis of the choice of the architecture and software of the electronics. In view of possible changes in these elements (to be decided on the basis of the outcome of the Demonstrator phase), the structure of `Narval` (and of the `Narval` emulator) allows for a change in the *actual class* used for the mapping of the read–out channels, while maintaining the rest of the structure of the *Topology*. In our case (as for the rest of the LNL Demonstrator campaign and the first experiments recently performed at GSI), the *CrystalProducerATCA actual* class was used. An example of decoded waveforms for the segments of one of the detector is reported in Fig. 3.4. The number of traces to be written to disk and their length

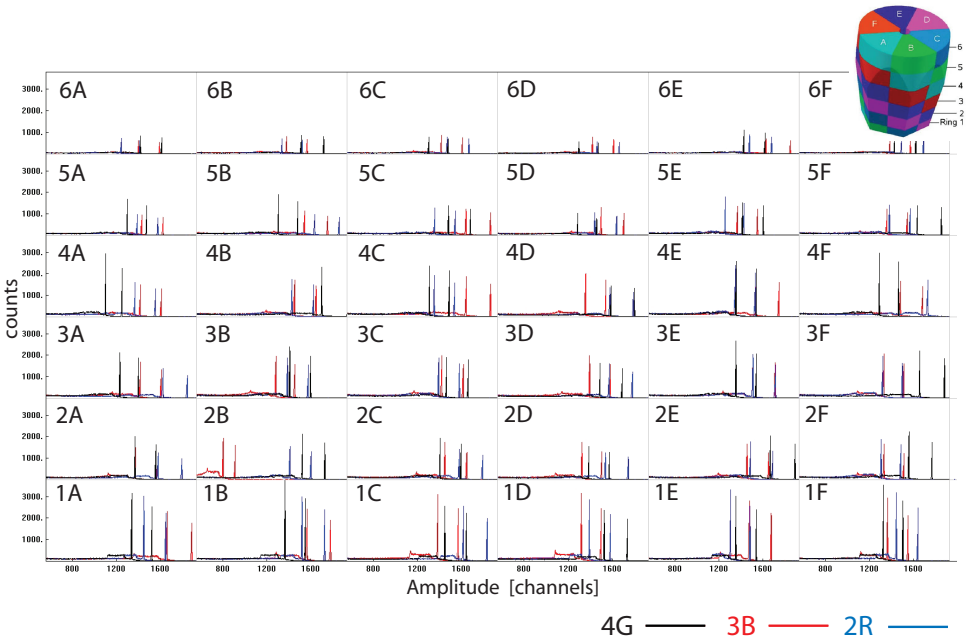

Figure 3.5: Producer amplitudes - *Producer* spectra for the segments of three detectors (4G, 3B, 2R) shown with the `TkT` spectrum viewer (140).

are shown. These spectra (and matrices) are useful for the monitoring of the operation of the various actors on the data flow (calibrations, time alignment, etc.) also during the online processing.

(100 samples in the case of the figure) are given by the user in the *CrystalProducer* configuration file. In Fig. 3.5, the histograms of the amplitudes of the segments of three detectors are shown for a measurement with the ^{60}Co radioactive source. The source was placed in proximity of the reaction chamber and we can notice a reduction of more than a factor of three in the counting statistics between the front ("slice" 1, Fig. 3.5) and the back ("slice" 6) segments. It should be recalled that the absorption length for γ rays of about 1 MeV energy in germanium is ≈ 3.5 cm, less than half the longitudinal size of the crystal (see Fig. 2.20), and this explains the observed drop in count rate. The spectra written to disk at the *Producer* level, when obtained by a radioactive γ source, are the ones used to extract the energy calibration coefficients for the segment and the central contact spectra.

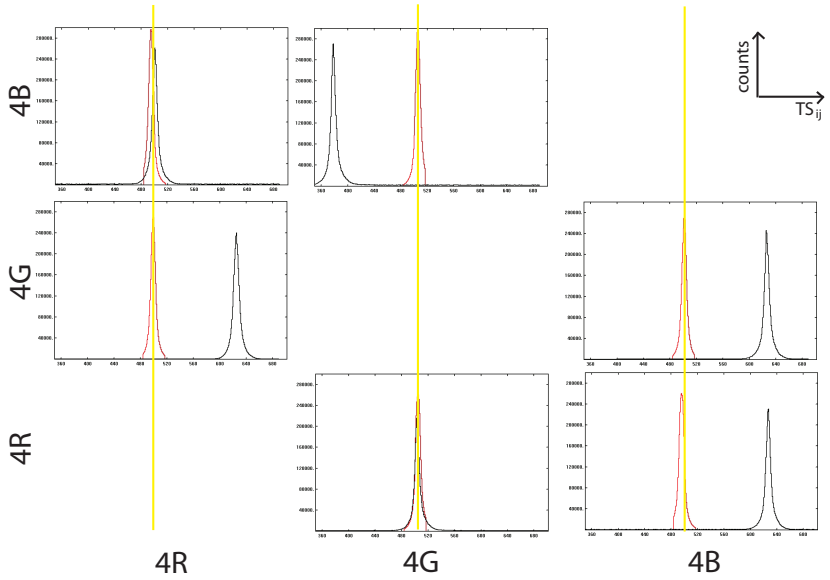

Figure 3.6: Timestamp differences - Timestamp differences between three of the detectors (inside the same cluster, ATC 4), TS_{ij}=timestamp$_j$-timestamp$_i$+offset, were i, j are the detectors indicated at the side (e.g. the spectra on the top left–hand side are the timestamp differences between the 4R and 4G detectors). From the spectra in black (saved to disk during the online processing) one can deduce a lag of 128 samples (1.28 μs) in the timestamps delivered for the 4R and 4B crystals (see text). This shift is corrected by modifying the timestamp at the level of the *CrystalProducer* by the proper amount. The effect of the correction is evident in the red spectra. The yellow vertical line is given as a reference for the position of the timestamp coincidence peak (channel 500).

In the *CrystalProducer* configuration file, an identification number is attributed to the processed crystal, that will be used in the next steps (rotation in the global reference frame, attribution of the ADL basis for PSA, etc.).

At the level of this actor, the value of the timestamp read for each event in a given detector can be corrected, i.e. shifted by a fixed amount (in tens of ns). This correction was introduced when the replay of our experiment started, because a mismatch in the delivered timestamps was noticed. The timestamp values for certain detectors were systematically differing by a fixed amount of samples (in our case, 128) from the others. This was noticed from the histograms of the timestamp differences between different detectors (analogous of the "standard" gamma–gamma coincidences time spectra but with the time measured in timestamp units, i.e. 10 ns units), reported as an example in Fig. 3.6 for the crystals composing ATC 4. The spectra reported in black are the ones obtained during the online processing of a measurement run. From such spectra we can infer a "shift" of 128 samples (1.28 μs) in the timestamps delivered for the 4R and 4B detectors. This effect –present in the second half of the experiment– has been attributed to a problem in the reboot of the FEE, still not fixed at this early stage of the campaign. This asynchrony in the clock delivery can be, anyway, properly corrected at the level of the *CrystalProducer*. The effect of the correction is evident in the red spectra[1].

Preprocessing Filter

After the very preliminary operations on the raw data described in the previous paragraph, data have to be properly prepared for the PSA, in the so–called *preprocessing* stage. As represented in Fig. 3.3, this task is fulfilled by the *PreprocessingFilter*. This part has to be sometimes considered even more crucial than the performance of the particular algorithm used for the PSA (141). What does the PSA algorithm "believe" about the measured signals it compares with the reference basis?

1. the waveforms amplitudes are given in keV, so that the raw ones have to be calibrated (as one usually does for a detector channel involved in a measurement);

[1] These spectra, with respect to the black ones in the same figure, are gated by a coincidence condition for the timestamps, set at the *EventBuilder* level (Sec. 3.1.2). Indeed, this spectra are written out at the Global level, when the information of the different detectors is merged.

2. all the segments in the considered detector are properly working, so that the algorithm searches for a net–charge release and the corresponding transients;

3. the traces corresponding to the different segments are properly aligned, since the PSA algorithm assumes the same "starting time" for all of them.

Energy calibration of the segment and central contact channels. ¿From the amplitude spectra, of the kind shown in Fig. 3.5, the calibration coefficients (deduced with standard calibration sources) are obtained, relying on automatic procedures for peak search and fit (142). Knowing the rise–time and shaping–time of the trapezoidal filter used to process the digital signal, the calibration for the amplitude of the waveforms is determined. This information is provided in the configuration file for the actual class (*PreprocessingFilterPSA*), where a single coefficient (the slope) is given for the energy calibrations of segment and core signals. A first set of these values, for all the detectors, is obtained from the analysis of the ^{60}Co calibration source data. The calibration source data, in case of segmented HPGe detectors, are obtained with longer measurements than with traditional detectors, in order to have enough statistics in the back segments. The preliminary set of linear calibration coefficients from the ^{60}Co run resulted in unsatisfactory peak positions at the higher energies of interest in our analysis (6–8 MeV). The γ rays produced by neutron–capture on Ni, Al and Fe when using an AmBe neutron source ($t_{1/2} \approx 430$ y, activity $\approx$3 Ci) were used in order to verify and, if needed, correct the calibration coefficients over a wider energy range. The AmBe source emits neutrons with an energy spectrum ranging between 2 and 10 MeV (143), produced by the reactions of the α particles emitted by the ^{241}Am nuclei on beryllium. The source was put inside a paraffin (carbon and hydrogen) container (represented in Fig. 3.14, top right hand–side). A one–week long calibration run was performed before our experiment (July 2010), using the gamma rays produced by n–capture reactions on nickel (in the form of a thin disk layer placed above the source). The spectrum recorded by the central contact of one of the detectors is presented in Fig. 3.7. The main gamma lines are indicated in the figure, with the adopted energies (41). Even using γ–ray sources with many calibration lines, the segment channels cannot be properly calibrated and the effects of non linearity persist. This is evident in the left panel of Fig. 3.8, where the (calibrated) spectrum for the 1.3 MeV line in ^{60}Co of the central

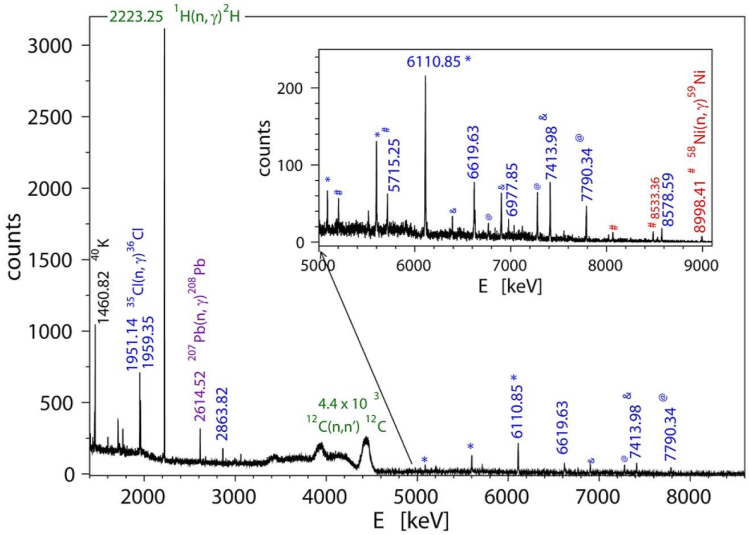

Figure 3.7: AmBe(Ni) gamma source spectrum - Gamma rays measured in the central contact of one of the used detectors (1B) from the capture of the neutrons produced by the AmBe source on Ni. A calibration run of about one week duration was analysed for the determination of the calibration coefficients for the segment and central contact channels of all the detectors.

contact of one of the detectors is compared with the spectrum for the sum of the energy depositions within the segments of the same crystal. While such deviations in the energies are not meaningful at the level of the PSA, they might compromise the output from tracking, since the sum of the energy released in the segments is used for the energy of the reconstructed event. To get rid of this problem, the sum of the energy releases in the segments is "forced" to be equal to the energy read out in the core, in the *Post-PSAFilter*, as discussed in the corresponding paragraph.

The cross–talk correction. Another effect that has to be considered in order to properly reconstruct the amplitudes recorded in the segments is the *cross-talk* between segments, introduced in Sec. 2.2.2. As mentioned there, one observes a deficit in the sum energy of the segments when the event is involving more than one segment, i.e. segment multiplicity $n_S > 1$.

¿From the ^{60}Co data an automatic procedure can be implemented to obtain the cross–talk matrix coefficients, by sorting the energies according to the segment multiplicity and exploiting the 1.17, 1.32 MeV ^{60}Co lines.

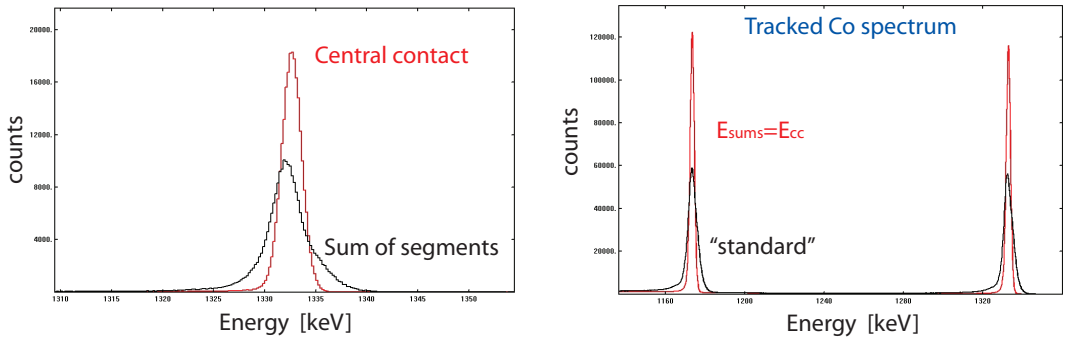

Figure 3.8: Central contact spectrum vs sum of segment energies - On the left–hand side: comparison of the spectra of the 1.3 MeV line from ^{60}Co corresponding to the central contact (red) and to the sum of the energies deposited in the segments (black). The worsening of the energy resolution in this spectrum with respect to the other one is due to non–linearities in the calibration of the segments. On the right–hand side: cobalt source peaks in the tracked spectrum, obtained with the standard procedure (black), i.e. considering the energy of the event as the sum of the ones released in the fired segments, and after forcing the sum of the energy released in the segments to the one recorded in the core (red).

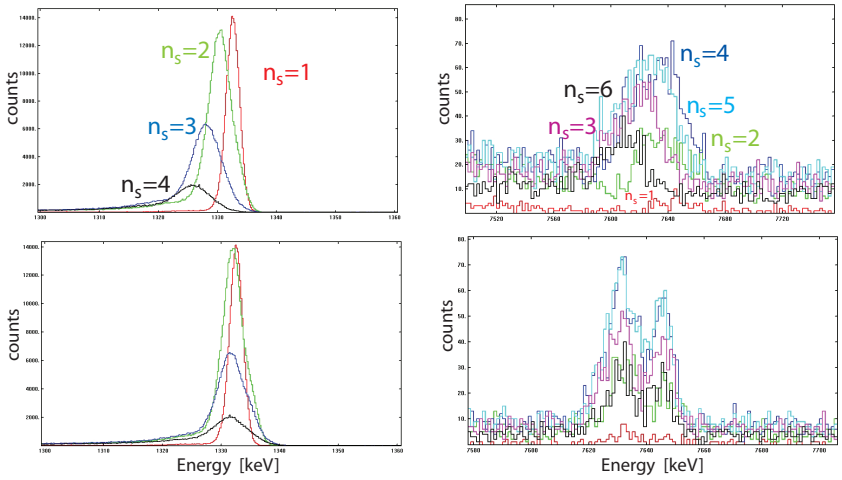

Figure 3.9: Segments cross–talk correction - Energy spectra sorted according to the segment multiplicity (n_S), of the 1.3 MeV line in ^{60}Co (right–hand side) and of the 6.73 and 6.74 MeV (left–hand side) γ rays from the AmBe(Fe) source. The spectra of the second row are corrected for the cross–talk.

In Fig. 3.9 left panel, the spectra of the 1.3 MeV gamma line obtained by summing up the segment energies according to a given multiplicity n_S are reported. As n_S increases, the peak centroid shifts to lower energies. In the left lower panel the same peaks are reported after the correction. In the right side of the figure similar spectra for the 7631, 7645 keV doublet are shown. Before the cross–talk correction the two γ lines can be hardly distinguished. After the correction, the peaks are well resolved.

¿From Fig. 3.9 we can also notice that while segment multiplicity 1 dominates for gamma rays of about 1 MeV, up to 5–6 segments are likely to fire simultaneously for $\approx$ 7 MeV gamma rays, indicating that a proper cross–talk correction is essential when detecting such high–energy photons.

Time alignment of the waveforms. The traces corresponding to the different segments can be aligned in time to the core trace with the proper coefficients given in the *PreprocessingFilterPSA.conf* file. This improves the time resolution in the coincidences and the PSA performance. In Fig. 3.10 the time difference of the segments with respect to the time of the core is reported for two different detectors, before (left hand side) and after the correction (right hand side). In this way, not only the waveforms are aligned "inside" the detector, but also among different detectors. Such shift coefficients are obtained from analogous spectra when triggering with the core alone. The core signals can be aligned as well based on the "time–zero" histogram as found by the PSA (next filter).

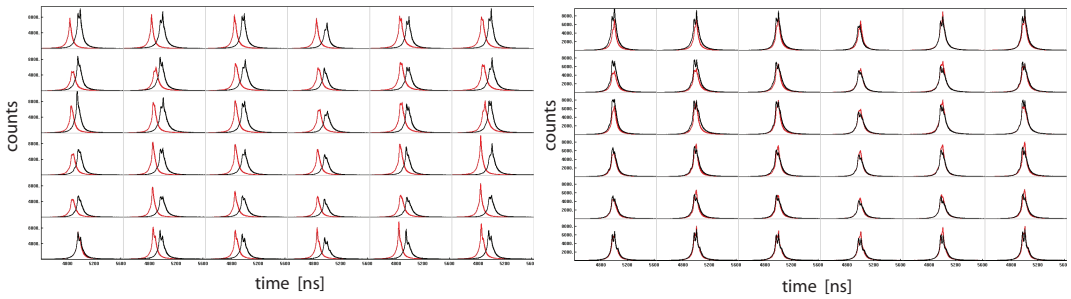

Figure 3.10: Alignment of the time of the waveforms - Time of the segments relative to the one of the core for two different detectors (spectra in red and black), before (left–hand side) and after (right–hand side) the time recalibration.

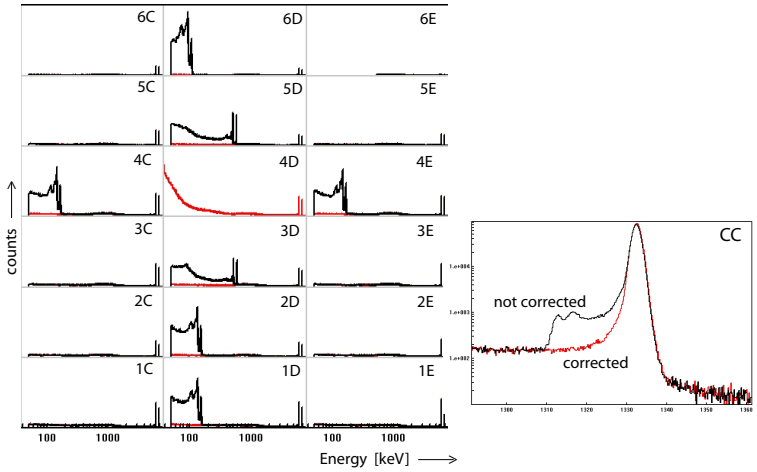

Figure 3.11: Correction for a broken segment - Segment energy spectra of the ^{60}Co source for a detector with the segment 4D (same notation as Fig. 3.5) not present. The energy axis is in logarithmic scale in order to enhance the satellite peak in the first channels (see text). The spectrum of the central contact is also shown for the 1.3 MeV peak, before (black spectrum) and after (red) the correction.

Since in the PSA all the waveforms are assumed to "begin" at the same time, any time misalignments tend to translate into a wrong reconstruction of the interaction points: slower signals, if the experimental waveform is delayed with respect to the basis one or faster signals viceversa, resulting, in case of systematic shifts, in a concentration of points in the corresponding electric field regions.

Correction for a gain–unstable/broken segment. In case the preamplifier of one of the segments is not working down to the FET level, so that the charge is not properly collected, the corresponding signal is totally missing or extremely noisy and *satellite* peaks appear in the energy spectra of the neighboring segments, as illustrated by the black spectra in Fig. 3.11. These peaks correspond to events in which the net–charge signal is absent while the transient signals are present, producing a "step–like" left tail in the central contact spectrum, displayed as the black peak in Fig. 3.11 right side.

¿From the analysis of ^{60}Co source data, a correction to the cross–talk matrix elements can be done in order to recover the signal of the broken segment, considering that the sum of the energies released in the segments should be equal to the one observed in

the core. The result of the correction is reported as the red spectra in the figure. The satellite peaks disappear, as well as the step–like tail in the central contact spectrum.

Similarly one can correct for segments presenting gain instabilities. Such malfunctioning segments lead to the occurrence of multiple peaks in the segment energy spectrum or in a broad peak.

PSA Filter

The PSA has been performed on the preprocessed data using the Adaptive Grid Search algorithm (as *actual class*) –see Sec. 2.2.2. Only one interaction point per segment has been considered in our data analysis. It is clear that this is a rather strong assumption because, given the size of the segments and the γ-ray energies of interest, the probability of multiple interactions in one segment is not negligible. However, the PSA algorithms are not yet "smart" enough to treat multiple interactions in a reliable way and it is preferable to get a result which is the barycenter of the interactions rather than badly positioned multiple points. Exploiting all the processors of the available computing farm, the event rate processed by the PSA was of about 250 ev/s. In Fig. 3.12 two examples are shown where experimental and calculated waveforms are compared. The bases used for the PSA of our data were simulated with the ADL software (144).

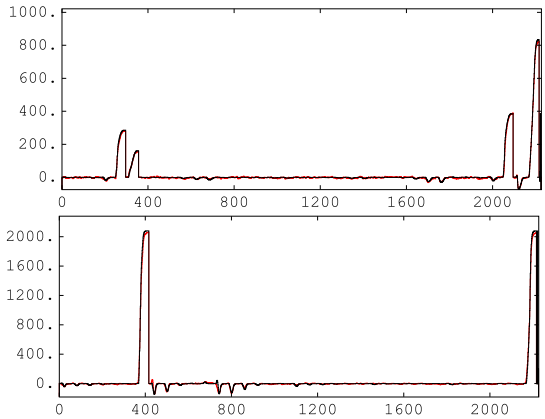

Figure 3.12: PSA traces - Examples of comparison between experimental and calculated traces.

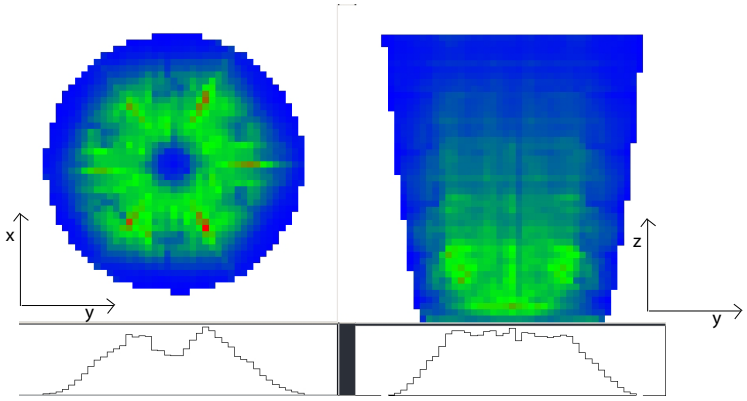

Figure 3.13: Interaction point distributions - XY and YZ projection matrices of the PSA interaction points for the 4R detector. The concentration of points is larger close to the front of the detector.

The distribution of the obtained interaction points (in the detector reference frame) for one of the detectors is reported in Fig.3.13.

Post–PSA Filter

The *Post–PSA Filter* actor is responsible for a series of actions that can be (optionally) done on the PSA hits. At this point, the calibration coefficients for the central contact signals can be refined, by using, as in the case of the present set of data, the stopped peaks provided by the AmBe(Fe) source. The Ni(n,γ) source previously used was replaced with a Fe(n,γ) source, since the former produces γ peaks overlapping with the one of interest between 6 and 7 MeV photon energy. An example of the AmBe(Fe) γ spectrum for the central contact of one of the detectors is shown in Fig. 3.14. The paraffin support for the neutron source is also sketched in the figure. The scaling factors for the calibration coefficients for the central contacts are reported in Fig. 3.15 as a function of the run number (2–3 h run duration has to be considered).

At the level of the *Post–PSAFilter actor* one can force the sum of the energies of the segments fired in an event to the value recorded in the central contact, thus avoiding the effects of non linearities or not proper functioning of some of the segments. In

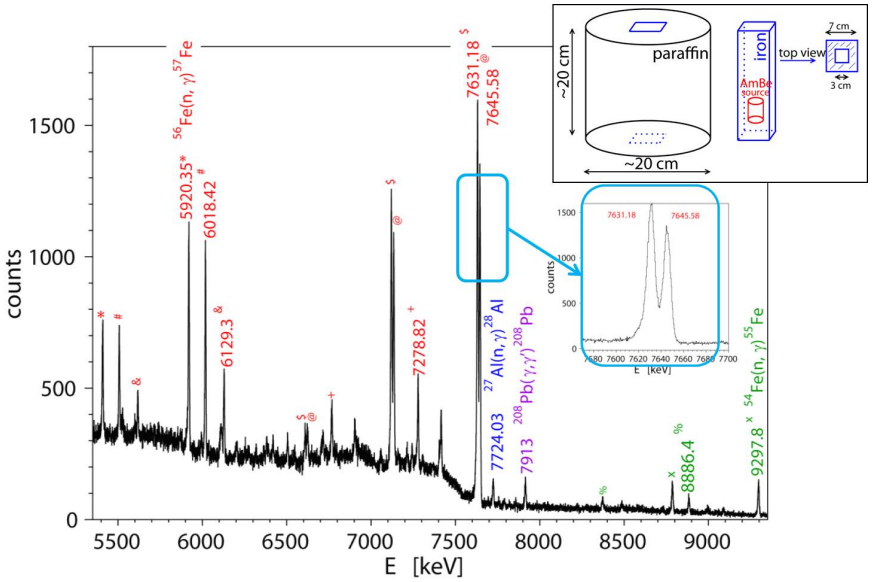

Figure 3.14: AmBe(Fe) source spectrum - Spectrum of the central contact of one of the AGATA Demonstrator crystals corresponding to the AmBe(Fe) source. This was kept while beam–on–target for the monitor of the gain instabilities and thus used to refine the energy calibration coefficients.

Fig. 3.8 right panel, the tracked spectrum (for the 4^{th} ATC) corresponding to the ^{60}Co source obtained with and without this condition is displayed. The advantages in the tracking performance are evident.

At this level, the file with the calibration coefficients of the neutron damage is also given.

The n-damage correction. The correction for the effects of the neutron damage in the detection of the γ rays of interest has been performed following the theoretical approach described in (106, 107), as discussed in Sec. 2.2.2.1. The aim was to obtain a set of calibration coefficients, for all the detector channels, to correct for the electron and hole trapping. This is performed by building a "grid" of such coefficients and applying them to the PSA hits, determining the set that minimizes the FWHM and the left tail of the peaks in the spectra.

In Fig. 3.16 the effect of the correction is shown in the spectra corresponding to one of the detectors. This correction is more evident in the segments, but it is also done for the central contact, and it is thus important also when the energy is forced to the

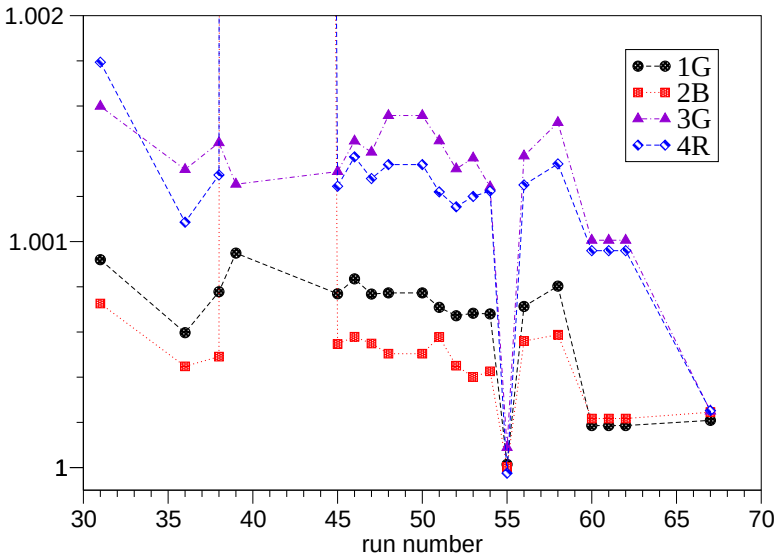

Figure 3.15: Scaling factors for the central–contacts - Scaling factors for the energy calibrations of the central contact that has been applied at the *PostPSA-Filter* level in the replay of the data recorded in different runs.

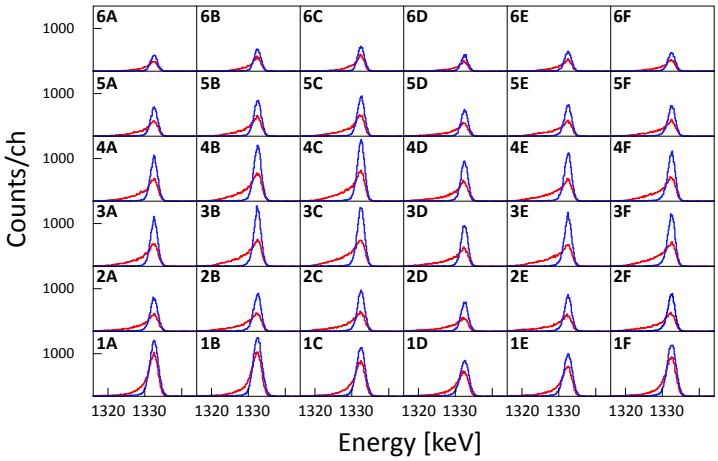

Figure 3.16: Correction for n–damage - Spectra of the 1.3 MeV of ^{60}Co for the segments of the 3R detector before (red) and after (blue) the calibration of the n-damage effects. The overall resolution of the segments and peak symmetry improve $\approx$4% and $\approx$40%, respectively.

value measured in the core, as is the case of the present data.

3.1.2 Global Level Processing (GLP)

As illustrated in Fig. 3.3, the output of the PSA processing is written to disk by a proper Consumer. The files can be read and further processed using a global level *Topology*. The most important `Narval` actors at the Global level are the **Event Builder** and the **Tracking Filter**. The general idea of the GLP is schematically represented in Fig. 3.17. The part of the *Topology* file to which it corresponds is indicated in the text box in the figure.

For each detector, the PSA hits obtained from the the LLP are read via a `Basic Agata Format Producer` and "dispatched" to the Event Builder. In case an ancillary detector is present, this is processed "locally" in an independent *Chain* and the output is dispatched to an *EventMerger* together with the one of the *EventBuilder* (141).

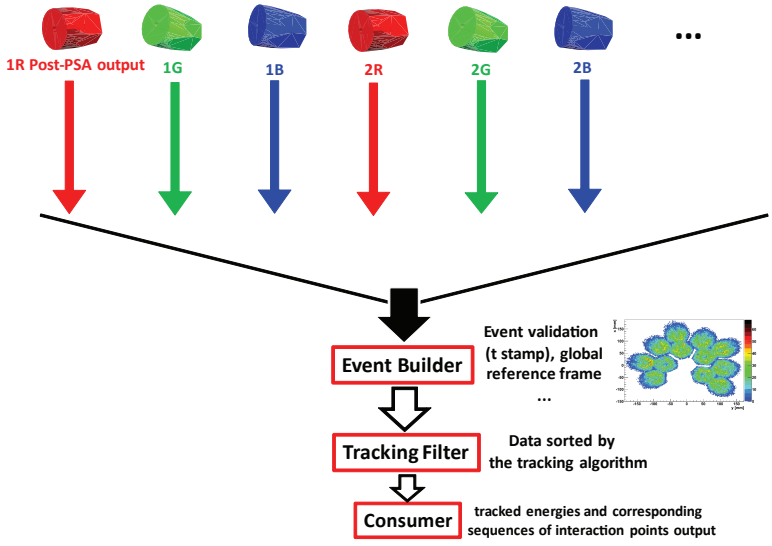


```
Chain 2 1R/
Producer BasicAFP
Dispatcher EventBuilder

[...]
Chain 3 Global/
Builder EventBuilder
Filter TrackingFilterMGT
Consumer None
```

Figure 3.17: Global Level Processing - Schematic representation of the steps followed in the GLP. The PSA outputs of the different detectors are merged together and the events are built on the basis of the timestamp. Part of the used *Topology* file is reported in the text box.

Event Builder

The *Builder* actors accept multiple inputs, for which the input keywords are indicated in the configuration file (according to the Agata Data Format, ADF (145)) as well as the output one.

Before passing to the tracking stage, the data are selected by this actor according to the timestamps. The events can thus be selected on the basis of the crystal fold (1 in the present analysis) and a window on the timestamp differences can be set, as illustrated in Fig. 3.18 for our data. The selection of the events "close" in timestamp not only improves an eventual coincidence analysis, but also improves the tracking performance, due to the elimination of uncorrelated events.

Tracking Filter

The *Tracking Filter* actor calls the actual tracking procedure (MGT –used in this work– or OFT). The performance of γ-ray tracking depends on knowing the position of the source. In our case the AGATA Demonstrator was translated by 54 mm away from the target position with respect to the nominal position, in order to assure the detection of γ–rays at the most possible forward angles compatible with mechanical constraints of the array.

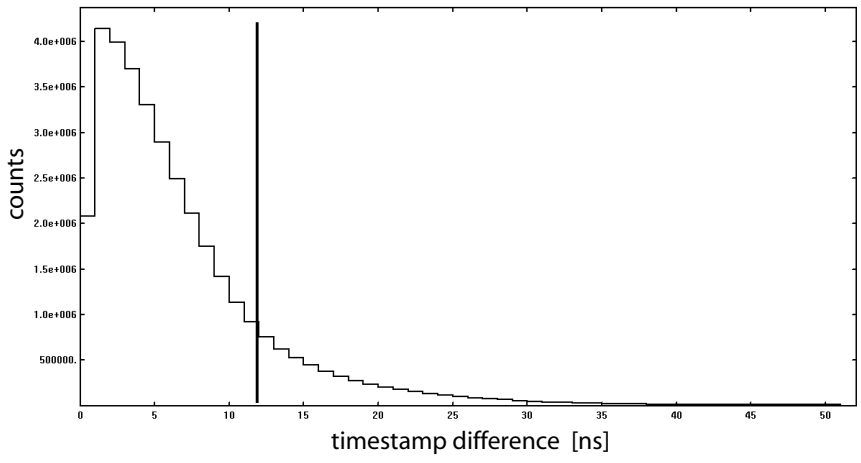

Figure 3.18: Timestamp differences - Histogram of the differences in the timestamps. A selection is done in order to select only correlated events, corresponding to timestamp differences lower than a given value (vertical line).

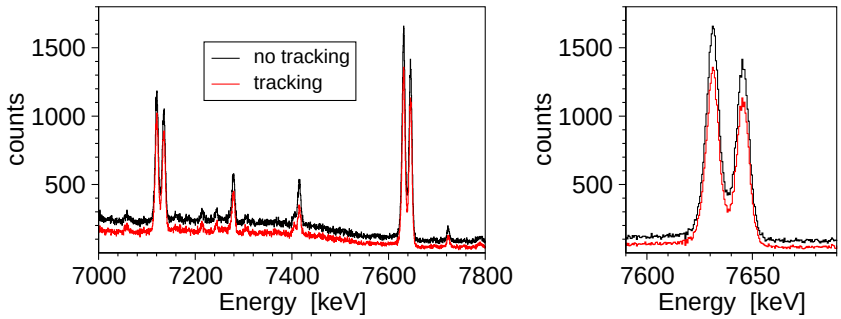

Figure 3.19: Comparison between tracked and sum–event spectra - Comparison between tracked (red) and not tracked spectrum (black), on the left–hand side for γ–ray energies between 7 and 8 MeV (AmBe(Fe) source) and on the right–hand side the 7.63 and 7.64 MeV lines are selected.

A `root-tree` (146) can be written out at this stage, together with a list–mode text file with the hits written in the global reference frame, that can be given as an input to the tracking code by command line. The same procedure is used for the simulated data too.

In Fig. 3.19, the sum energy spectrum (no tracking applied) is compared with the result of the tracking, in case of the AmBe(Fe) source. The data are taken with the AmBe(Fe) source and the energy interval of interest for our experiment is considered. What is apparent from the figure is essentially a reduction in the background. The double–gaussian fit of the doublet in the figure provides the numbers reported in Tab. 3.2.

spectrum	**FWHM(7.64 MeV) [keV]**	$\mathbf{A}_p/\mathbf{A}_{tot}$	$\mathbf{A}_{se}/\mathbf{A}_{fe}$	A(7.63 MeV)+A(7.64 MeV)
tracked	7.38	0.78	0.68	3.7×10^5
summed	7.41	0.69	0.63	4.5×10^5

Table 3.2: Tracked vs sum–energy spectrum for the 7.63 and 7.64 MeV lines - Comparison between tracked and the sum energy spectrum, for the 7.63, 7.64 MeV γ lines. A_p is the area of the peaks in the spectrum of Fig. 3.19 right side; A_{tot} is the integral of the whole region (background included); A_{se} is the area of the single escape peaks while A_{fe} is the one of the full energy ones.

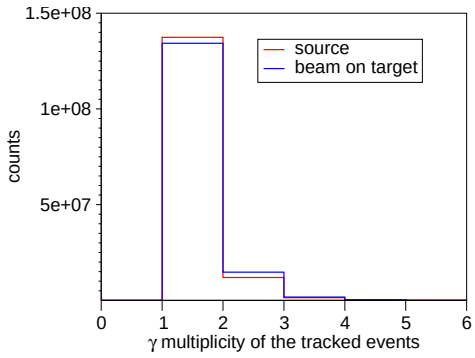

Figure 3.20: Number of detected γ rays per tracked event - Event multiplicity (after tracking) for the AmBe(Fe) source (red histogram) and for the data taken while beam on target (blue).

¿From those values one can see that while the gain in the peak–to–background (roughly estimated from the integral of the region expanded in the right side of Fig. 3.19) is evident, the energy resolution is almost the same, at the cost of ≈20% of statistics. It is worth noting at this point that the tracking algorithms have been developed for high gamma multiplicity events and a detector medium covering 4π. In case of the particular experiment discussed here, the γ–ray multiplicity is mostly 1, as we can see from the histogram of the number of gammas per event in Fig. 3.20. In order to preserve the statistics, one can investigate the possibility of skipping the tracking procedure, i.e. by considering the sum energy of the event and finding a convenient way to identify the first interaction point, for instance by choosing the highest energy one. In Fig. 3.21 the correlation between the angle of the first interaction point reconstructed in the two cases is reported. Since the information on the angle is crucial for the present experiment, more than the statistics, the slight displacement from the diagonal position, evident in the figure, strongly encouraged us to make the "conservative" choice of using the tracked events.

In Fig. 3.22 the spectra reconstructed as Compton and pair production are shown, together with the overall tracked spectrum. As pointed out by Fig. 2.11, the pair production process is present but still Compton scattering is the dominant interaction mechanism. The spectra reconstructed as pair production would constitute a cleaner analysis but the statistics is too low.

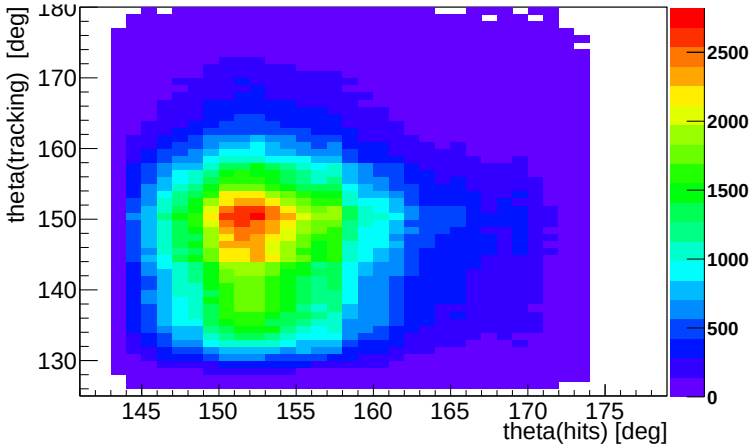

Figure 3.21: Angle of the first interaction point - Angle of the first interaction point as reconstructed with the tracking algorithm vs the angle of the interaction point characterized by the largest energy release in the non tracked event.

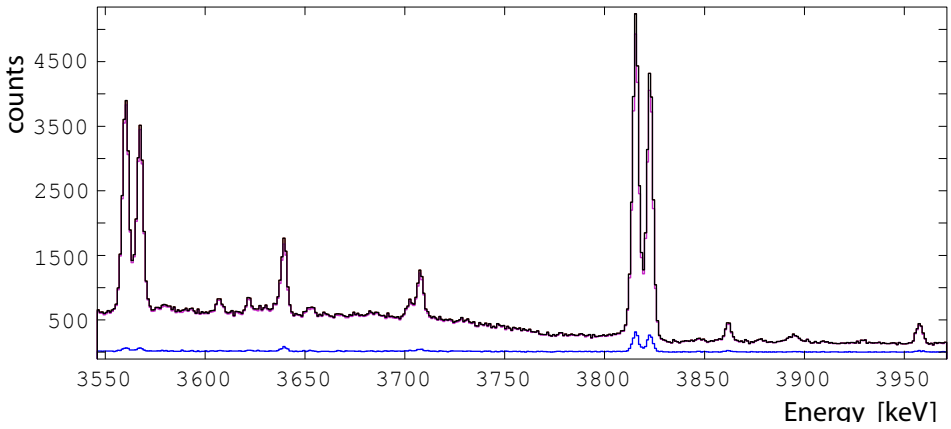

Figure 3.22: Spectra reconstructed as Compton and pair–production - Comparison between the spectra reconstructed as Compton (red) and as pair–production (blue) and the resulting tracked spectrum (black). The Compton scattering is the dominating reconstruction mechanism.

3.2 Data sorting

As a result of the data replay previously described, several parameters are extracted from the raw experimental data: event number (time stamp), gamma energy, gamma time and first interaction point. Other parameters are present but they are not relevant for our analysis. These parameters are thus ready to build correlations, i.e. they can be sorted event by event.

One of the first crucial things to be checked is the population of the produced nuclei, namely ^{15}O and ^{15}N . This is done by inspecting the coincidence events, thus observing the spectra obtained by setting a gate on a gamma–gamma matrix. It is worth noting that we operated the experiment in a trigger–less mode, so there is no coincidence condition on the data stored on disk. Moreover, the gamma rays of interest are

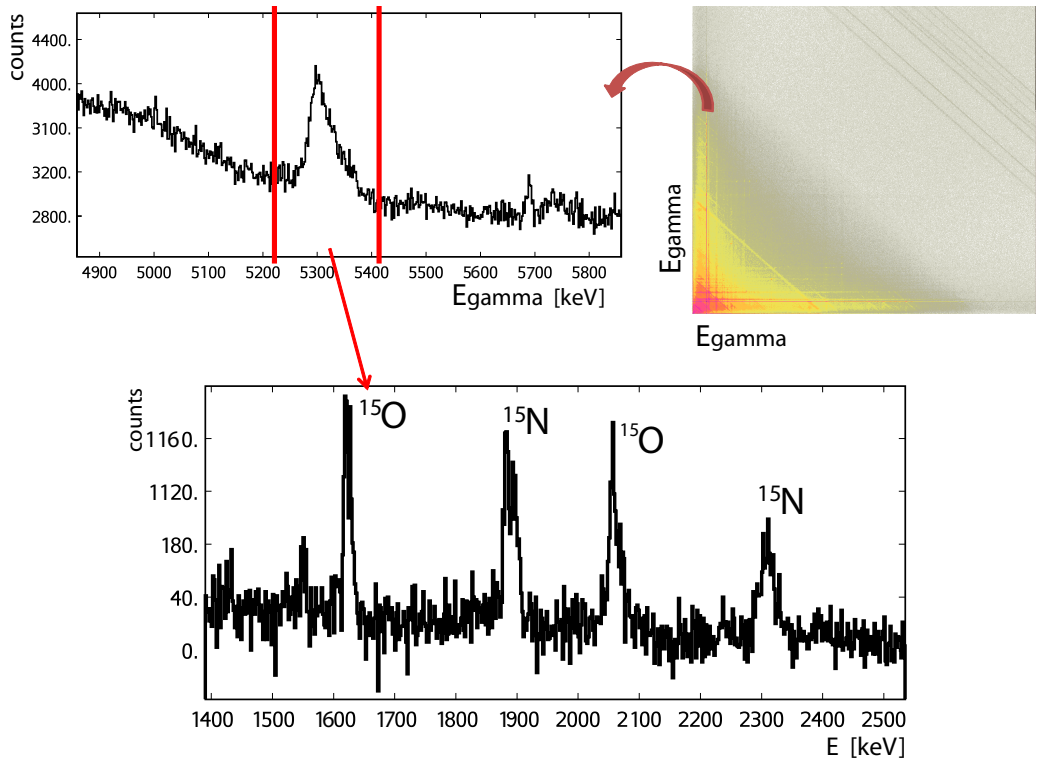

Figure 3.23: Coincidences with a composite gamma line - Gate on the ≈5300 keV gamma line, result from the overlap of two different γ rays in ^{15}O and ^{15}N , on one of the axis of the γ -γ matrix (upper right). The resulting coincidence spectrum is shown at the bottom, and the peaks are labelled by the corresponding emitting nucleus. An average Doppler correction ($\beta = 0.06$, along the beam direction) has been used to this purpose.

of high–energy and mainly of multiplicity 1. Still we can set a gate on a "composite" gamma line –around 5.3 MeV, see Fig. 2.26– and observe the gamma rays in coincidence (Fig. 3.23). Since the ion velocity was not measured event–by–event, the Doppler correction was performed using an average value, which can be set at the Tracking level. The matrix is obtained with the tracked data, imposing an average Doppler correction of β =0.06. This is just a rough approximation, since the kinematics of the emitting nuclei is composite, but the energies in Fig. 3.23 are quite close to the nominal ones (Fig. 2.26 and (41)). ¿From the study of such a matrix we could confirm the level schemes reported in Fig. 2.26. It should be remarked that the level of interest in ^{15}O is directly populated, so that its (predicted) short lifetime is not masked by feeding from long–lived higher levels. Anyway, eventual feeding can be included in the simulation. For the actual data analysis no Doppler correction was considered.

The second matrix we focus on is obtained by sorting the non Doppler corrected energy of the reconstructed gamma rays as a function of the angle θ of the first interaction point with respect to the beam axis, see Fig. 3.24. ¿From this correlation we can see the effect of "short" lifetimes: straight narrow lines correspond to the γ–rays emitted from the AmBe(Fe) source, while the broad tilted lines correspond to the ones following the emission from a short living level while the emitting nucleus is slowing down. They appear as broad and composite structures when projecting on the energy axis (Fig. 3.24 lower panel).

The total angular coverage of the detectors was divided in steps of two degrees (based on the target-to-detector distance and the PSA position resolution (104)). In the following, "angle θ" will refer to the θ interval between θ and θ-2 degrees.

In Fig. 3.25 the projections corresponding to different angles θ are shown. The structures are better resolved and these projection spectra will be used for our analysis. In Fig. 3.26 the lineshape of the 8.31 MeV gamma ray in ^{15}N is shown at different angles. The complex structure of the peak, the energy of which is close to the one of emission in–flight, closely reflects the kinematics, as we are going to discuss later.

The lifetime of the 6.79 MeV state in ^{15}O and of the excited levels in ^{15}N (like the one de–exciting with the γ rays shown in the spectra of Fig. 3.26) will be extracted by means of lineshape analysis techniques, introduced in Sec. 2.1.1.1. Various elements of this method have been revised in this Thesis work and refined in order to adapt it to the

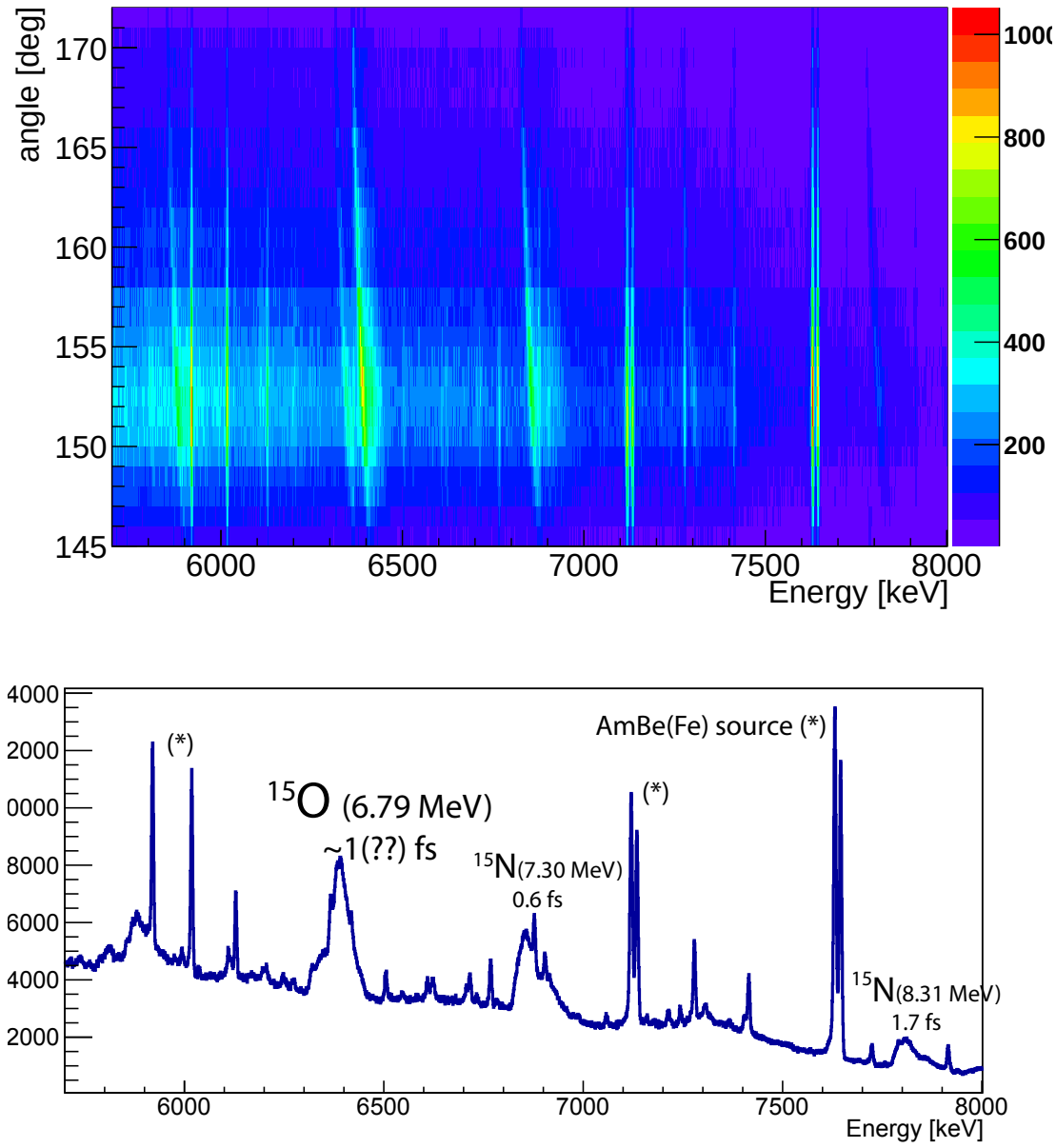

Figure 3.24: γ–ray energy vs θ of the first interaction point - Angular position of the first interaction point θ, with respect to the beam direction, sorted as a function of the energy of the reconstructed γ ray. The narrow straight lines correspond to the emission at rest from the AmBe(Fe) source, while the broad "tilted" lines are gammas emitted while the excited nucleus is moving in the Au layer. In the projection on the energy axis (lower panel) the broad and composite structure are assigned to ^{15}O and ^{15}N.

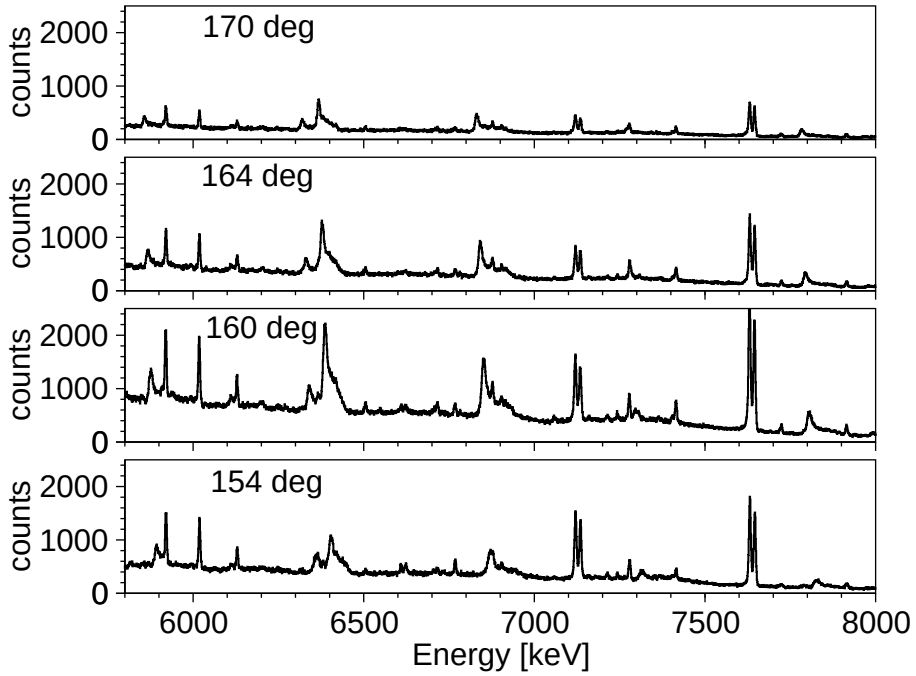

Figure 3.25: Energy spectrum for different "angle θ" slices - Spectra in the $\approx$6-8 MeV energy range obtained by gating on different θ intervals (see text) on the matrix reported in Fig. 3.24.

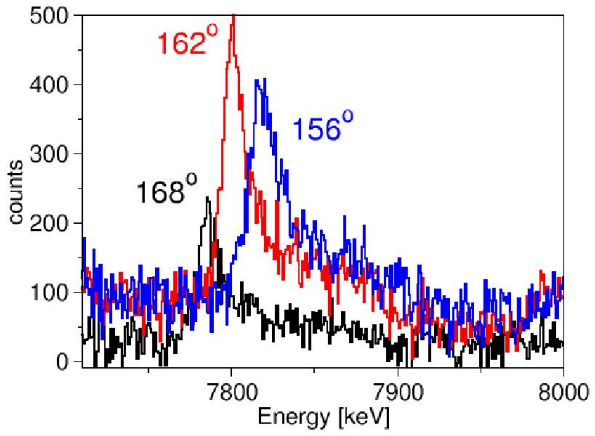

Figure 3.26: Lineshape of the 8.31 MeV line in ^{15}N observed at different angles - Comparison of the lineshape of the peak corresponding to the 7.3 MeV γ in ^{15}N measured at three different angles.

innovative detection technique and to the "extreme" conditions for the measurement of $\approx$ fs lifetimes.

In order to take full advantage of the possibilities offered by a γ–ray tracking array as the AGATA Demonstrator, the lineshape analysis has to rely on sophisticated Monte Carlo simulations, that we are going to discuss in the following Chapter, before describing the data analysis in Chapter 5.

4

Monte Carlo simulations for lifetime measurements with Doppler shift techniques

As it was discussed in Sec. 2.2.3.1, several of the planned (now performed) experiments for the campaign of measurements of the AGATA Demonstrator Array at the Laboratori Nazionali di Legnaro aimed at measuring transition probabilities in exotic nuclei. Therefore, many users within the AGATA community were interested in evaluating in a consistent way the expected performance of the device in this kind of measurements. This requirement demanded for an extension of the original Monte Carlo code for AGATA in order to properly include the effects of the nuclear lifetimes and of the interaction of the excited nuclei with the surrounding media. In the revised code, not only the ion is followed from its initial conditions –at the moment of the production in the target– but also the γ emission is properly handled, so that the user has not to care about any a posteriori solution of the Bateman equation (e.g. (147)).

It soon turned out that this improved Monte Carlo code could be not only a valuable predictive tool, but that it would be essential to analyse measurements such as that described in the present Thesis. The basic ideas of MC simulations for lineshape analysis are described in Sec. 2.1.1.1 and (63). As a matter of fact, given the peculiar data treatment within the AGATA project, as with any other γ-ray tracking array (see Chap. 2), the response function of the device cannot be easily schematized and separated by the history generation described in Sec. 2.1.1.1. Therefore, a more complex

code, combining both the history generation and the detailed response function of the tracking array, was needed to perform our analysis. The revised Monte Carlo code for AGATA proved flexible enough to become one of our tools for the analysis of the present data.

In this Chapter, after briefly recalling the main features of the original Monte Carlo code for AGATA and of the `Geant4` package, on which the code is based, we will describe the major changes needed to include the effects of the nuclear lifetimes and of the interaction of the excited nuclei with the target/degrader. We will show, through the comparison between simulated and experimental data, how the code works and therefore that it is suited as a tool for our analysis, which will be the subject of Chap. 5.

4.1 Simulations with the `Geant4` package

Monte Carlo (MC) simulations are powerful and fundamental tools in order to plan and analyse modern High–Energy Physics (HEP) and Nuclear Physics (NP) experiments. Several packages have been developed within these communities to help the users develop their own simulation code. One of the most widely used is the `Geant4` package (138). It provides tools for the description of complex geometries, the interactions of particles with matter and the retrieval of all the relevant information the user needs from a physics process. `Geant4` exploits the versatility of object–oriented C++ programming. The user in his "main" code –Fig. 4.1– has to call the constructors of mandatory classes, connected with arrows to the "main" box in Fig. 4.1. These

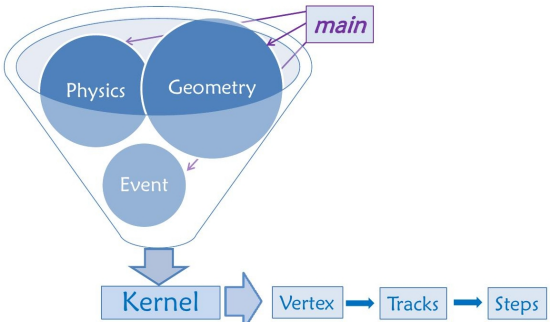

Figure 4.1: `Geant4` philosophy - Block diagram of the `Geant4` basic, mandatory classes: the user, in his "main" program, has to call the constructors of these classes, i.e. define the geometry, the kind of event and the physics behind.

mandatory classes are user–defined and independent from one another when calling the constructors. As represented in Fig. 4.1, the user must provide the specific geometry of the setup (*DetectorConstruction*), the kind of events to be processed (*PrimaryGeneratorAction*) and the processes characterizing the involved particles (*PhysicsList*). This information is processed by the `Geant4` kernel, that will produce the history of each particle, created in a "vertex", in discrete steps. The steps contain all the relevant information, that is available for the user and can be retrieved and used by implementing additional user classes.

In this way, each particle (primary and secondary) is followed in the emission and interaction with the surrounding medium (detectors and eventual dead materials). In particular, the models for the interaction of gamma–rays with matter are successfully included and they have been tested to be reliable.

4.2 The AGATA simulation code

The `Geant4` capabilities have been exploited in order to plan the geometry of the AGATA array and to test the tracking algorithms. Simulations were indeed needed to optimise the geometry of the array, to evaluate the expected experimental performance and to test the tracking and analysis programs with "standard" datasets (109, 110). The `Agata` simulation code has been written for this purpose, as extensively described in (109). Here we will just recall the general features.
The geometry of the array is not directly hard–coded and can be changed by modifying geometry files. This allowed for realistic simulations for the AGATA Demonstrator phase at the LNL, and an easy adaptation to the next phases in other European laboratories (as it is currently at GSI (148)). The schematic emission of photons and particles has been implemented within the simulation. When more "realistic" events are needed, it is possible to decode the event structure and sequence from a formatted text file, using the `Agata` code merely to evaluate the response function of the detector arrangement to such pre-generated events, which can contain fine details such as the directional correlations in a cascade of γ-rays.

A basic requirement of the code was to disentangle each scattering sequence in order to verify the results of the tracking process. Thus, one particle or photon is emitted at a time in the simulation process, making it easier to follow each scattering sequence.

High-multiplicity events can be emulated at the level of the subsequent analysis, namely of the γ-ray tracking code, where the actual event multiplicity can be specified.

The tracking process in itself is not included in the `Agata` code, which basically produces just a formatted text file in list-mode where n-tuples are stored, each of them listing position and energy of the individual depositions within the active parts of the array. These data can be subsequently processed with "standard" tracking codes. Here it should be observed that the results provided by the simulation code are given with infinite precision both for the energy and for the position of the interactions. In order to emulate the finite precision of the pulse shape algorithms in the identification of the interaction points, the raw simulated data are packed together and smeared assuming a three-dimensional gaussian distribution. Following this packing and smearing process, spectra and matrices can be produced by processing the list-mode files with a tracking algorithm, where the effects of the finite energy resolution of the detectors are also taken into account.

In order to have the possibility to run in batch mode, no graphical user interface is provided, but rather several built-in commands are given to set the relevant parameters of the simulation.

4.3 Extension of the code to include complex level scheme and nuclear level lifetimes

What are the limitations of the above described code when dealing with the simulation of lifetime effects? The "standard" `Agata` code does not include any effect of interaction between the excited nucleus and the target (or an eventual additional layer, like the degrader). In order to overcome this limitation, we implemented another event generator, similarly to what P. Adrich et al. (149) did for the simulation of plunger experiments at NSCL (150). In the geometry description, target and degrader have been added, as well as new classes for the handling of the reaction in the target (or degrader, *Incoming–OutgoingBeam* Fig. 4.2). The excited nucleus, produced in such reaction process, decays while slowing–down in the material. The energy and angular distributions of the emitted nuclei can be provided in an external text file. Still, the major limitation of this preliminary version of the code was the consideration of a single level decaying exponentially, excluding the possibility of reproducing effective

lifetimes, i.e. cascades of gammas de–exciting nuclear levels with different lifetimes. It has been thus decided to rely upon the built–in capabilities of the `Geant4` libraries, i.e. the *PhotonEvaporation* library (151), which describes the de–excitation of excited nuclei through complex level schemes. However, it turned out that in the `Geant4` version used (4.9.2p04), the displacement of the excited nucleus while emitting the gamma ray was not correctly taken into account[1]. The *G4PhotonEvaporation* library had thus to be modified. In our modified version of the library, the excited nuclei decay through the standard *G4PhotonEvaporation* only in case of zero lifetime. When the lifetime of the excited level is different from zero, the more general *G4Decay* process is called. The final states are chosen on the basis of the nuclear level scheme present in the *G4DataBase*, by creating the relevant *G4DecayChannel* objects and registering them

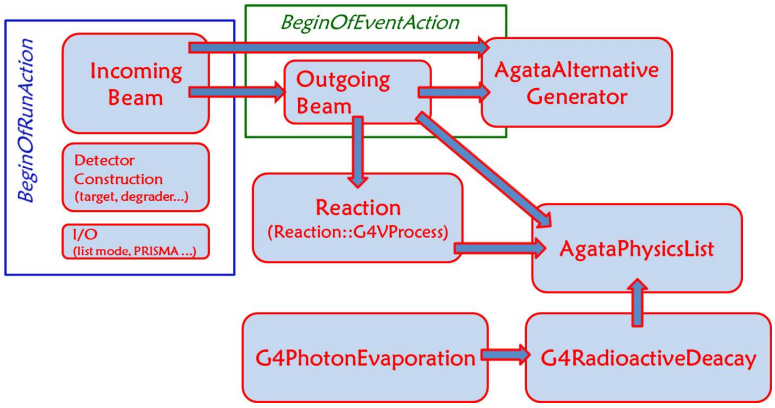

Figure 4.2: Conceptual organization in classes of the simulation code - Block diagram with the new classes introduced in the `Agata` code for the simulation of Doppler shift lifetime measurements and production of complex level schemes. The name of the used classes is reported in the boxes, connected by arrows that indicate the logical flow of information from one class to the other. Both the event generator (*AgataAlternativeGenerator*) and the physics process (*AgataPhysicsList*) retrieve the information from the *OutgoingBeam* class. Its arguments (variables and methods) are related with the reaction products (as Z, A and kinematics) and use the information provided by the *IncomingBeam* (as beam energy, beam nucleus –Z, A– beam profile) and *DetectorConstruction* (target, degrader/absorber) classes. The *Reaction* (inheriting from *G4VProcess*) class is used to control the beam–target and produced nucleus–target/absorber interactions. The *G4RadioactiveDecay* process has been added to the *PhysicsList* and the *G4PhotonEvaporation* library extensively modified (see text for more details).

[1]This problem is not yet fixed in the latest release (4.9.6).

in the *G4DecayTable*. The possibility to decay without photons in order to mimic the side–feeding from unobserved levels is also included. The class structure of the modified part of the code is reported in Fig. 4.2. Concerning the *Agata* user code, it was further modified in order to provide a better description of the target/degrader setup, including the possibility to consider a generic distribution of target nuclei and some energy dependence of the reaction cross–section. The *OutgoingBeam* class has been extended in order to consider up to four reaction mechanisms (or, in other words, energy and momentum distributions for the excited nuclei), with the limitation that only one kind of nucleus in the exit channel is considered (with the possibility to consider a distribution of entry levels):

- fusion–evaporation: a generic spectrum of the energy of the evaporated particle(s) in the center of mass can be provided from file; in alternative, a gaussian distribution in the center of mass can be used (with isotropic angular emission), providing centroid and sigma;
- (multi)nucleon transfer: the differential cross-section as a function of the angle and the energy must be provided from file;
- Coulomb–Excitation (not yet implemented);
- transfer reaction followed by fission of the target–like nuclei (not yet implemented);

As an example of the ingredients such a simulation has to be fed with, a typical macro used to generate a data file for the simulations for the analysis of our experiment is reported in Fig. 4.3.

The test of the modified version of the code was done through the comparison of simulated and existing datasets from the AD campaign. The code resulted useful both to plan experiments and to analyse them. In the following the results of the tests are reported, for which a preliminary version of the code was used, that made us confident that everything was working fine.

4.3.1 Preliminary test of the code with some experimental data

The revised version of the code and of the libraries was extensively tested through the comparison with existing experimental data (152). The examples presented here

```
## Reaction ##
/Agata/generator/emitter/BeamIn/Z 7 # projectile Z
/Agata/generator/emitter/BeamIn/A 14 # projectile A
/Agata/generator/emitter/BeamIn/KE 32 MeV # projectile energy
/Agata/generator/emitter/BeamOut/DZ 1 # Z reaction product - Z projectile
/Agata/generator/emitter/BeamOut/DA 1 # A reaction product - A projectile
/Agata/generator/emitter/BeamOut/Z 1 # target Z
/Agata/generator/emitter/BeamOut/A 2 # target A
/Agata/generator/emitter/BeamOut/ProjectileExcitation 6791.4 keV # excitation energy of the produced nuclei
## Geometry ##
/Agata/detector/targetMaterial Gold # target material, in our case: absorber
/Agata/detector/targetSize 10 10 3.86 # linear transversal dimensions of the target [mm] and thickness [mg/cm^2]
/Agata/detector/traslateArray 0 0 -54.4 # AGATA position with respect to the nominal distance
/control/execute macros/geom180-Demo.mac # macro file setting the geometry of the detectors to the AGATA Demonstrator (size and position of the detectors decoded from external files)
/Agata/detector/update

/Agata/file/enableLM # enable list mode output
/grdm/allVolumes # enable radioactive decay mode in all volumes composing the geometry

## distribution of reaction points according to "profile.dat"
/Agata/generator/emitter/disableUniformDistr # disable uniform distribution of target nuclei in order to read it from file

/Agata/generator/emitter/BeamOut/setEvapNumberN 1 # number of evaporated neutrons
/Agata/generator/emitter/BeamOut/enableEvapFromFileN # evaporation energy spectrum read from file

/Agata/generator/emitter/BeamOut/setPfe 0.3 # fusion–evaporation probability set at 30% with respect to the total interaction probability
/Agata/generator/emitter/BeamOut/setPtr 0.7 # nucleon–transfer probability set at 70% with respect to the total interaction probability; angular distribution of the produced nucleus read from file

/run/beamOn 100000000 # number of events to be simulated
```

Figure 4.3: Simulation macro file - Example of macro file used for the simulation used for our analysis. In particular, the 6.79 MeV level in ^{15}O is considered. For a brief description of the different inputs see the comments (sentences beginning with "#", in italic font). The lifetime of the simulated level(s) is changed in the *Decay Table* of the given nucleus (*G4Data*), decoded from an external data file. The decay pattern indicated in this table is followed.

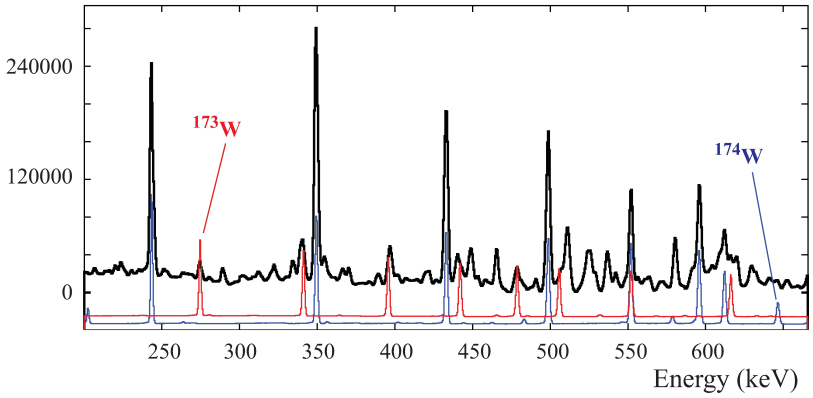

Figure 4.4: Simulated spectra of complex level schemes following fusion–evaporation reactions - Comparison between the experimental spectrum for the ^{50}Ti(217 MeV) + ^{128}Te reaction (thick black line) and the simulated spectra for one band of ^{173}W (thin red line) and one band of ^{174}W (thin blue line). γ-rays were detected with the AGATA Demonstrator.

were produced with an early implementation of the code, where the distribution of entry levels of the residual nucleus was still missing and had to be reproduced by an adequate combination of independent simulations.

The capability to handle quite complex level schemes is shown in Figure 4.4, where the experimental data, sketched with a thick black line, refer to the ^{50}Ti(217 MeV) + ^{128}Te reaction (131). γ-rays were detected with the AGATA Demonstrator. The simulated spectra assuming photon emission from one band of ^{173}W (5n evaporation channel) and one band of ^{174}W (4n evaporation channel) are sketched respectively with thin red and blue lines. The intensity and the branching ratios are reproduced in a satisfactory way. In Figure 4.5, the experimental (thick black line) and the simulated data (thin blue line) for the ^{16}O(64 MeV)+^{108}Cd reaction, leading to ^{122}Ba as the 2n evaporation channel, are compared (153). In this case, a thick target was used to extract lifetimes through the DSAM technique. The spectra of Figure 4.5 were obtained with the detectors of GASP in Configuration II positioned at 35° with respect to the beam direction. Also in this case there is good agreement between the experimental and the simulated data. The remaining discrepancies are most likely due to the side–feeding from higher–lying levels, not yet taken into account in the simulation code.

The spectra presented in Figure 4.6 refer to the ^{76}Ge(577 MeV)+^{238}U reaction.

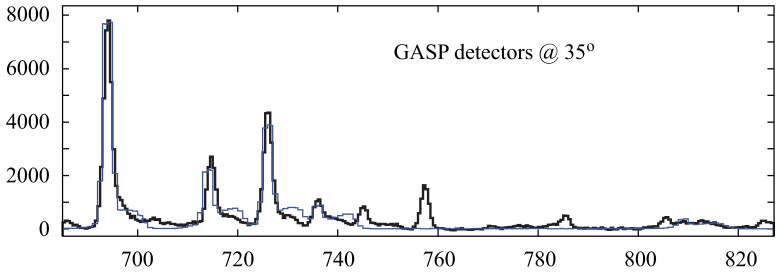

Figure 4.5: Simulated lineshapes of gamma peaks produced in fusion–evaporation reactions - Comparison between the experimental (thick black line) and the simulated data (thin blue line) for the ^{16}O(64 MeV)+^{108}Cd reaction, leading to ^{122}Ba as the 2n evaporation channel. The GASP detectors positioned at 35° with respect to the beam direction are considered here.

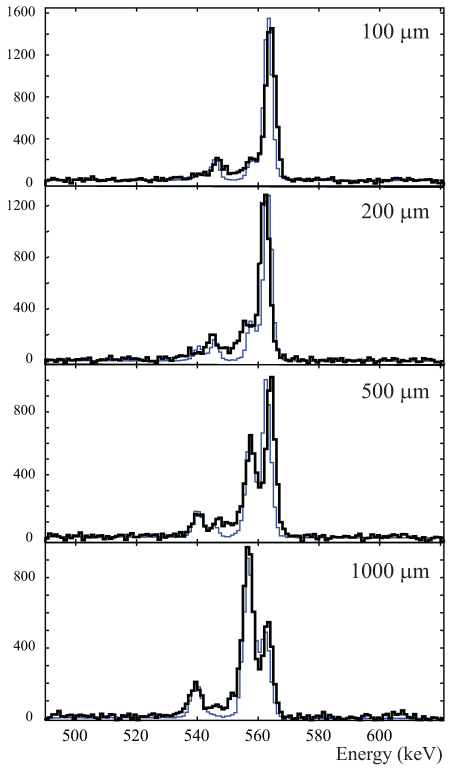

Figure 4.6: Simulated spectra for a differential plunger measurement - Comparison between the experimental (thick black line) and the simulated data (thin blue line) for the $2_1^+ \rightarrow 0_1^+$ transition of ^{76}Ge, populated in the ^{76}Ge(577 MeV)+^{238}U reaction. Four different target-degrader distances were considered here.

In this case, the aim was to measure lifetimes with the RDDS method (differential plunger), using the AGATA Demonstrator coupled to PRISMA (127, 134). The experimental (black) and the simulated (red) data for the ^{76}Ge quasi-elastic channel, measured at four different target-degrader distances, are compared in Figure 4.6. In the simulation, it was assumed to populate the 2_2^+ level at 1108 keV with an intensity of 30%, the remaining intensity going into the 2_1^+ level at 563 keV. In the simulation, the major simplification of assuming a "sharp" distribution in energy/direction of the ^{76}Ge excited ions was considered, having fixed that the energy and initial trajectory point towards the optical axis of PRISMA. Nevertheless, due to the interactions within target and degrader, in order to perform Doppler correction of good quality it was mandatory to exploit the full information from PRISMA also with the simulated data, similarly to what was performed in (154). Despite the approximation, the agreement between the experimental and the simulated data for the $2_1^+ \rightarrow 0_1^+$ transition, shown in Figure 4.6, is quite good.

After being confident of the fact that the results of the simulation were reliable, other major adjustments and developments have been performed in the framework of the analysis of our experiment. They will be described in the following Chapter, along with the data analysis.

5

The lifetime of the 6.79 MeV state in ^{15}O

In this Chapter we will discuss the actual lineshape analysis performed for the determination of the lifetime of the 6.79 MeV state in ^{15}O and of the 8.31, 10.06 MeV states in ^{15}N . The construction of the spectra for the final analysis and the error propagation will be outlined. The most representative χ^2 curve will be reported and examples of lineshape fits will be shown.

5.1 Data analysis

In order to perform the present lineshape analysis, the capabilities of the AGATA Demonstrator to measure the angle of the first interaction point of each photon with respect to the beam axis in a "continuous" way were fully exploited. This is in practice achieved by analysing the lineshapes of the gamma peaks reconstructed in different θ slices of 2°, as shown in Fig. 3.24 and Fig. 3.25. As mentioned previously, the choice of a 2° angular interval is reasonable considering the target–to–detector distance and the expected position resolution provided by the PSA algorithms, which gives an average "angular" resolution of $\approx 2°$. Concerning the position resolution, it should be remarked that the experimental measurement reported in Fig. 16 of (104) extends up to $E_\gamma \approx 4$ MeV, where a value of ≈ 4 mm is obtained. Considering the overall trend, we can safely assume that the position resolution for higher energy gammas is of the same order. We will refer hereafter as $\mathcal{S}_\theta$ to the spectrum $\mathcal{S}$ corresponding to the angular

interval $(\theta, \theta - 2)$.

In order to compare the experimental and the simulated spectra a χ^2 function can be built:

$$\chi^2 = \sum_{k=\mathrm{low_{lim}}}^{\mathrm{up_{lim}}} \left(\frac{Exp(k) - Sim(k)}{\sigma_{Exp}} \right)^2 \tag{5.1}$$

where k is the channel of the region in the spectrum selected for the fit. The experimental and properly normalized simulated spectra are respectively $Exp(k)$ and $Sim(k)$, while σ_{Exp} is the error on the experimental spectrum. In principle an error σ_{Sim} should be considered for the simulated data, which however can be neglected by taking into account simulations with "infinite" statistics, i.e. with statistics much larger than the experimental data. The content on each channel of the "raw" spectra is considered to be ruled by Poisson statistics, so that the statistical error for the spectrum $\mathcal{S}$ is deduced considering the variance equal to the channel content, i.e. $\sigma^2_{\mathcal{S}} = \mathcal{S}$.

It should be pointed out that in our case the detectors were not distributed isotropically around the target position, in other words they were covering only a fraction of the total solid angle. For this reason, not all the θ angles show the same level of statistics, since at the borders of the array the lack of detection material results in increased escape and background probabilities.

In order to perform the present analysis, some operations (implemented in a C++ code written specifically to this purpose, treating the spectra as N–tuples with the corresponding errors) are performed on the following sets of spectra, where θ labels the selected angular slice in Fig. 3.24 and k is the channel number:

- $B_\theta = B_\theta(k)$: energy spectrum obtained from the in–beam data, where both the γ rays from the reaction products and the ones from the radioactive source are present;
- $R_\theta = R_\theta(k)$: spectrum obtained off–beam from the AmBe(Fe) radioactive source;
- $S^{\tau,p}_\theta(k)$: simulated spectrum corresponding to a lifetime τ and to a fraction p of fusion–evaporation with respect to nucleon–transfer ($p = 0, 1$ when only nucleon transfer and fusion–evaporation are considered, respectively).

Rather than producing a full Monte Carlo simulation comprehensive of all the possible sources of background (e.g. radioactive source or contaminant lines from other nuclei),

we decided to "clean up" the experimental spectra, since this will result in a better (safer) treatment of the errors.

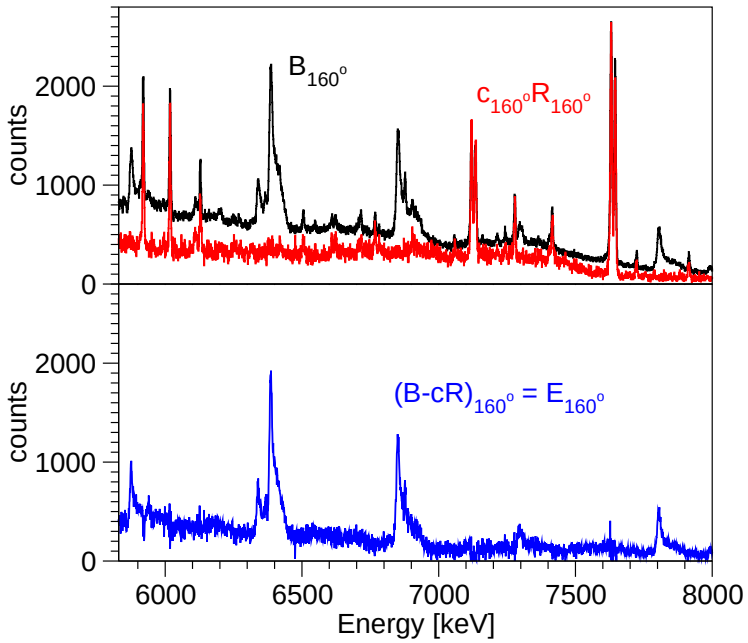

Figure 5.1: Source subtracted spectra - Example of subtraction of the source spectrum (red, "R") from the reaction one (black, "B"), for the $\theta = 160^o$ slice. The resulting spectrum (blue, "E") is also shown. The source spectra are normalized to those in–beam through the c_θ coefficients discussed in the text.)

In Fig. 5.1, the first step in the construction of the spectra to be analysed is illustrated. In order to "clean" the γ peaks of interest, the background induced by the AmBe(Fe) source (red spectrum) should be subtracted from the in–beam data (black spectrum). The normalization coefficients needed to perform the subtraction in a proper way have been determined, for each θ angle, by evaluating the areas of the 7.63 MeV–7.64 MeV doublet and of the 9.30 MeV γ line (see Fig. 3.14). These peaks have been chosen as the "cleanest" in the B spectra. The two independent evaluations (corresponding to the two components of the doublet) of the normalization coefficients have been combined via weighted average. The final adopted c_θ values are shown in Fig. 5.2. The error on the source–subtracted spectrum $E = B - R$ is obtained with statistical error propagation, $\sigma_E^2 = \sigma_R^2 + c\sigma_B^2 + B\sigma_c^2$.

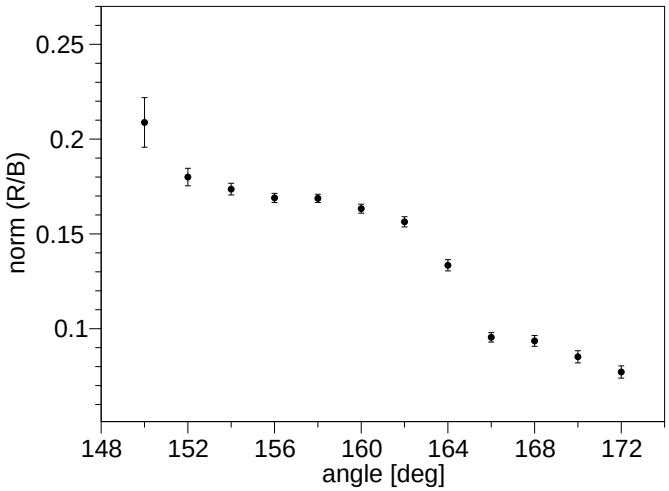

Figure 5.2: Normalization coefficients used for the source subtraction - The coefficients have been obtained from the weighted average of those determined considering the 7.63 MeV, 7.64 MeV and 9.3 MeV gamma lines.

Here it should be recalled that, for each γ peak, the centroid, area and width are extracted after considering the subtraction of a linear background, of the form of Fig. 5.3 (see formula in caption). A "simple" linear background is a reasonable assumption in the high–energy range of interest, where the background is quite small. The identification of the background regions, straightforward for isolated gaussian peaks, resulted from a careful evaluation angle by angle in case of the experimental data. For the "clean" spectra provided by the simulation we rely instead on an automated procedure.

A further manipulation is needed on the spectra, of the kind reported in blue in Fig. 5.1, before performing the final comparison with the results from the Monte Carlo simulations. As it is evident, for instance, from Fig. 3.19 and Tab. 3.2, the single (and double) escape peaks are still present even after the γ–ray tracking. From the level schemes (Fig. 2.26) one can notice that the 7.3 MeV level in ^{15}N differs by about 510 keV from the level of interest in ^{15}O . Even considering the Doppler effect, the single escape peak appears as a peak at the left–hand side of the 6.79 MeV line. As it was mentioned previously, the spectrum reconstructed as pair–production would be a better (cleaner)

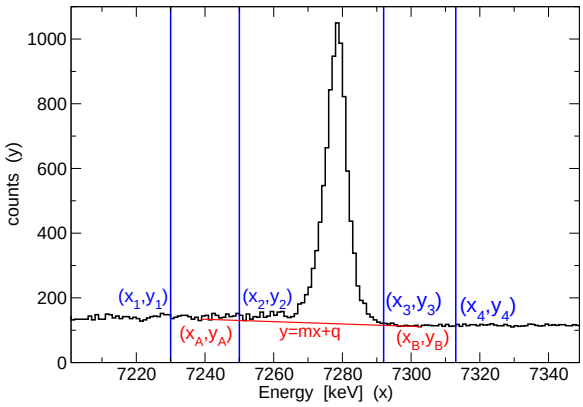

Figure 5.3: Background subtraction - (Stopped) γ–ray peak, $\hat{S}$, as an example of linear background subtraction. The baricenter of two background intervals are considered –(x_A, y_A) and (x_B, y_B)– and the background is the line passing through these points (155). Indicating with $\hat{\mathrm{S}}$ the background–subtracted spectrum, $\sigma^2_{\hat{\mathrm{S}}}(k) = \sigma^2_{\mathrm{S}}(k) + (\frac{x_A-k}{(x_B-x_A)(x_2-x_1+1)})^2 \sum_{k=x_1}^{x_2} \sigma^2_{\mathrm{S}}(k) + (\frac{k-x_A}{(x_B-x_A)(x_4-x_3+1)})^2 \sum_{k=x_3}^{x_4} \sigma^2_{\mathrm{S}}(k)$.

choice but the statistics is too low to use it for the analysis.

In Fig. 5.4, the same spectrum shown in Fig. 5.1 (black) is compared with its "single–escape" partner, namely the same spectrum shifted on the left by 511 keV, $\hat{E}$: $F = E - c_e\hat{E}$. The coefficients c_e for the subtraction of the escape peaks have been determined by the weighted average of those obtained from the ratios between the single–escape peak and the full–energy peak of the source (stopped) lines. They are extracted for each angle and they range between 50% and 70%. The final adopted normalization coefficients for the escape subtraction are reported in Fig. 5.5.

5.1.1 The simulated spectra

As described in Sec. 4, the simulation output can be analysed with the same tracking program used for the experimental data, namely the *mgt* tracking code. The experimental setup sketched in Fig. 2.25 was simulated, using macro files similar to the one reported in Fig 4.3. For each excited level of energy E_L, a number n_τ of lifetimes was simulated, considering both fusion–evaporation and nucleon transfer reactions. The resulting spectra were then combined (added) to account for different fractions p_{fe} of

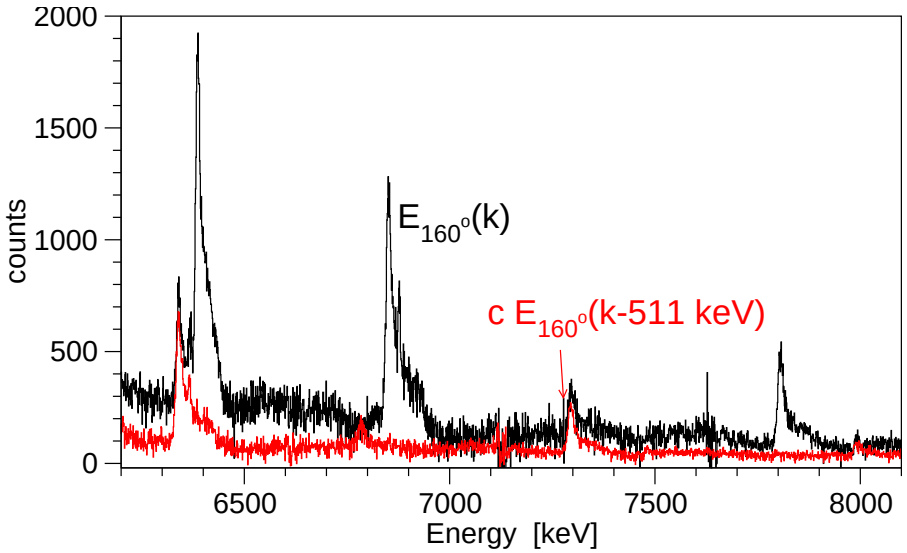

Figure 5.4: Escape subtraction - The spectra obtained with the procedure illustrated in Fig. 5.1, are further treated by subtracting the $\hat{E}$ spectrum, namely the same spectrum shifted by 511 keV on the left and properly normalized.

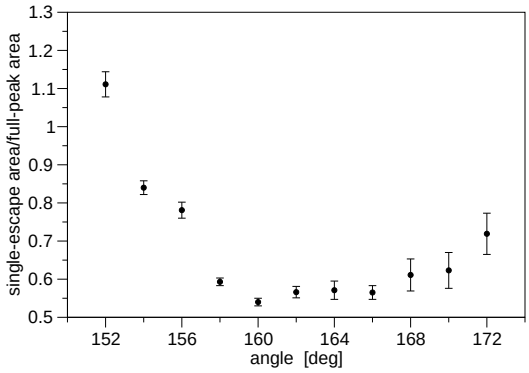

Figure 5.5: Normalization for the subtraction of the escape peaks - The coefficients c_e have been obtained from the weighted average of those determined considering the 7.63 MeV, 7.64 MeV and 6.02 MeV gamma lines.

fusion–evaporation with respect to direct process. For each level, we thus obtained a set $S_\theta^{\tau,p_{fe}}$ of simulated spectra. For each simulation of the direct process 5×10^8 events were considered, while for the fusion–evaporation parts, 10^7 events were simulated. In order to speed–up the run of the simulations a bash script and the possibility to use the different processors of the same computer were exploited.

In the spectra thus obtained, the Compton background has to be subtracted spectrum by spectrum. This was performed using an automated procedure, giving automatic background search and subtraction from the different simulated spectra, that relied on a routine written to this purpose.

The inputs of the simulations can be summarized as follows:

- geometry of the AGATA Demonstrator;
- profile of the deuterium distribution (Fig. 2.28);
- characteristics of the reaction and produced isotope;
- kinematics of the reaction product: angular distribution for the transfer process (Fig. 5.10) and evaporation spectrum for the fusion–evaporation part;
- level scheme of the emitting nucleus (E_γ, branching ratios, lifetime).

Concerning the kinematics of the reaction product, in Fig. 5.6 the partial contributions of the relevant processes to the final simulated lineshape of the 6.79 MeV line are shown, for the full angular coverage and for two selected slices. In particular, it soon turned out that in order to reproduce properly the experimental lineshape, a schematic treatment of the transfer process was not sufficient, and one has to rely on more complete calculations such as those that will be described later.

In order to mimic the PSA output of the experimental data, the simulated interaction points inside the same segment have been packed together. Moreover, a FWHM calibration can be fed to the tracking code, including the parametrization of a left tail (still present in the experimental data even after the neutron–damage correction). To have a "quantitative" idea of how good is the adopted modeling of the response function of the system, a χ^2 analysis has been performed with the same programs used for the lifetime analysis on some of the source peaks. The stopped peaks are simulated with the response function that will be used also for the other data. The normalization

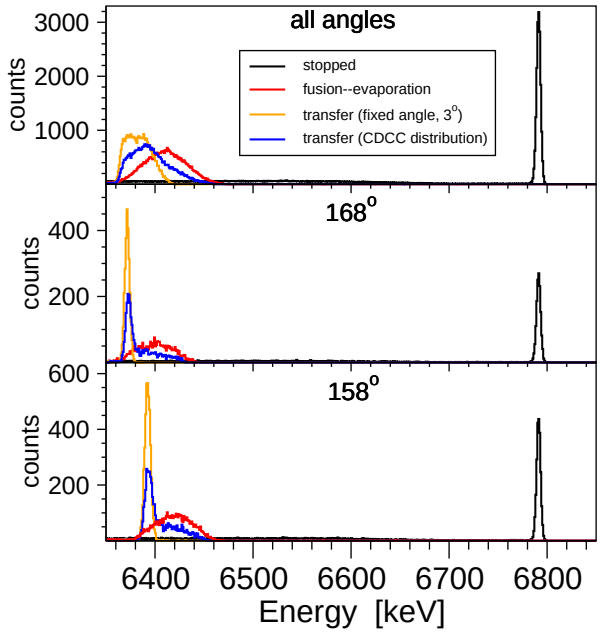

Figure 5.6: Evolution of the lineshape with increasing complexity of the kinematics - Simulated spectra for the 6.79 MeV level in ^{15}O excited in the ^{14}N (32 MeV)+d reaction. The partial contributions of the different reaction processes are shown.

coefficient is the only free parameter in the fit. The χ^2 has been evaluated with Eqn. 5.1 and examples of the comparison between simulated and experimental spectrum for a given angle are reported in Fig. 5.7, proving that the effective response function of the detectors is well taken into account.

The normalization of beam data to simulated data is done in the chi–square routine, with a recursive procedure that starts from the ratio of the integrals of the spectra, and "optimizes" it in a few steps.

Before discussing the results of the χ^2 analysis, we will give an overview of the calculations of the reaction kinematics, which were used as an input to the simulations.

5.1.1.1 Calculations of the kinematics for the ^{14}N(d,n) and ^{14}N(d,p) reactions

As previously discussed, the kinematics of the emitting nuclei is an essential ingredient in the lineshape analysis, and it should be properly taken into account in the simula-

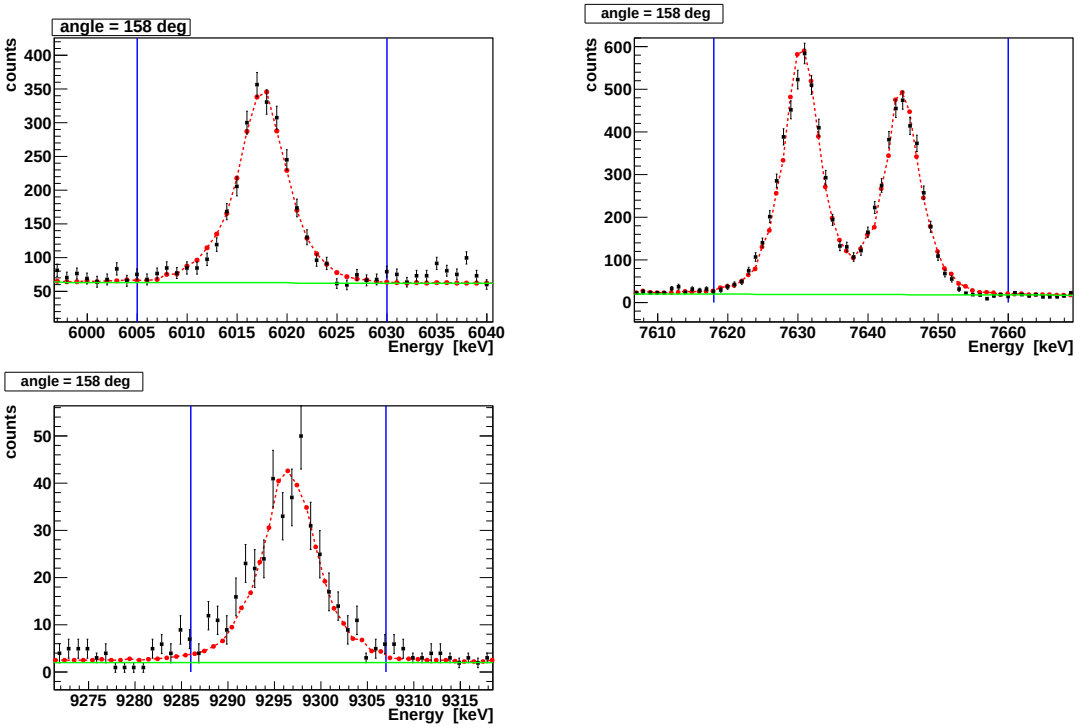

Figure 5.7: χ^2 on stopped lines. - Examples of χ^2 analysis on the source (stopped) lines, performed in order to verify the modeling of the detector response function. An overall reduced χ^2 of 1.7, 3.5 and 2.3 was obtained for the 6018 keV, 7631 keV–7645 keV doublet and 9298 keV gamma lines respectively. The intensity ratio between the 7.63 and 7.64 MeV gamma lines have been determined from the experimental data.

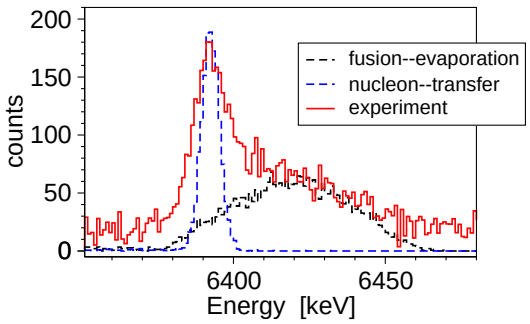

Figure 5.8: Nucleon–transfer and fusion–evaporation components in the γ line-shape - Comparison of the experimental data with the nucleon–transfer and fusion–evaporation components for the 6.79 MeV line (Doppler-shifted to lower energies).

tions. For the reactions we are considering, namely ^{14}N(d,n) and ^{14}N(d,p), the transfer process is the dominant part. In Fig. 5.8, the experimental peak shape is compared with what one would expect in case of "pure" (schematically treated) nucleon transfer or fusion–evaporation kinematics. It is clear that both mechanisms should be properly taken into account in order to reproduce the experimental data, although major care should be given to the dominant nucleon transfer part, that is particularly influencing the lower energy part of the γ peak. It is worth recalling that the selection of the exit channel and the measurement of the energy and angular distribution of the emitting nuclei was not feasible in our case, thus we had to rely on existing data or on theoretical calculations in order to properly describe the reaction kinematics within the simulations.

Examples of measured cross–sections for the ^{14}N(d,n) and ^{14}N(d,p) reactions can be found in the literature for reaction energies differing from the one used in our experiment (156). Therefore, the only feasible option was to rely on theoretical calculations in order to carry on the analysis.

The reaction kinematics was modelled using calculations by N. Keeley. They have been performed using the FRESCO code (157) for CDCC (*Continuum Discretized Coupled Channel*) (158) combined to the CRC (*Coupled Reaction Channels*) calculations. Differently from the "classical" DWBA (*Distorted Wave Born Approximation*), within the CRC scheme the coupling with the excited states in the final channel(s) is taken into account. The CDCC part properly adds the deuteron breakup states (coupling to the continuum) that have been proven to be very important when considering transfer reactions involving deuterons (159).

In Fig. 5.9 the experimental data available from (156) for the reaction ^{14}N(d,p) are compared with the DWBA and the CDCC-CRC calculations. The agreement of the CDCC-CRC calculations with the experimental data is quite good. Compared to the DWBA calculations, one can notice a better agreement also at larger angles in the center of mass. The distribution at larger center–of–mass angles underestimates, however, the experimental data. In this angular region, the fusion–evaporation component is indeed dominant. The procedure followed in the work of Ritter et al. (156), is to use a fusion–evaporation code and normalize the results of the two different calculations to the experimental data. It is worth noting here that this kind of calculations differs from the fusion–evaporation calculations for heavier nuclei, since in that case a continuum

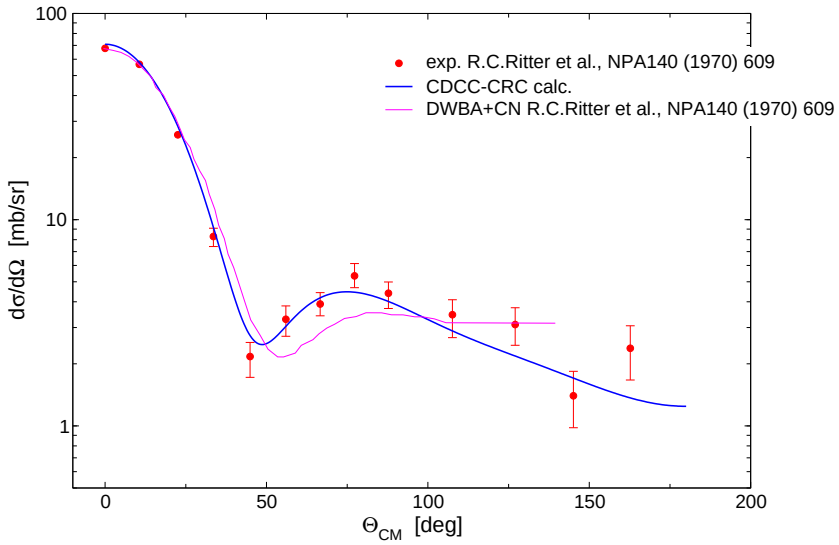

Figure 5.9: Test of the CDCC-CRC calculations - The experimental data for the ^{14}N(d,p) reaction are compared to two different theoretical models, namely a DWBA and a CDCC-CRC calculation.

parametrization of the level density of the compound nucleus can be used. In case of lighter nuclei this parametrization is not suitable and discrete levels have to be considered. These calculations were used to investigate the structure of similar light nuclei in the past, with Hauser-Feshbach (160, 161) codes such as MANDY (162), that are quite difficult nowadays to recover and use properly. The ratio p_{fe} of the fusion–evaporation channel with respect to the nucleon–transfer is hard to get from calculations or from the literature, and in our case we decided to leave it as a free parameter. As we will see in the next section, the modeling of the fusion–evaporation part is not crucial, since the sensitive component to the "short" lifetime effects is the one related to the transfer process. The output of PACE4 calculations will be used to describe the fusion–evaporation part together with trial assumptions considering a gaussian energy distribution and isotropical emission in the center of mass.

Examples of calculated CDCC-CRC angular distributions in the center of mass for different levels in ^{15}O and ^{15}N , populated in the ^{14}N(d,n) and ^{14}N(d,p) reactions, are shown in Fig. 5.10.

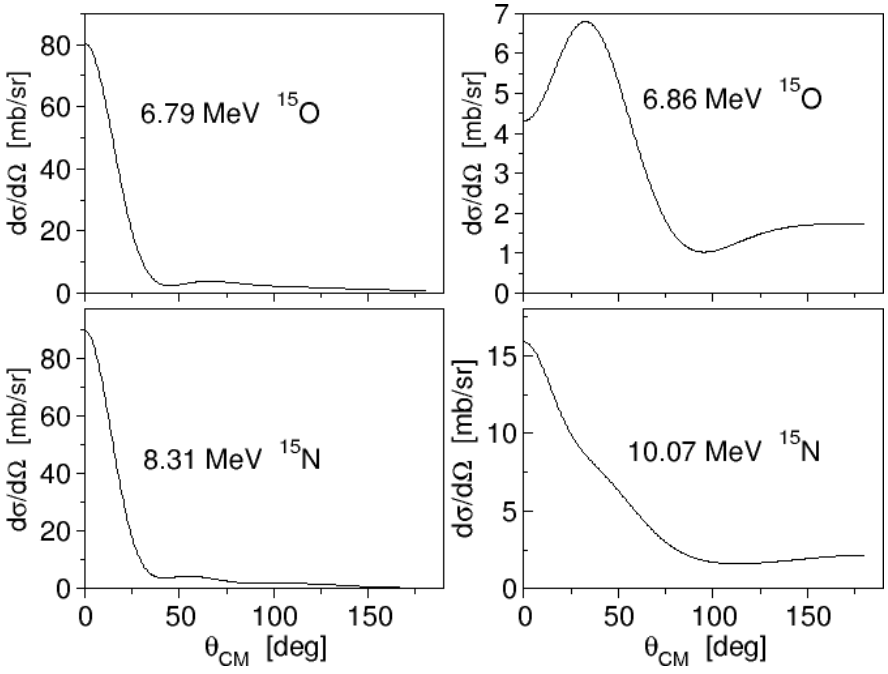

Figure 5.10: CDCC-CRC calculations for the nucleon–transfer process - Examples of calculated CDCC-CRC angular distributions in the center of mass for the levels of interest in ^{15}O and ^{15}N , populated in the ^{14}N(d,n) and ^{14}N(d,p) reactions

5.2 Lineshape analysis

The χ^2 between the experimental and simulated spectra can be evaluated with Eqn. 5.1 for each "θ–slice" selected after the tracking procedure (see Fig. 3.24). The limits of the fit region depend on the θ angle, since the energy of the peaks changes according to the Doppler formula. The number of points in the fit region, $\mathcal{N}$, was typically of the order of few hundreds channels. The reduced χ^2, $\tilde{\chi^2}$, is obtained by dividing Eqn. 5.1 by the number of degrees of freedom, considered as $\mathcal{N} - 1 - \mathcal{P}$, where $\mathcal{P}$ is the number of parameters to be extracted from the fit. In the $\tilde{\chi^2}$ curves that will be shown in the following, $\mathcal{P} = 3$ free parameters were extracted by looking for the minimum χ^2, namely the lifetime τ of the level, the fraction p_{fe} of fusion–evaporation, relative to the total cross–section, and the normalization of the spectra at the different angles.

The main difference with respect to a "traditional" fit procedure is that here the "theoretical" function (the simulated data) is not an analytical expression of the parameters. As a matter of fact, given the time it takes to produce the simulated spectra, and the operations that need to be performed on them, it was only feasible to produce simulated spectra for a limited number of lifetimes. Therefore, it was not possible to use or adapt the "traditional" well–known procedures for χ^2 minimization (such as MINUIT (163)), found in analysis packages such as `root`. Therefore we decided to build our own routine, in the framework of the automatic procedures described above for the construction of the spectra. In this way we could evaluate all the information relevant to the χ^2 and prepare output text files that could be read out by `root` macros which allow to plot any useful information, such as correlations and lineshapes.

In the following sections, the obtained results will be discussed separately for each level for which we could measure the lifetime, namely the 8.31 MeV and the 10.06 MeV states in ^{15}N and the 6.79 MeV state in ^{15}O . The previously measured values for the levels in ^{15}N (reported in Tab. 2.1) were used to check and validate our analysis method, before applying it to the ^{15}O case.

5.2.1 The lifetime of the 8.31 MeV state in ^{15}N

The lifetime of the 8.31 MeV level has been determined in a resonance fluorescence experiment and a DSAM measurement ((47, 48)). The obtained values, reported in

Tab. 2.1, are (1.7±1.1) fs and an upper limit at 16 fs, respectively. Now we will report our result for this level. This may be taken as a test of the capability of our system.

The reduced χ^2 values for the 8.31 MeV line in ^{15}N are shown in Figs. 5.11 and 5.12 as a function respectively of the lifetime and of the fraction p_{fe} of fusion–evaporation. All the θ slices having sufficient statistics are considered and fitted simultaneously.

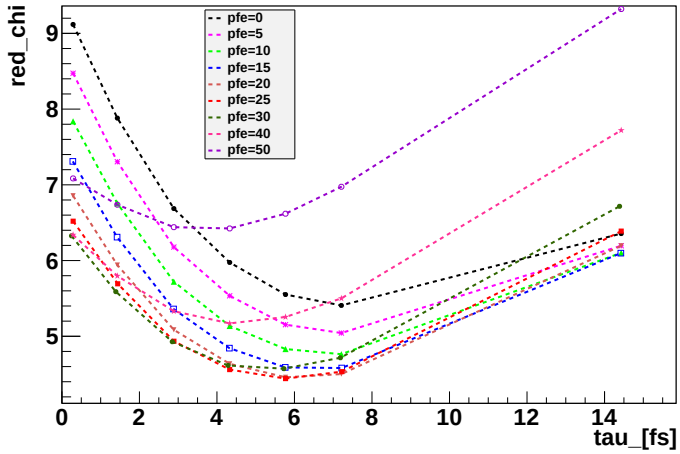

Figure 5.11: Reduced χ^2 vs τ for the 8.31 MeV level in ^{15}N - Reduced χ^2 values as a function of the lifetime for the 8.31 MeV level in ^{15}N. The curves corresponding to different (fixed) fractions of fusion–evaporation are shown in different colors.

Two considerations stand out from the reported trends:

- the reduced χ^2 as a function of the lifetime τ and p_{fe} have clear minima;
- these minima (τ ≈6 fs and p$_{fe}$ ≈25%) are almost independent from the fusion–evaporation fraction (with p_{fe} = 15-30), see Fig. 5.11, and from τ (in the ≈4.3–7.2 fs interval), see Fig. 5.12;
- the minimum $\tilde{\chi^2}$ is not approaching 1, as one would expect for gaussian distributions and proper treatment of the used model and the errors.

In Figs. 5.13 and 5.14 the spectrum measured at 160° is compared with the peak lineshape simulated for τ = 5.8 fs and p$_{fe}$=25% (red spectrum) and for p$_{fe}$ and τ, respectively, away from the minimum. The sensitivity of the lineshape to those parameters is evident from these figures.

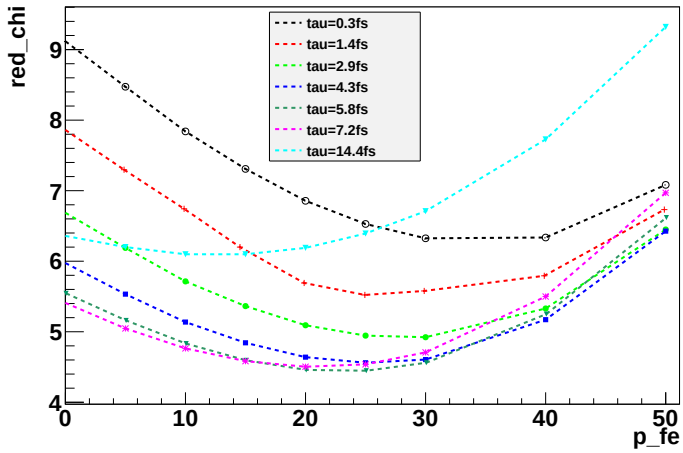

Figure 5.12: Reduced χ^2 vs p_{fe} for the 8.31 MeV level in ^{15}N - Reduced χ^2 as a function of the fusion–evaporation probability for the 8.31 MeV level in ^{15}N . The curves corresponding to different (fixed) lifetimes are shown in different colors.

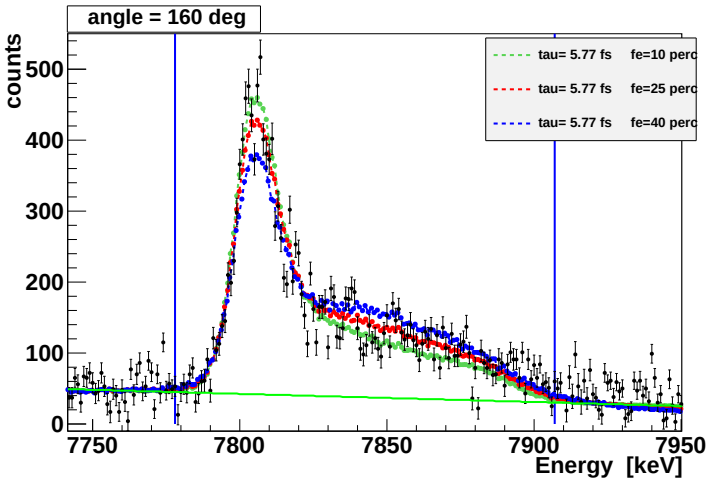

Figure 5.13: Lineshape of the 8312 keV level in ^{15}N for different p_{fe} - Experimental spectrum measured at 160°, compared with the lineshapes simulated for $\tau \approx 6$ fs –the minimum in the curves reported in Fig. 5.11– and p_{fe}=10, 25 and 40%. From Fig. 5.12 we can see that the minimum in the χ^2 curves is reached for p_{fe}=25%.

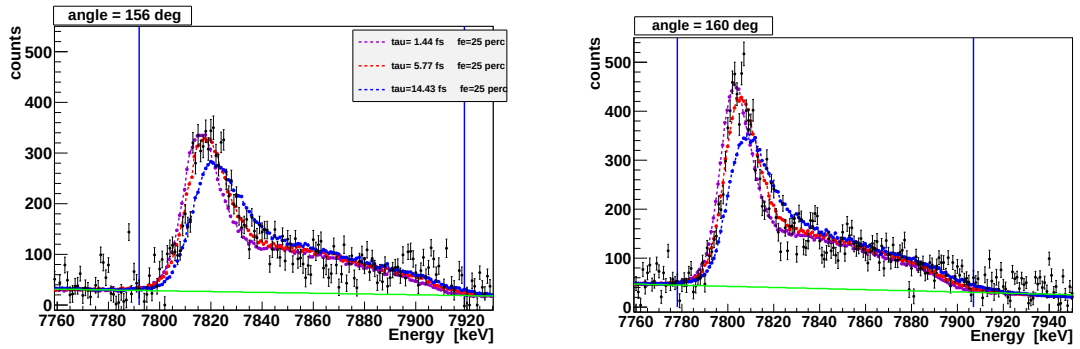

Figure 5.14: Lineshape of the 8312 keV level in ^{15}N for different τ - Experimental spectrum measured at 160° and corresponding simulated lineshapes for p_{fe}=25% –the minimum in the curves reported in Fig. 5.12– and different lifetime values. The "optimal" value is reported in red, corresponding to the minimum of the curves reported in Fig. 5.11.

In Fig. 5.15 the χ^2 curves (not reduced χ^2) are reported independently for the different angles. Ideally it would be nice to extract a value from each angle (possibly avoiding the ones with less statistics) and make an average. As discussed in e.g. (164), the statistical errors should be determined by the value of the parameter that correspond to an increase in the χ^2 by 3.2 (assuming 3 free parameters).

Evidently in the complex case we are treating, we are neglecting some important degrees of freedom/parameters, like e.g. the indetermination and error on the angle, that has to account for the non uniform distribution of the PSA hits, leading to wrong assignment of the first interaction point in the tracking. Given the complexity of the statistical treatment and the amount of parameters that are difficult to control, one can try, in our case, to exploit the parabolic trend of the chi square curves to obtain the statistical error in a self–consistent way. The background and details of this statistical treatment are reported in (165). One should then repeat the measurement "many times" for the distribution of the experimental points inside the errors to be gaussian. One can mimic this effect by analysing artificial spectra generated starting from the experimental one and randomly distributing the measured channel-values according to a gassian distribution with a standard deviation equals to their error bar. This is the idea at the basis of the *Monte Carlo sampling* error estimations (see (165) and references therein).

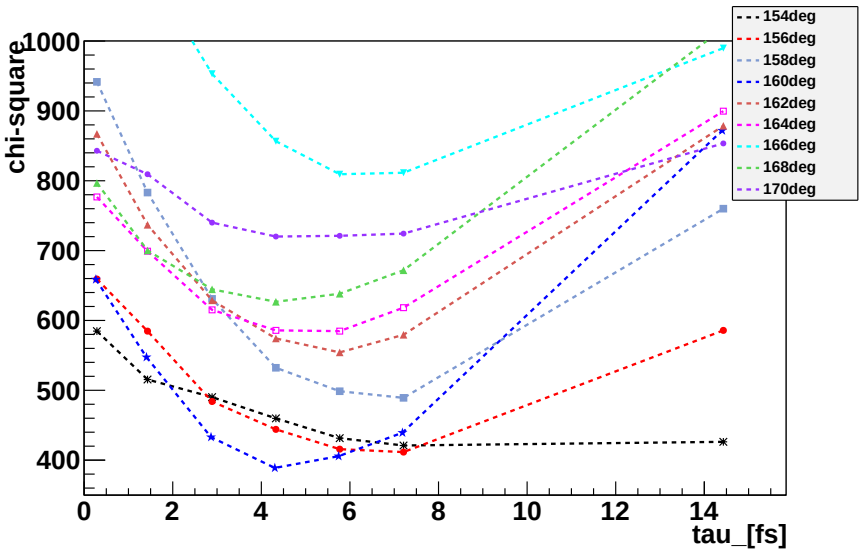

Figure 5.15: Reduced χ^2 vs τ for different θ angles - Reduced χ^2 as a function of the lifetime, obtained from the independent analyses of the spectra at the different angles.

From an evaluation of this procedure the obtained lifetime values and the relative errors for the different angles are reported in Tab. 5.16 and the corresponding figure.

Excluding the last point affected by low statistics, the weighted average of these values is (6.11±0.12) fs. Clearly, the error estimated in this way contains only the contribution of the measured statistics and therefore is just an absolute lower limit. In fact, the distribution of the individual values around the average has a standard deviation of 0.94, which implies an error of $\sigma/\sqrt{N-1}$=0.36 for the average value (as reported in Fig. 5.16). The discrepancy between the two error estimates is an indication of problems in modelling the data or in the data themselves (e.g. incorrect angle assignments by the PSA+Tracking procedure). This discrepancy and the fact that the reduced chisquare is much larger than 1 are an indication that the errors used in the fitting procedure, derived by simple propagation, are underestimated. Instead of increasing them (in a somehow arbitrary way) we prefer to account for the problem by quoting the standard deviation of the the distribution (0.94) instead of the statistical ones (0.11 or 0.35) as global error of the measured lifetime.

Our estimate on the lifetime of this level, (6.1±1.0) fs, is consistent with the upper limit reported in (47), but disagrees by four standard deviations from the value mea-

θ [deg]	τ [fs]
170	5.8±0.5
168	4.6±0.4
166	7.3±0.3
164	6.0±0.5
162	6.1±0.3
160	5.1±0.3
158	6.7±0.2
156	7.2±0.5
154	9.3±0.7

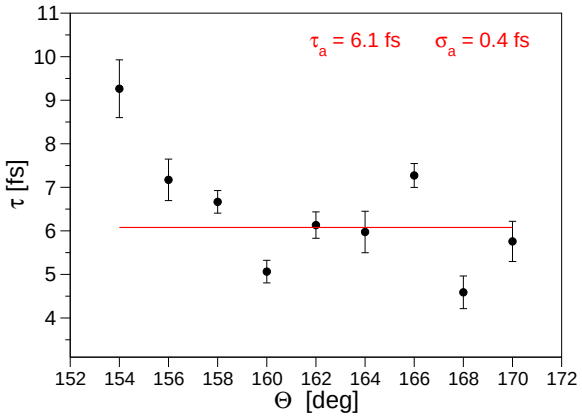

Figure 5.16: Lifetime of the 8.3 MeV level in ^{15}N - Self–consistent estimation of the statistical uncertainties on the lifetime values obtained at the different angles (166) in the case of the 8.31 MeV state in ^{15}N. The weighted average is (6.11±0.12) fs (not considering the value for θ=154°.

sured in (48). From the spectra displayed in Fig. 5.14 one can see that a lifetime of 1.4 fs (close to the one evaluated in the considered reference) is not suitable for reproducing our data.

5.2.2 The lifetime of the 10.06 MeV state in ^{15}N

For the 10.06 MeV state in ^{15}N a precise value of (0.104±0.007) fs is given in (47), on the basis of a resonance fluorescence experiment. In Fig. 5.17 the $\tilde{\chi}^2$ derived in our analysis are reported. The overall trend and statistical considerations are similar to the analysis described above. One can thus determine a minimum from these curves and consider the same relative statistical error as obtained for the 8.31 MeV level, i.e. 16%. We can then derive (5.0±0.8) fs as our estimate of the lifetime. This value strongly disagree from the estimate from the resonance fluorescence method, i.e. (0.104±0.007) fs (47). We don't see a way to reconcile our data with such a value because just by a simple visual comparison (Fig. 5.18) it is clear that a lifetime of 0.1 fs is incompatible with our spectra.

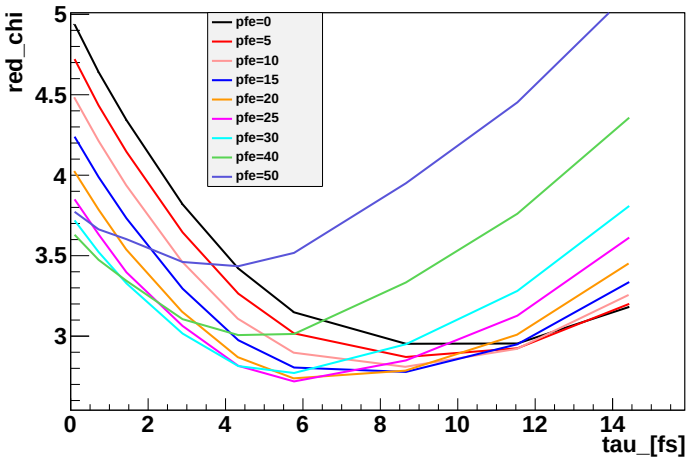

Figure 5.17: Reduced χ^2 vs τ for the 10.06 MeV level in ^{15}N - The $\tilde{\chi}^2$ curves corresponding to different (fixed) fractions of fusion–evaporation are shown.

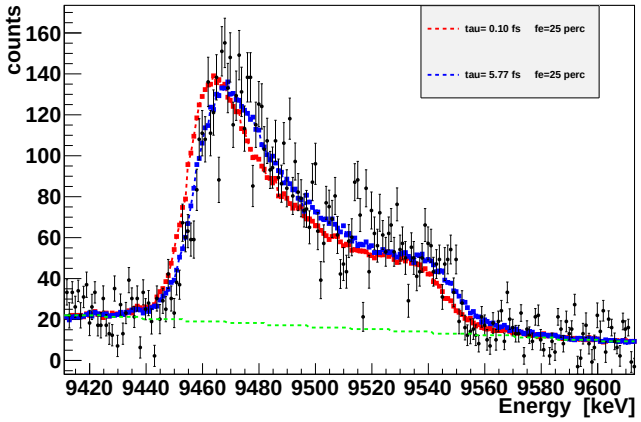

Figure 5.18: Lineshape analysis for the 10.06 MeV level in ^{15}N - Comparison of the experimental and simulated spectra for the 10.06 MeV level in ^{15}N at 160°.

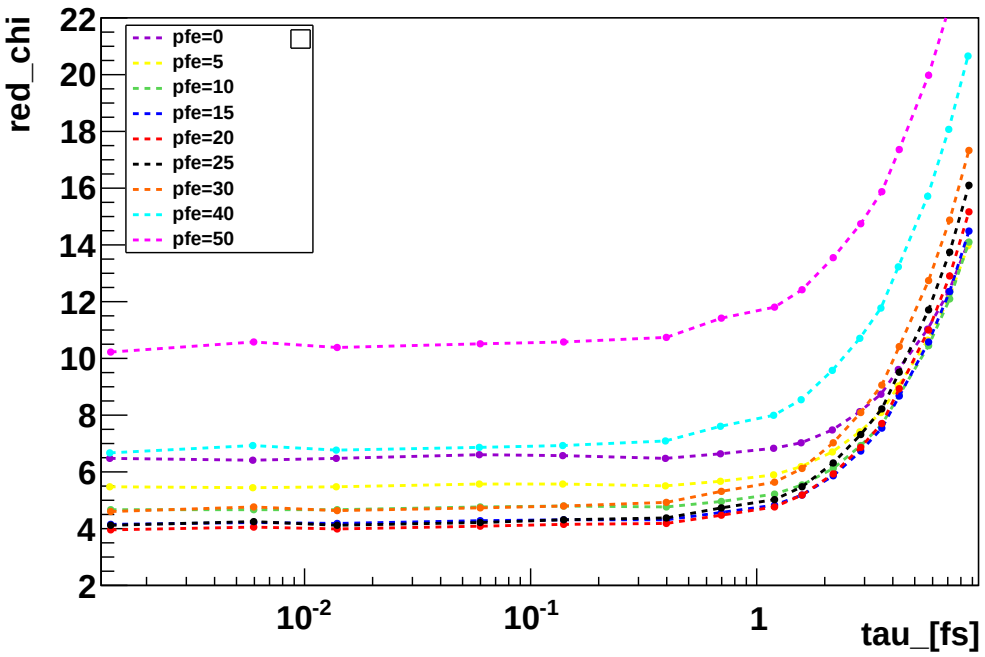

Figure 5.19: Reduced χ^2 vs τ for the 6792 keV state in ^{15}O - $\tilde{\chi^2}$ curves as a function of the lifetime, corresponding to different fractions of fusion–evaporation. The x (lifetime) axis is shown in logarithmic, in order to better recognise the flattering of the curves towards "0" fs lifetime.

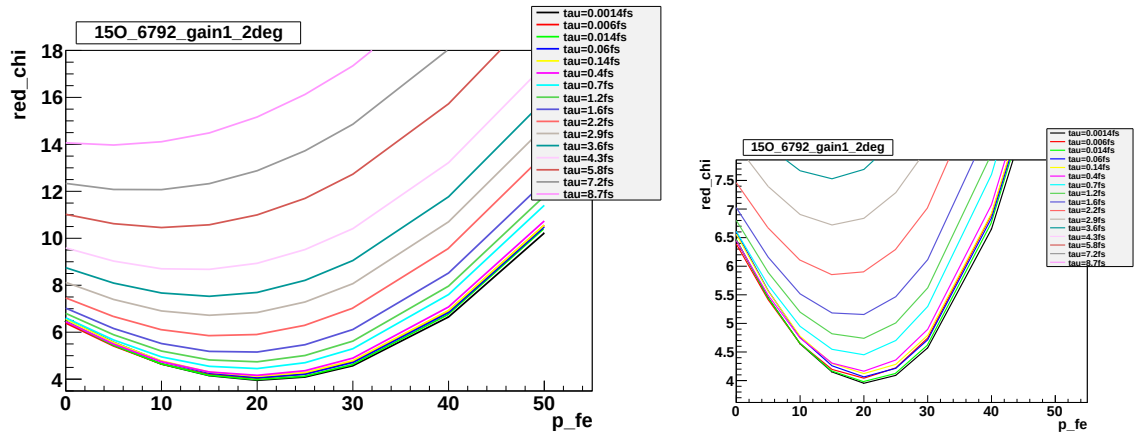

Figure 5.20: Reduced χ^2 vs p_{fe} for the 6792 keV state in ^{15}O - Reduced χ^2 curves as a function of the fraction of fusion–evaporation, corresponding to different lifetimes. The panel on the right–hand side is a zoom of the region around the minimum from the plot on the left.

5.2.3 The lifetime of the 6.79 MeV state in ^{15}O

In Fig. 5.19 the reduced chi–square as a function of the lifetime is reported for the 6.79 MeV γ–ray transition. The different fractions of fusion–evaporation all indicate that below a certain value for the lifetime the χ^2 flattens without producing a detectable minimum. It is then clear that our experiment can only produce an upper limit for the lifetime of this state. On the other side, Fig. 5.20 shows that, as for the case of ^{15}N,the fraction of fusion-evaporation does not depend sensitively on the value of the lifetime and minimizes always at ≈20%. Given the quality of the χ^2 curves and the fact that the value of $\tilde{\chi^2}$ is, like in the previous cases, quite larger than unity, it seems impossible to derive the limit in a numerically sound way. There are actually only two consideration we can make:

- how much do the simulated spectra differ from each other in this lifetime range;
- at the point they start being different, is our statistics sufficient to produce a sensible change in the χ^2?

To answer the first question we have calculated the χ^2 of the simulated spectra with one of them, in turn, replacing $Exp(k)$ in Eqn. 5.1. The obtained distributions have been fitted with a second degree curve (excluding, of course, the reference value for which χ^2=0 by construction), as shown in Fig. 5.21. It is clear that the distributions develop a minimum only for $\tau \lesssim 1$ fs, while for lower lifetimes they flatten off very similarly to what happens in Fig. 5.19. For this reason and in consideration of the fact that for the ^{15}N cases we have given 1 fs as reasonable error, we fix the upper limit of the lifetime of the 6.79 MeV state in ^{15}O to 1 fs.

In Fig. 5.22 the reduced χ^2 as a function of the lifetime, selected from Fig. 5.19 for p_{fe}=20%, is reported, with indicated the limit deduced from our analysis. The lineshapes simulated for p_{fe}=20% and two different lifetimes, smaller and larger than the considered limit, are compared with the experimental spectra at different angles in Fig. 5.23. These figures show a quite good agreement between simulated and experimental spectrum, at the different angles.

The deduced upper limit on the lifetime of the 6.79 MeV state in ^{15}O, $\tau < 1$fs – corresponding to a width $\Gamma > 0.66$ keV, is consistent with the values estimated by the

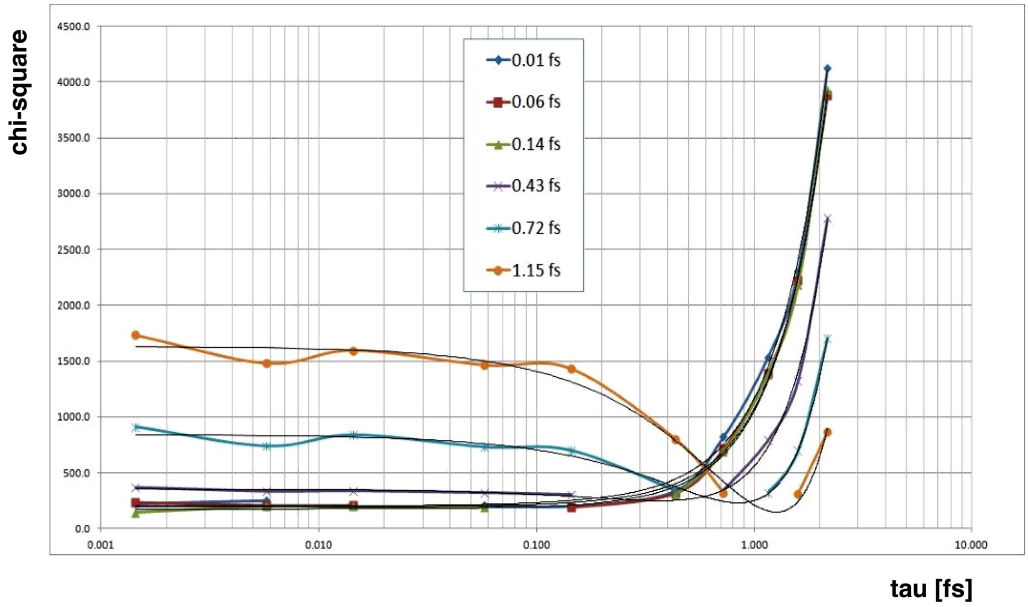

Figure 5.21: Sensitivity of the simulated lineshapes to chnges of the lifetime in the fs region - χ^2 as a function of the lifetime taking as a reference a simulated spectrum, obtained with a given lifetime. In correspondence of this value, the χ^2 is null by construction and thus not reported in the figure. In analogy to the plots reported in Fig. **??**, the x (lifetime) axis is in logarithmic scale.

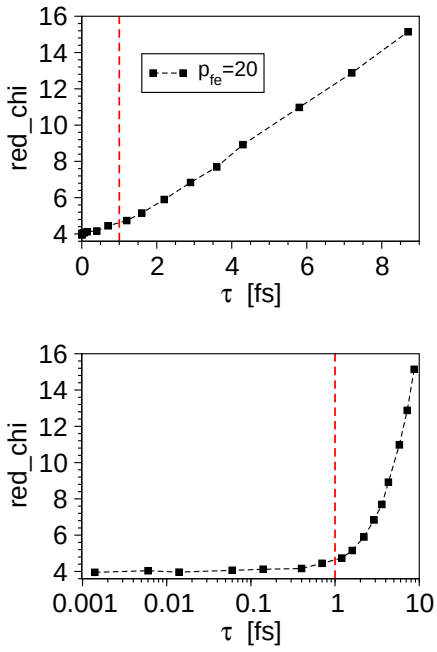

Figure 5.22: The lifetime of the 6.79 MeV state in ^{15}O - Reduced χ^2 curves as a function of τ–in linear (upper panel) and logarithmic (lower panel) scale– for $p_{fe} = 20\%$. The limit of 1 fs, deduced from our analysis is indicated with a red line.

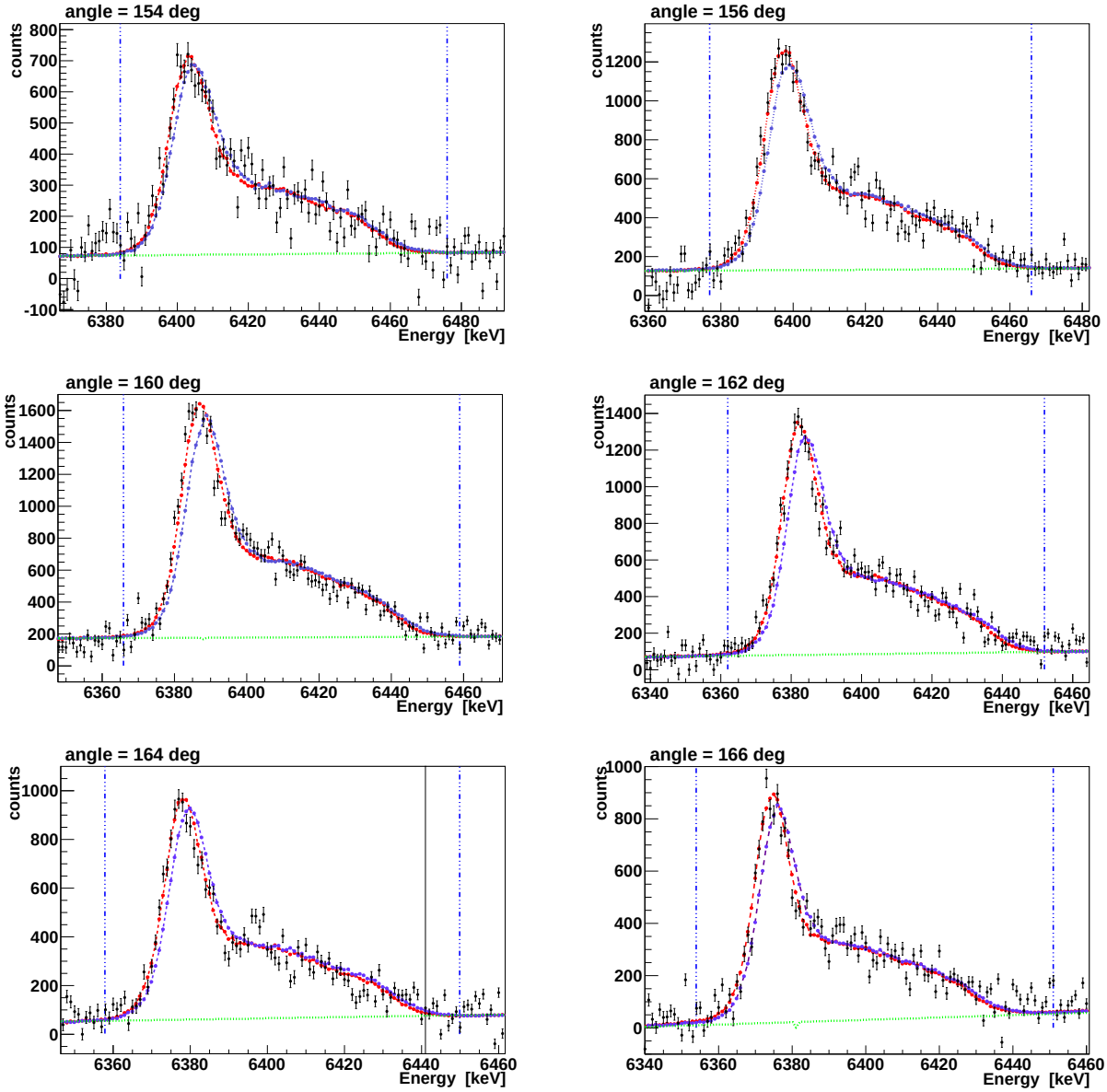

Figure 5.23: Lineshapes of the 6.79 MeV γ–ray in ^{15}O - Spectra mesured at different angles for the 6.79 MeV gamma line, compared with the lineshapes simulated for p_{fe}=20% and two different lifetimes, $\tau = 0.1$ fs (red spectrum) and 2.9 fs (violet).

R–matrix fit used for the extrapolation of the experimental S–factor to low energies. These values are reported in Chapter 1, Tab.1.1, together with the results of direct measurements as the one described in this Thesis. Our new direct evaluation of this upper limit brings additional support to the previously reported sub–femtosecond lifetime determinations.

6

Conclusions

A new experimental evidence for a sub–femtosecond lifetime of the 6.79 MeV state in ^{15}O has been obtained. The accurate determination of the lifetime of this level is of paramount importance in the extrapolation of the astrophysical S–factor of the ^{14}N(p,γ)^{15}O reaction at stellar energies. This reaction is the "bottle–neck" in the CNO–cycle and its rate influences important astrophysical phenomena and open questions, such as the age of the globular clusters and the problem of the homogeneity of the metal content across the solar volume (*solar composition problem*). From the analysis carried out in this thesis work, a limit of 1 fs for the lifetime of the 6.79 MeV state in ^{15}O is deduced, corresponding to $\Gamma > 0.66$ keV, is consistent with the R–matrix fit estimations, available in the literature.

The DSAM constitutes the only tool to measure directly this lifetime. In this Thesis the complex problem of experimentally accessing such short lifetimes with this technique has been faced and its main issues reviewed, in the framework of the analysis of a new dedicated experiment.

The 6.79 MeV level in ^{15}O and excited levels in ^{15}N were populated in the d(^{14}N,n)^{15}O reaction at 32 MeV. The emitted γ–rays were detected with the AGATA Demonstrator, during its first experimental campaign, at the Legnaro National Laboratories. By the means of the implementation of the novel concepts of pulse shape analysis and gamma–ray tracking, the first interaction points of the detected gamma–rays could be sorted in angular "slices" of 2o (with respect to the beam axis). The Doppler shift attenuated lineshapes in those spectra have been analysed by comparison with detailed Monte Carlo simulation of the reaction process and γ–ray emission and detection. Given the

complexity and innovation of the system, the data replay and analysis procedures have been discussed in detail.

The lifetime of the 8.3 MeV state in ^{15}N has been used as a test of the analysis method developed during the thesis work. In this case a lifetime of (6.0±1.0) fs was determined and compared with the values reported in the literature. The statistical errors on the values obtained for different angles were evaluated with a Monte Carlo sampling statistical analysis. It became evident that the statistical treatment of the DSAM data obtained with the AGATA Demonstrator array is complex, due to the not well defined degree of correlation of the parameters involved, in particular the ones related to the pulse shape analysis and tracking. More effort is required to completely understand the nature and the entity of all the contributions to the statistical errors.

Bibliography

[1] C. Iliadis. *Nuclear physics of stars*. Physics textbook. Wiley-VCH, 2007. 1, 2, 6, 7

[2] D.D. Clayton. *Principles of Stellar Evolution and Nuclear Synthesis*. Physics textbook. McGraw-Hill, 1968. 1, 4

[3] **Australia Telescope. Outreach and Education**, 2012. 2

[4] E.G. Adelberger et al. **Solar fusion cross sections. II. The *pp* chain and CNO cycles**. *Review of Modern Physics*, **83**:195, Apr 2011. 3, 5, 6, 7, 9, 12, 14

[5] C. Broggini et al. **LUNA: Nuclear Astrophysics Deep Underground**. *Annual Review of Nuclear and Particle Science*, **60**:53, 2010. 4, 11

[6] J.N. Bahcall. *Neutrino Astrophysics*. Cambridge University Press, 1989. 5, 6

[7] C.E. Rolfs and W.S. Rodney. *Cauldrons in the Cosmos*. Physics textbook. University of Chicago Press, 2005. 5

[8] A.M. Lane and R.G. Thomas. *Review of Modern Physics*, **30**:257, 1958. 6

[9] C.R. Brune. **Alternative parametrization of R–matrix theory**. *Physical Review C*, **66**:044611, 2002. 6

[10] R. Jimenez. **Globular clusterages**. *Proceedings of the National Academy of Sciences*, **95**(1):13, 1998. 6

[11] J.N. Bahcall et al. **Helioseismological Implications of Recent Solar Abundance Determinations**. *The Astrophysical Journal*, **618**(2):1049, 2005. 7

[12] J.N. Bahcall and H.A. Bethe. **Solution of the solar–neutrino problem**. *Physical Review Letters*, **65**:2233–2235, 1990. 6

[13] C. Pena-Garay and A.M. Serenelli. **Solar neutrinos and the solar composition problem**. *arXiv: 0811.2424v1 [astro-ph]*, 2008. 7, 11

[14] A. M. Serenelli et al. **New solar composition: the problem with solar models revisited**. *Astrophysical Journal Letters*, **705**:L123, 2009. 7

[15] John N. Bahcall et al. **Solar Models: Current Epoch and Time Dependences, Neutrinos, and Helioseismological Properties**. *The Astrophysical Journal*, **555**(2):990, 2001. 7

[16] M. Asplund et al. **Cosmic Abundances as Records of Stellar Evolution and Nucleosynthesis**. In T. G. Barnes and F. N. Bash, editors, *Conference Proceedings Vol. 336*, page 25. Astronomical Society of the Pacific, 2005. asplund.pdf. 7

[17] W. C. Haxton and A. M. Serenelli. **CN cycle solar neutrinos and the Sun's primordial core metallicity**. *Astrophysical Journal*, **687**:678, 2008. 7, 8

[18] C. Arpesella et al. **First real time detection of Be7 solar neutrinos by Borexino**. *Physical Review Letters*, **101**:091302, 2008. 8

[19] M. C. Chen et al. **The SNO Liquid Scintillator Project**. *Nuclear Physics B (Proceedings Supplements)*, **145**:65, 2005. 8

[20] **NASA Science: Science news**, 2009. http://www.nishina.riken.jp/Eng/index.html. 8

[21] U. Schröder et al. **Stellar reaction rate of ^{14}N(p,g)^{15}O and hydrogen burning in massive stars**. *Nuclear Physics A*, **467**(2):240 – 260, 1987. 9

[22] D. Bemmerer et al. **Low energy measurement of the ^{14}N(p,g)^{15}O total cross section at the LUNA underground facility**. *Nuclear Physics A*, **779**:297–317, 2006. 9

BIBLIOGRAPHY

[23] A. Formicola et al. **Astrophysical S–factor of ^{14}N(p,g)^{15}O**. *Physics Letters B*, **591**(1-2):61–68, 2004. 9, 10, 12

[24] G. Imbriani et al. **S–factor of ^{14}N(p,g)^{15}O at astrophysical energies**. *The European Physical Journal A - Hadrons and Nuclei*, **25**:455–466, 2005. 9, 10

[25] A. Lemut et al. **First measurement of the ^{14}N(p,g)^{15}O cross section down to 70 keV**. *Physics Letters B*, **634**(56):483 – 487, 2006. 9, 10

[26] R. Runkle et al. **Direct Measurement of the ^{14}N(p,g)^{15}O S factor**. *Physical Review Letters*, **94**:082503, 2005. 9, 12

[27] M. Marta et al. **The ^{14}N(p,g)^{15}O reaction studied with a composite germanium detector**. *Physical Review C*, **78**:022802(R), 2008. 9, 10, 11, 12

[28] M. Marta et al. **The ^{14}N(p,g)^{15}O reaction studied with a composite germanium detector**. *Physical Review C*, **83**:045804, 2011. 9

[29] M. Marta. **Experimental study of the ^{14}N(p,g)^{15}O reaction at high and low energies**. *Progress in Particle and Nuclear Physics*, **66**:303, 2011. 9

[30] C. Angulo et al. **A compilation of charged-particle induced thermonuclear reaction rates**. *Nuclear Physics A*, **656**(1):3, 1999. 10

[31] S. Degl'Innocenti et al. **The ^{14}N(p,γ)^{15}O reaction, solar neutrinos and the age of the globular clusters**. *Physics Letters B*, **590**:13, 2004. 10

[32] J.N. Bahcall and M.H. Pinsonneault. **What Do We (Not) Know Theoretically about Solar Neutrino Fluxes?** *Physical Review Letters*, **92**:121301, Mar 2004. 10

[33] G. Imbriani et al. **The bottleneck of CNO burning and the age of Globular Clusters**. *Astronomy & Astrophysics*, **420**(2):625, 2004. 11

[34] H. P. Trautvetter et al. **Ground state capture in ^{14}N(p,g)^{15}O studied above the 259 keV resonance at LUNA**. *Journal of Physics G*, **35**:014019, 2008. 11, 12

[35] M. Marta. **R–matrix fit for the ground state transition in the S–factor for the ^{14}N(p,γ)^{15}O reaction**. *private communication*, 2011. 12

[36] W. Gill et al. **Lifetime measurements in mass–15 nuclei**. *Nuclear Physics A*, **121**:209, 1968. 12, 13, 14, 55

[37] P.F. Bertone et al. **Lifetime of the 6793-keV State in ^{15}O**. *Physical Review Letters*, **87**:152501, 2001. 12, 13, 14

[38] K. Yamada et al. **E1 strength of the subthreshold $3/2^+$ state in ^{15}O studied by Coulomb excitation**. *Physics Letters B*, **579**:265, 2004. 12, 28

[39] D. Schuermann et al. **Lifetime measurement of the 6792 keV state in ^{15}O, important for the astrophysical S–factor extrapolation in ^{14}N(p,g)^{15}O**. *Physical Review C*, **77**:055803, 2008. 12, 13, 14

[40] **RIKEN Nishina center for Accelerator based Science**, 2013. 12

[41] **National Nuclear Data Center**, 2011. 14, 19, 56, 70, 85

[42] **TRIUMF: Canadian's national laboratories for particle and nuclear physics**, 2012. 15

[43] N. Galinsky. **TRIUMF: ISAC Forum Minutes**, 2010. 15

[44] C. Michelagnoli et al. **Lifetime measurement of the 6.79 MeV state in ^{15}O with the AGATA Demonstrator**. In S. Kubono, T. Hayakawa, T. Kajino, H. Miyatake, T. Motobayashi, and K. Nomoto, editors, *Origin of Matter and Evolution of Galaxies XII, Conference Proceedings in press*. AIP Conference Proceedings, Volume 1484, 2011. 15, 53

[45] A. Bohr and B.R. Mottelson. *Nuclear Structure*, **1**. World Scientific, 1998. 17

[46] M.A. Preston. *Structure of the Nucleus*. 17, 18

[47] R. Moreh et al. **Gamma–ray widths in ^{15}N**. *Physical Review C*, **23**:988–991, 1981. 19, 111, 115, 116

[48] J.C. Kim, H.S. Caplan, and J.C. Bergstrom. **Low lying octupole excitations in ^{15}N**. *Nuclear Physics A*, **246**(2):282 – 292, 1975. 19, 111, 116

[49] J. Keinonen, M. Bister, and A. Anttila. **Lifetimes of bound states in ^{15}O**. *Nuclear Physics A*, **286**(3):505 – 511, 1977. 19

[50] D. E. Alburger and E. K. Warburton. **Excitation Energy and Lifetime of the O^{15} 7276-keV State**. *Physical Review*, **152**:914–917, Dec 1966. 19

[51] F. Ajzenberg-Selove. **Energy levels of light nuclei A = 13-15**. *Nuclear Physics A*, **523**(1):1–196, 1991. 19

[52] S. Raman, E. T. Jurney, J. W. Starner, A. Kuronen, J. Keinonen, K. Nordlund, and D. J. Millener. **Lifetimes in ^{15}N from gamma–ray line shapes produced in the ^{2}H(^{14}N,$p\gamma$) and ^{14}N(thermal n,γ) reactions**. *Physical Review C*, **50**:682–697, Aug 1994. 19

[53] P.J. Nolan et al. **The measurement of the lifetime of excited nuclear states**. *Reports on Progress in Physics*, **45**, 1979. 18

[54] E.K. Warburton and A.Z. Schwarzschild. **The Measurement of Short Nuclear Lifetimes**. *Annual Review of Nuclear Science*, **18**, 1968. 19, 22

[55] A. Dewald, S. Harissopulos, and P. von Brentano. **The differential plunger and the differential decay curve method for the analysis of recoil distance Doppler–shift data**. *Zeitschrift für Physik A Hadrons and Nuclei*, **334**:163–175, 1989. 10.1007/BF01294217. 20, 21, 22

[56] T.K. Alexander and A. Bell. **A target chamber for recoil-distance lifetime measurements**. *Nuclear Instruments and Methods*, **81**(1):22 – 26, 1970. 21

[57] G. Boehm, A. Dewald, P. Petkov, and P. von Brentano. **The differential decay curve method for the analysis of Doppler shift timing experiments**. *Nuclear Instruments and Methods in Physics Research Section A*, **329**(1-2):248–261, 1993. 21

[58] P. Petkov, D. Tonev, A. Dewald, and P. von Brentano. **Lifetime analysis using the Doppler-shift attenuation method with a gate on depopulating transition**. *Nuclear Instruments and Methods in Physics Research Section A*, **488**:555–561, 2002. 23

[59] F. Brandolini and R.V. Ribas. **Doppler shift attenuation method analysis with the narrow gate on transitions below procedure**. *Nuclear Instruments and Methods in Physics Research Section A*, **417**(1):150–157, 1998. 23, 25

[60] F. Brandolini, N.H. Medina, S.M. Lenzi, D.R. Napoli, A. Poves, R.V. Ribas, J. Sanchez-Solano, C.A. Ur, M. De Poli, N. Marginean, D. Bazzacco, J.A. Cameron, G. de Angelis, A. Gadea, R. Menegazzo, and C. Rossi-Alvarez. **Lifetimes in the middle of 1f7/2 shell: cross-conjugated nuclei ^{47}V and ^{49}Cr**. *Nuclear Physics A*, **693**(3-4):517–532, 2001. 23, 24

[61] J. C. Bacelar, R. M. Diamond, E. M. Beck, M. A. Deleplanque, J. Draper, and F. S. Stephens. **Line-shape analysis of high spin states: Collectivity in ^{166}Yb**. *Physical Review C*, **35**:1170–1173, Mar 1987. 23, 24

[62] A.E. Blaugrund. **Notes on Doppler-shift lifetime measurements**. *Nuclear Physics*, **88**(3):501 – 512, 1966. 24

[63] W.M. Currie. **A Monte Carlo programme for Doppler shift analysis**. *Nuclear Instruments and Methods*, **73**(2):173 – 185, 1969. 24, 89

[64] J.F. Ziegler et al. *The Stopping and Range of Ions in Solids*, **1**. Pergamon Press, 1985. 27, 56

[65] L.C.Northcliffe e R.F.Schilling. *Nuclear Data Tables A*, **7**:233, 1970. 27

[66] J.E.Ziegler e W.K.Chu. *Atomic and Nuclear Data Tables*, **13**:463, 1974. 27

[67] D.Ward. *AECL Rep.*, page 5313, 1976. 27, 30, 31

[68] V.Nielsen e M.Scharff J.Lindhard. *Mat. Fys. Medd., Dan. Vid. Selsk.*, **36**:no 10, 1968. 27

[69] GRETA Steering Committee. **Proposal for GRETINA**. *Lawrence Berkeley National Laboratory*, 2003. 30, 31, 32, 45

[70] H. Morinaga and P.C. Gugelot. **Gamma rays following (α, xn) reactions**. *Nuclear Physics*, **46**:210 – 224, 1963. 30, 31

[71] H. Ryde, S.A. Hjorth, D. Barnoud, A. Johnson, G.B. Hagemann, and B. Herskind. **Influence of nuclear rotation on the moment of inertia in ^{160}Er and ^{156}Dy**. *Nuclear Physics A*, **207**(3):513 – 526, 1973. 30, 31

[72] M.A. Riley, J. Simpson, J.F. Sharpey-Schafer, J.R. Cresswell, H.W. Cranmer-Gordon, P.D. Forsyth, D. Howe, A.H. Nelson, P.J. Nolan, P.J. Smith, N.J. Ward, J.C. Lisle, E. Paul, and P.M. Walker. **Near yrast discrete line gamma–ray spectroscopy in ^{156}Dy up to spin 40$\hbar$**. *Nuclear Physics A*, **486**(2):456 – 492, 1988. 30, 31

[73] F.G. Kondev et al. **Spin approx 60$\hbar$ in ^{156}Dy: competition between collective and terminating structures at very high–spin**. *Physics Letters B*, **437**:35, 1998. 30, 31

[74] D. Bazzacco. *Proceedings of Conference on the Physics from Large γ–ray detector arrays*, page 376, 1992. Chalk River, Ontario, Canada. 32

[75] C. Rossi Alvarez. **The GASP Array**. *Nuclear Physics News Europe*, **2**:10, 1993. 32

[76] C.W. Beausang, S.A. Forbes, P. Fallon, P.J. Nolan, P.J. Twin, J.N. Mo, J.C. Lisle, M.A. Bentley, J. Simpson, F.A. Beck, D. Curien, G. deFrance, G. Duchne, and D. Popescu. **Measurements on prototype Ge and BGO detectors for the Eurogam array**. *Nuclear Instruments and Methods in Physics Research Section A*, **313**(1-2):37 – 49, 1992. 32

[77] C. Rossi Alvarez. **The EUROBALL array**. *Nuovo Cimento A*, **111**:601, 1998. 32

[78] J. Simpson. **The EUROBALL Spectrometer**. *Zeitschrift für Physik A*, **358**:139, 1997. 32

[79] R. Diamond M. A. Deleplanque. **Gammasphere proposal**. *Lawrence Berkley National Laboratory Report*, **5202**. 32

[80] I. Y. Lee. **The GAMMASPHERE**. *Nuclear Physics A*, **520**:641–655, 1990. 32

[81] I.Y. Lee, M.A. Deleplanque, and K. Vetter. **Developments in large gamma–ray detector arrays**. *Report on Progress in Physics*, **66**, 2003. 32, 33

[82] J. Eberth and J. Simpson. **From Ge(Li) detectors to gamma-ray tracking arrays –50 years of gamma spectroscopy with germanium detectors**. *Report on Progress in Physics*, **60**:283, 2008. 32, 33

[83] P.J. Nolan and P.J. Twin. **Superdeformed shapes at high angular momentum**. *Annual Review of Nuclear and Particle Science*, **38**:533–562, 1988. 33

[84] A.M. Stefanini, L. Corradi, G. Maron, A. Pisent, M. Trotta, A.M. Vinodkumar, S. Beghini, G. Montagnoli, F. Scarlassara, G.F. Segato, A. De Rosa, G. Inglima, D. Pierroutsakou, M. Romoli, M. Sandoli, G. Pollarolo, and A. Latina. **The heavy-ion magnetic spectrometer PRISMA**. *Nuclear Physics A*, **701**(1-4):217–221, 2002. 5th International Conference on Radioactive Nuclear Beams. 33

[85] A. Gottardo et al. *Nuclear Physics A*, **805**:606, 2008. 33

[86] A. Gadea et al. **Conceptual design and infrastructure for the installation of the first AGATA sub–array at LNL**. *Nuclear Instruments and Methods in Physics Research Section A*, **654**(1):88, 2011. 33, 52, 55

[87] D. Mengoni et al. **TRACE Project: Progress on Digital Pulse Shape Analysis for Silicon Detectors**. *LNL Annual Report 2011*, page 58, 2012. 33

[88] **SPES Technical Design Report**. *INFN-LNL-223*, 2008. 34

[89] Th. Kroell and D. Bazzacco. **Simulation and analysis of pulse shapes from highly segmented HPGe detectors for the γ–ray tracking array MARS**. *Nuclear Instruments and Methods in Physics Research Section A*, **463**:227–249, 2001. 34, 37, 43

[90] D. Bazzacco. **Status of the AGATA project**. In A. Bracco and A. C. Kalfas, editors, *The labyrinth in nuclear structure, Conference Proceedings Vol. 701*, page 132. American Institute of Physics, 2003. 37

[91] G. Schmid et al. **A γ–ray tracking algorithm for the GRETA spectrometer**. *Nuclear Instruments and Methods in Physics Research Section A*, **430**(1):69, 1999. 37

[92] J. van der Marel and B. Cederwall. **Backtracking as a way to reconstruct Compton scattered gamma rays**. *Nuclear Instruments and Methods in Physics Research Section A*, **437**(2-3):538, 1999. 37

[93] D. Bazzacco. **MGT (Mars Gamma Tracking) code**. 2012. private communication. 37

[94] F. Recchia. *In–beam test and imaging capabilities of the AGATA prototype detector*. PhD thesis, University of Padova, January 2008. 38, 39

[95] G.F. Knoll. *Radiation detection and measurement*. Physics textbook. Wiley-VCH, 2010. 40, 44

[96] L. Nelson et al. **Characterisation of an AGATA symmetric prototype detector**. *Nuclear Instruments and Methods in Physics Research Section A*, **573**(12):153, 2007. Proceedings of the 7th International Conference on Position-Sensitive Detectors. PSD-7 7th International Conference on Position-Sensitive Detectors. 41

[97] T. M. Hoa and A. Korichi. **AGATA scanning status at Orsay**. 5th AGATA week, Orsay, 2007. 41

[98] B. Bruyneel. *Characterization of Segmented Large Volume, High Purity Germanium Detectors*. PhD thesis, University of Cologne, June 2006. 42, 43

[99] W. Blum et al. *Particle detection with drift chambers*. Particle acceleration and detection. Springer-Verlag Berlin Heidelberg, 2008. 42

[100] B. Bruyneel et al. **Crosstalk properties of 36-fold segmented symmetric hexagonal HPGe detectors**. *Nuclear Instruments and Methods in Physics Research Section A*, **599**(23):196, 2009. 43

[101] B. Bruyneel et al. **Characterization of large volume HPGe detectors. Part II: Experimental results**. *Nuclear Instruments and Methods in Physics Research Section A*, **569**(3):774, 2006. 43

[102] R. Venturelli et al. **Fold–dependent energy correction in segmented germanium detectors**. *LNL Annual Report 2002*, page 156, 2003. 43

[103] F. Recchia et al. **Position resolution of the prototype AGATA triple–cluster detector from an in–beam experiment**. *Nuclear Instruments and Methods in Physics Research Section A*, **604**(3):555, 2009. 43, 44

[104] P.-A. Söderstrom et al. **Interaction position resolution simulations and in–beam measurements of the AGATA HPGe detectors**. *Nuclear Instruments and Methods in Physics Research Section A*, **638**(1):96, 2011. 43, 85, 99

[105] R. Venturelli and D. Bazzacco. **Adaptive Grid Search as Pulse Shape Analysis Algorithm for g–Tracking and Results**. *LNL Annual Report 2004*, page 220, 2005. 43, 44

[106] B. Bruyneel. **Neutron damage and trapping effects**. 8th AGATA week, Lyon, 2010. 44, 45, 77

[107] B. Bruyneel et al. **Correction for neutron damage in AGATA detectors using Pulse Shape Analysis**. *submitted to EPJA*, 2012. 44, 45, 77

[108] D. Bazzacco. **Modern gamma tracking arrays**. 4th Summer School in Radiation Detection and Measurements, Munich, 2011. 45

[109] E. Farnea et al. **Conceptual design and Monte Carlo simulations of the AGATA array**. *Nuclear Instruments and Methods in Physics Research Section A*, **621**(1-3):331, 2010. 46, 52, 91

[110] S. Akkoyun et al. **AGATA–Advanced GAmma Tracking Array**. *Nuclear Instruments and Methods in Physics Research Section A*, **668**:26, 2012. 45, 46, 47, 49, 52, 91

[111] J. Gerl and W. Korten (editors). **Technical proposal for the AGATA project**. 2001. 45

[112] E. Farnea and D. Bazzacco. **The AGATA Demonstrator array at LNL**. *Nuclear Physics News International*, **22**:27, 2012. 46, 52, 53

[113] A. Wiens et al. **The AGATA triple cluster detector**. *Nuclear Instruments and Methods in Physics Research Section A*, **618**(13):223, 2010. 46

[114] **Field–Programmable Gate Array (National Instruments)**, 2012. 48

[115] A. Georgiev et al. **An analog-to-digital conversion based on a moving window deconvolution**. *IEEE Transactions on Nuclear Science*, **41**:1116, 1994. 48

[116] **Advanced Telecommunication Computing Architecture**, 2012. 48

[117] **PCI express (National Instruments)**, 2012. 48

[118] X. Grave. **NARVAL a Modular Distributed Data Acquisition System with Ada 95 and RTAI**. *14th IEEE-NPSS*, **1**, 2005. 50

[119] E. Calore and D. Mengoni. **AGATA DAQ: a NARVAL prototype installation and test**. *LNL Annual Report 2007*, page 197, 2008. 50

[120] D. Bazzacco et al. **The NARVAL emulator**. 2009–2013. private communication. 51, 63

[121] **Legnaro National Lab. website**, 2011. 52, 54, 55

[122] R.S. Kempley et al. **AGATA Demonstrator Beam Test: ^{110}Pd(^{32}S,4n)^{138}Sm Fusion–Evaporation Experiment**. *LNL Annual Report 2009*, page 17, 2010. 52

[123] F. Recchia et al. **Test–Beam Experiment with AGATA in Stand–Alone Mode**. *LNL Annual Report 2009*, page 53, 2010. 52

[124] F. Recchia et al. **AGATA Demonstrator at LNL: the Coupling with the PRISMA Magnetic Spectrometer**. *LNL Annual Report 2009*, page 55, 2010. 52

[125] K. HadynskaKlek et al. **Refinement of the Ca–42 level scheme. Preliminary results from the first AGATA Demonstrator experiment**. *Acta Physica Polonica B*, **42**:817, 2011. 53

[126] R. Nicolini et al. **Study of High–lying States in ^{208}Pb with the AGATA Demonstrator**. *Acta Physica Polonica B*, **42**:653, 2011. 53

[127] C. Louchart et al. **First Campaign with the AGATA Demonstrator at LNL: Lifetime of Excited States in ^{72}Zn and ^{74}Zn**. *LNL Annual Report 2010*, 2011. 53, 98

[128] M. Doncel et al. **Lifetime Measurement in Neutron–Rich Cu Isotopes**. *LNL Annual Report 2010*, page 5, 2011. 53

[129] J.J. Valiente-Dobon et al. **Lifetime Measurements of the Neutron–Rich Cr Isotopes**. *LNL Annual Report 2010*, page 7, 2011. 53

[130] A. Goasduff et al. **Lifetimes of Intruder States in N∼20 sd–pf Shell Neutron–Rich Nuclei**. *LNL Annual Report 2011*, page 5, 2012. 53, 62

[131] V. Vandone et al. **Study of the Order–to–Chaos Transition in ^{174}W with the AGATA-Demonstrator**. *LNL Annual Report 2010*, page 15, 2011. 53, 96

[132] P.-A. Söderström et al. **High–spin structure in ^{40}K**. *Physical Review C*, **86**:054320, Nov 2012. 53

[133] F.C.L. Crespi et al. **Response of AGATA Segmented HPGe Detectors to Gamma Rays up to 15.1 MeV**. *arXiv:1209.1188 [nucl-ex]*, 2012. 53

[134] C Louchart et al. **Investigation of the collective nature of low-lying excitations in ^{70,72,74}Zn via lifetime measurements with the plunger technique and the AGATA demonstrator**. *to be submitted to PRC*. 53, 98

[135] F Raiola et al. **Electron screening in d(d,p)t for deuterated metals and the periodic table**. *Physics Letters B*, **547**:193 – 199, 2002. 59

[136] R. Depalo et al. **ERDA and BS Analysis of the Au Targets Used for the Lifetime Measurement of the 6.79 MeV State in ^{15}O**. *LNL Annual Report 2009*, page 83, 2010. 58

[137] D. Bazzacco. **Pyton script for the configuration of Narval actors**. 2012. private communication. 63

[138] **GEANT4: A toolkit for the simulation of the passage of particles through matter**, 2012. 64, 90

[139] **Friendship and inheritance in C++ programming**, 2012. 66

[140] D. Bazzacco. **The TkT spectrum viewer**. 2012. private communication. 67

[141] D. Bazzacco. **Data processing**. 8th AGATA week, Lyon, 2010. 69, 79

[142] D. Bazzacco. `Recal` **program**. 2012. private communication. 70

[143] E.A. Lorch. **Neutron Spectra of 214Am/B, 241Am/Be, 241Am/F, 242Cm/Be, 238Pu/13C and 252Cf isotopic neutron sources**. *The International Journal of Applied Radiation and Isotopes*, **24**(10):585, 1973. 70

[144] B. Birkenbach. **AGATA Detector Library – ADL 3**. 11th AGATA week, Darmstadt, 2011. http://www.ikp.uni-koeln.de/agata/. 75

[145] O. Stezowsky. **AGATA Data Format**. 80

[146] **ROOT: A data analysis framework**, 2012. 81

[147] K. Krane. *Introductory Nuclear Physics*. "John Wiley and Sons", 1988. 89

[148] C. Domingo-Pardo, D. Bazzacco, P. Doornenbal, E. Farnea, A. Gadea, J. Gerl, and H.J. Wollersheim. **Conceptual design and performance study for the first implementation of AGATA at the in–flight RIB facility of GSI**. *Nuclear Instruments and Methods in Physics Research Section A*, **694**:297–312, 2012. 91

[149] P. Adrich et al. **A simulation tool for Recoil Distance Method lifetime measurements at NSCL**. *Nuclear Instruments and Methods in Physics Research Section A*, **598**(2):454, 2009. 92

[150] **National Superconducting Cyclotron Laboratory –Michigan State University**, 2012. 92

[151] **GEANT4: G4PhotonEvaporation Class reference**, 2012. 93

[152] E. Farnea et al. **Monte Carlo Simulations of Complex Level Schemes with Geant4**. *LNL Annual Report 2010*, page 62, 2011. 94

[153] C. Michelagnoli et al. **Lifetime Measurement of the High Spin States in ^{122}Ba**. *LNL Annual Report 2008*, page 17, 2009. 96

[154] E. Farnea et al. **Lifetime Measurements with the AGATA Demonstrator: Monte Carlo Simulations of the Array coupled to PRISMA and the Cologne Differential Plunger**. *LNL Annual Report 2009*, page 57, 2010. 98

[155] G. Gilmore and J. Hemingway. *Practical Gamma–Ray Spectroscopy*. John Wiley & sons, 1995. 103

[156] R.C. Ritter et al. **Investigation of states in ^{15}O by the ^{14}N(d,n)^{15}O reaction**. *Nuclear Physics A*, **140**(3):609 – 624, 1970. 108

[157] I.J. Thompson. *Computational Physics Report*, **7**, 1988. 108

[158] George H. Rawitscher. **Effect of deuteron breakup on elastic deuteron–nucleus scattering**. *Physical Review C*, **9**:2210–2229, Jun 1974. 108

[159] N. Keeley. **Analysis of Transfer Reactions: Determination of Spectroscopic Factors**. *Ecole Joliot-Curie, Maubuisson, France*, 2007. 108

[160] Walter Hauser and Herman Feshbach. **The Inelastic Scattering of Neutrons**. *Physical Review*, **87**:366–373, Jul 1952. 110

[161] P. A. Moldauer. **Why the Hauser–Feshbach formula works**. *Physical Review C*, **11**:426–436, Feb 1975. 110

[162] E. Sheldon and R.M. Strang. *Computer Physics Communications*, **1**. Elsevier Science, 1969. 110

[163] **MINUIT: Function Minimization and Error Analysis –Reference Manual**, 2013. 111

[164] K. Nakamura et al. **Particle Data Group**. *J. Phys. G*, **37**:075021, 2010. 114

[165] R. Andrae. **Error estimation in astronomy: A guide**. *arXiv: 1009.2755v3 [astro-ph]*, 2010. 114

[166] Dino Bazzacco. **Estimation of the statistical uncertainties via re–sampling technique**. 2013. private communication. 116

Acknowledgements

I am extremely grateful to Santo Lunardi and Calin Ur for the supervision of this work and for allowing me to follow the activities of the research groups of Padova and Legnaro and let me managing independently my research activities, being, however, always available for useful suggestions and discussions. In addition to my supervisors, this thesis work would not exist without the help/contribution of other people I want to acknowledge: Dino Bazzacco: without his constant and tireless help and "teaching" all the part related to the AGATA data analysis and chi–square analysis would not exist. I am really grateful to him for the time spent in explaining me everything I needed/wanted to understand. I hope I will be capable of "mantaining" the "lernt lessons" also in the future, in whatever job I will do. Enrico Farnea: without his help I would have never even started dealing with Geant4 and the AGATA simulation code. His help was fundamental also for the draft of this Thesis. Carlo Broggini: his revision and explanetion of the astrophysical case was really important. I want to thank him for his helpfulness. A particular acknowledgement to: all the participants to the experiment, in particular the experiment spokesperson, Roberto Menegazzo (together with Calin Ur) and R. Depalo, for her important contribution to the data replay and analysis; C. Rossi-Alvaretz, A. Caciolli, D. Bemmerer, M. Marta, for the useful discussions and the target preparation; N. Keeley, for CRC-CDCC calculations, fundamental for the analysis; A. Dewald, for the fruitful discussions about plunger measurements and the idea of the simulation code for Doppler shift lifetime measurements; C. Sthal and M. Reese, for the useful DSAM discussions; P.G. Bizzeti, for the helpfulness and useful advices; T. Marchi, for the unveiling of the root secrets; D. Mengoni for the useful discussions about data replay; J.J. Valiente–Dobon, S. Lenzi, G. De Angelis, A. Gadea, for allowing me to participate to interesting experiments that, even if not directly related to the subject of the thesis, were really a big opportunity to learn and make new discoveries.

E GRAZIE di cuore a: Tommaso, Daniela e Benedetta, la mia seconda famiglia; Margi e Lorenzo; Dario e Lucia; Don Andrea; Paola, Elisa e tutta la famiglia Fabbri; Giorgia, Riccardo e Chiara; Daniele, Barbara e Sofia; Marco; Andrea G.; Javier; Andres; Silvia e Daniel; Daniele Montanari; Gabriele; Angela; Monica; Pasqualina; Grazia; Maura e famiglia; Ivana e Loredano; Davide, Roberta e Leonardo; Alessandra e Linda; Maria; Tea; Alain; Luisa

Last but not least: la mia cara e meravigliosa famiglia –Sere, Babbo, i mie pupilli Matti e July, Cristiano, Alessandro. Grazie Enrico. Grazie cara mamma.